# Modelling and Assessment of Battery Electric Vehicle Powertrain and the Impact on Dynamic Characteristics in relation to Addis Ababa, Ethiopian Driving Profile

Tatek Mamo Wachamo

A Dissertation Submitted to the Department of Mechanical Engineering, School of Mechanical Chemical and Materials Engineering

Presented in Fulfilment of the Requirement for the Degree of Doctor of Philosophy in Automotive Engineering

Office of Graduate Studies
Adama Science and Technology University

August 2024
Adama, Ethiopia

# Modelling and Assessment of Battery Electric Vehicle Powertrain and the Impact on Dynamic Characteristics in relation to Addis Ababa, Ethiopian Driving Profile

Tatek Mamo Wachamo

Main Supervisor: Dr. Rajendiran Gopal (Professor)

Co-supervisor: Dr. Bisrat Yoseph (Associate Professor)

A Dissertation Submitted to the Department of Mechanical Engineering, School of Mechanical Chemical and Materials Engineering

Presented in Fulfilment of the Requirement for the Degree of Doctor of Philosophy in Automotive Engineering

Office of Graduate Studies
Adama Science and Technology University

August 2024
Adama, Ethiopia

# DECLARATION AND RECOMMENDATION

## Declaration

I hereby declare that this dissertation entitled, **“Modelling and Assessment of Battery Electric Vehicle Powertrain and the Impact on Dynamic Characteristics in relation to Addis Ababa, Ethiopian Driving Profile**” is my original work. That is, it has not been submitted for the award of any academic degree, diploma or certificate in any other university. All sources of materials used for this dissertation have been duly acknowledged through appropriate citations.

| Name of student | Signature | Date |
|---|---|---|

## Recommendation

Under our guidance, Tatek Mamo Wachamo prepared the dissertation **"Modelling and Assessment of Battery Electric Vehicle Powertrain and the Impact on Dynamic Characteristics in relation to Addis Ababa, Ethiopian driving profile**" which was submitted in fulfilment of the requirements for the degree of Doctor of Philosophy in Automotive Engineering. We, the dissertation supervisors, hereby certify that we have read and revised the dissertation. As a result, we advise submitting the dissertation to the department for additional evaluation and defence.

| | | |
|---|---|---|
| Rajendiran Gopal (Professor) | ____________ | ____________ |
| Main Supervisor | Signature | Date |
| Bisrat Yoseph (Associate Professor) | ____________ | ____________ |
| Co-supervisor | Signature | Date |

# APPROVAL PAGE

We hereby certify that the recommendations and suggestions made by the board of examiners are appropriately incorporated into the final version of the dissertation entitled "Modelling and Assessment of Battery Electric Vehicle Powertrain and the Impact on Dynamic Characteristics in relation to Addis Ababa, Ethiopian Driving Profile" by Tatek Mamo Wachamo.

| | | |
|---|---|---|
| Rajendiran Gopal (Professor) | | |
| Main Supervisor | Signature | Date |
| Bisrat Yoseph (Associate Prof) | | |
| Co-supervisor | Signature | Date |

We, the undersigned, members of the Board of Examiners of the dissertation open defence by Tatek Mamo Wachamo have read and evaluated the dissertation entitled "Modelling and Assessment of Battery Electric Vehicle Powertrain and the Impact on Dynamic Characteristics in relation to Addis Ababa, Ethiopian driving profile" and examined the candidate during open defence. This is, therefore, to certify that the dissertation is accepted for fulfilment of the requirement of the degree of Doctor of Philosophy in Automotive Engineering.

| | | |
|---|---|---|
| Chairperson | Signature | Date |
| Ramesh Babu (Associate Prof) | | |
| Internal Examiner | Signature | Date |
| Venkata Ramayya (Professor) | | |
| External Examiner 1 | Signature | Date |
| Daniel Tilahun (Associate Professor) | | |
| External Examiner 2 | Signature | Date |

Finally, approval and acceptance of the dissertation is contingent upon submission of its final copy to the Office of Postgraduate Studies (OPGS) through the candidate's Department Graduate Council (DGC) and School Graduate Committee (SGC)

| | | |
|---|---|---|
| Department Head | Signature | Date |
| School Dean | Signature | Date |
| Office of Postgraduate Studies, Dean | Signature | Date |

# ACKNOWLEDGMENT

First of all, I want to sincerely thank Prof. G. Rajendiran Gopal and Dr. Bisrat Yoseph, my supervisors, for their constant guidance and constructive criticism. Their unwavering encouragement, motivation, counsel, and perceptive remarks are greatly valued. I would like to thank Prof. Girma Woldesnbet for his intelligent criticism, which pushes me to think beyond the box and raises the standard of my work. His rapid response, unwavering diligence, and counsel have truly touched me.

I express my gratitude to every member of the doctorate committee for their insightful feedback on the progress reports. I am indebted to the Editors and Reviewers for their insightful comments on the manuscripts that I sent in to be published in journals. I also want to express my gratitude to my fellow postgraduate students for their support and encouragement.

I owe a debt of gratitude to Adama Science and Technology University and Ethiopian Defence University for their scholarship and financial assistance with this dissertation. My sincere appreciation is extended to Mr. Adana Abdeta, the deputy manager of Addis Ababa city's Sheger Express bus organisation, for his help in configuring the GPS-equipped vehicles that are utilised to collect fleet data.

I am incredibly grateful to my spouse Helen Asamenew for her wonderful and unwavering moral support, which lifted my spirits even on the gloomiest of days. I would especially like to thank my children, Leul and Yididya Tatek, for being my constant sources of inspiration. I also want to express my gratitude to my family and everyone else whose constant moral and financial support has allowed me to continue with my postgraduate studies.

Last but not least, I want to express my gratitude to God Almighty! Give yourself full credit.

# TABLE OF CONTENTS

# LIST OF TABLES

# LIST OF FIGURES

# LIST OF ACRONYMS AND ABBREVIATIONS

| | |
|---|---|
| AA | Addis Ababa |
| AASU | Addis Ababa and its sub-urban |
| Afp | Projected frontal area |
| Ah | Ampere hour |
| a | Track of the vehicle |
| $a_{i,x}$ | Instantaneous translational inertia of the vehicle |
| BEV | Battery electric vehicle |
| BIW | Body in white |
| CAD | Computer aided design |
| $C_D$ | Aerodynamic drag coefficient |
| CDF | Cumulative diagram functions |
| Cf | Damping coefficient of the front dampers |
| CFD | Computational fluid dynamics |
| CG | Center of gravity |
| $C_L$ | Aerodynamic coefficient of lift |
| CMBP | Clustered modular battery pack |
| $C_P$ | Aerodynamic coefficient of pitch |
| Cr | Damping coefficient of the rear dampers |
| CRGE | Climate resilient green economy |
| $C_{RM}$ | Aerodynamic rolling moment coefficient |
| CS | Component-sizing |
| $C_{YM}$ | Aerodynamic yawing moment coefficient |
| DOD | Depth of discharge |
| DOF | Degree of freedom |
| ECM | Equivalent circuit models |
| ECMS | Equivalent consumption minimization strategy |
| EMDE | Emerging market and developing economies |
| EMS | Energy management strategy |
| EPA | Environmental protection agency |
| ESS | Energy storage system |
| $F_D$ | Aerodynamic drag force |

| | |
|---|---|
| FEM | Finite element method |
| $F_L$ | Aerodynamic lift force |
| $F_S$ | Aerodynamic side force |
| GHG | Greenhouse gas |
| h | Height of center of gravity of the vehicle |
| HEV | Hybrid electric vehicle |
| H-P | Hip Point |
| i | Time instant |
| ICEV | Internal combustion engine vehicle |
| IEA | International Energy Agency |
| $i_{tf}$ | Combined transmission and final drive ratio |
| Ixx | The moment of inertia of car body about x-axis |
| Iyy | The moment of inertia of car body about y-axis |
| k | Turbulent energy |
| Kf | Stiffness of front suspension spring |
| Kr | Stiffness of rear suspension spring |
| Kt | Stiffness of tire |
| KWh | Kilo Watt Hour |
| L | Wheelbase |
| $l_1$ | Location of front axle from center of gravity |
| $l_2$ | Location of rear axle from center of gravity |
| LMIC | Low- and middle-income countries |
| MG | Motor-generator |
| MT | Micro trip |
| $M_{VG}$ | Gross mass of the vehicle |
| NEDC | New European driving cycle |
| NKE | Negative kinetic energy |
| NYCC | New York City cycle |
| NZE | Net zero emission |
| ODE | Ordinary differential equation |
| OEM | Original equipment manufacturers |
| PCA | Principal component analysis |
| PHEV | Plug-in hybrid electric vehicle |
| PID | Proportional-integrative and derivative |

| | |
|---|---|
| $P_M$ | Aerodynamic pitching moment |
| PMS | Power management strategy |
| PMSM | Permanente magnet synchronous motor |
| RNA | Relative negative acceleration |
| RPA | Relative positive acceleration |
| RPM | Revolution per minute |
| RSBS | Rebuild with behavior split |
| SE | System Engineering |
| SgRP | Seating reference point |
| SOC | State of charge |
| ST | Short trips |
| UDDS | Urban dynamometer driving schedule |
| USABC | United States advanced battery consortium |
| $V_\infty$ | Free stream air velocity |
| WLTC | Worldwide harmonized light vehicles test cycle |
| $X_S$ | Total sprung mass displacement |
| $\ddot{X}_B$ | Acceleration of car body |
| $\omega_M$ | Angular speed of electric motor |
| $\varepsilon$ | Dissipation rate |
| $\theta$ | *R*oad slope angle |
| $\theta_r$ | Roll angle of car body |
| $\ddot{\phi}_p$ | Pitch effect angular acceleration of car body |
| $\ddot{\theta}_r$ | Roll effect angular acceleration of car body |
| $\phi_p$ | Pitch angle of car body |
| $\phi_{pf}$ | Propulsion system function |

# ABSTRACT

*In recent years, battery electric vehicles (BEVs) have gained attention due to their zero emissions and improved efficiency. However, their global market spread is hindered by the range anxiety of customers associated with a limited driving range and the requirement of long time to charge the battery. To alleviate the challenges, grid power forecasting, energy consumption estimation, range prediction and lifecycle analysis need to be addressed considering the use phase conditions. The BEV manufacturers are focusing on the market of developed countries and their operating cycle evaluation is also based on those countries. However, to increase market share, their development should explore new operating conditions and duty cycles, particularly for developing countries. This dissertation develops a Systems Engineering methodology for the integration of an electric powertrain within vehicle sizing and synthesis, specifically tailored to the driving profile of Addis Ababa, Ethiopia. It assesses energy consumption, powertrain efficiency, and dynamic performance characteristics in a virtual environment using valid models and a simulation setup. A new BEV driving cycle was developed for Addis Ababa, Ethiopia, using GPS-collected data and compared with the k-means clustering method and legislative drive cycles. This cycle was then integrated with powertrain sizing. Top-level energy-based modelling and subsystem parametric models were employed to validate the method and simulate country-specific energy consumption, powertrain efficiency, and driving range. According to the simulated results, acceleration requirements demand the maximum force and power, with low and high speeds needed for desired performance. The proposed BEV drive cycle shows a 14.57% and 8.9% reduction in energy consumption compared to the Urban Dynamometer Driving Schedule (UDDS) and Worldwide Harmonized Light Vehicles Test Cycle (WLTC)-2. The Addis Ababa and its suburbs (AASU) cycle demonstrated an average cycle efficiency of 88.7%, reaching 96% efficiency of the implemented electric motor. Additionally, the AASU cycle provided 5-20 km more range than the WLTC cycle, reducing the battery size by 3.4 kWh for urban car driving. Subsequently, a Finite Element Method (FEM) model of the body structure integrated with the powertrain package was analyzed for both aluminum and structural steel. The aluminum body structure exhibited a weight reduction of 11.75%, resulting in energy savings and extending the range by 18.21 km. The study, conducted in a Computer-Aided Design (CAD) model, also revealed that powertrain components packaging and side wind velocity impact aerodynamic drag and stability. The increase in drag force was attributed to drag-induced underbody, rear side, and the opposite side of the wind attack. The car's power requirement increased significantly with side wind, potentially causing instability in high winds exceeding 15 m/s. However, at no wind effect, the drag force of the variant with a clustered battery pack decreased by 7.15%. The implemented methodology for sizing and packaging the BEV powertrain resulted total reduction of battery size by 7.23 kWh. The study further evaluated the ride dynamic performance of a converted car using MATLAB/SIMULINK software. While no significant changes in comfort were observed, there was an increase in vertical displacement peak and pitch motions due to center of gravity (CG) position changes. Acceleration over a bump profile ranged from 0.6 to 0.9 m/s2, with discomfort less than 0.315 m/s2. However, no major consequences were observed for a short duration. Finally, the methodology demonstrated its capability in sizing BEV powertrains based on typical driving cycles, vehicle dynamics characteristics, and customer needs.*

***KEYWORDS:*** Addis Ababa, Battery electric vehicle, aerodynamics, Driving cycle, Energy consumption, Modelling, Power-train sizing, Driving range and Vehicle stability

# CHAPTER ONE

# INTRODUCTION

## 1.1 Background of the Study

### 1.1.1 The Environment and Energy Concern of the Transport Sector

Road mobility is crucial for economic and social development, as it facilitates access to services, jobs, and opportunities. Rapid urbanization has increased the demand for transportation, but internal combustion engine vehicles contribute to local pollution and greenhouse gas emissions (GHG) (Chesterman & Chevallier, 2022; Hossain, Kumar, Islam, Selvaraj, & Miralinaghi, 2022). Fossil fuel combustion produces greenhouse gas emissions, primarily carbon dioxide, contributing to global warming. The transport sector has consistently increased emissions, with road transport accounting for 70% of these emissions in 2019, generating nearly 8.5 Gt $CO_2$ and three times higher than 1990 as shown in Figure 1.1(Outlook, 2022).

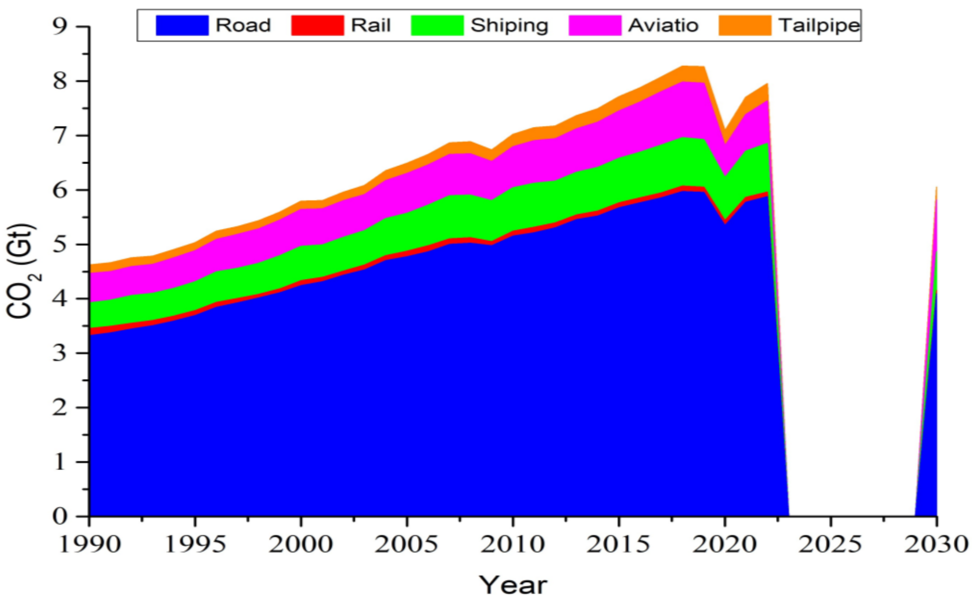


Figure 1.1: Global $CO_2$ emission by transport system since 1990 to 2022 (Outlook, 2023)

The burning of fossil fuels releases pollutants into the local air, such as carbon monoxide (CO), ozone, sulphur oxides ($SO_X$), nitrogen oxides (NOx), and volatile organic compounds (VOC). These pollutants are linked to heart disease, lung cancer, pregnancy problems, and unfavourable birth outcomes (Outlook, 2023). This is particularly true in low-income nations with older car stocks and loose emission regulations (Jihui, Agyemang, Zhaolin, & Gao, 2022). Fossil fuels dominate the transportation industry, accounting for 30.8% of their use. The global fleet of vehicles is forecasted to reach 2 billion by 2050 (Jihui et al., 2022). With vehicle ownership near saturation in high-income countries and rapid motorization in low- and middle-income countries, energy demand is increasing, but many countries rely on imported oil, making balances vulnerable to price shocks (Chesterman & Chevallier, 2022; Hossain et al., 2022; Sayed, Kassem, Saleeb, Alghamdi, & Abo-Khalil, 2020).

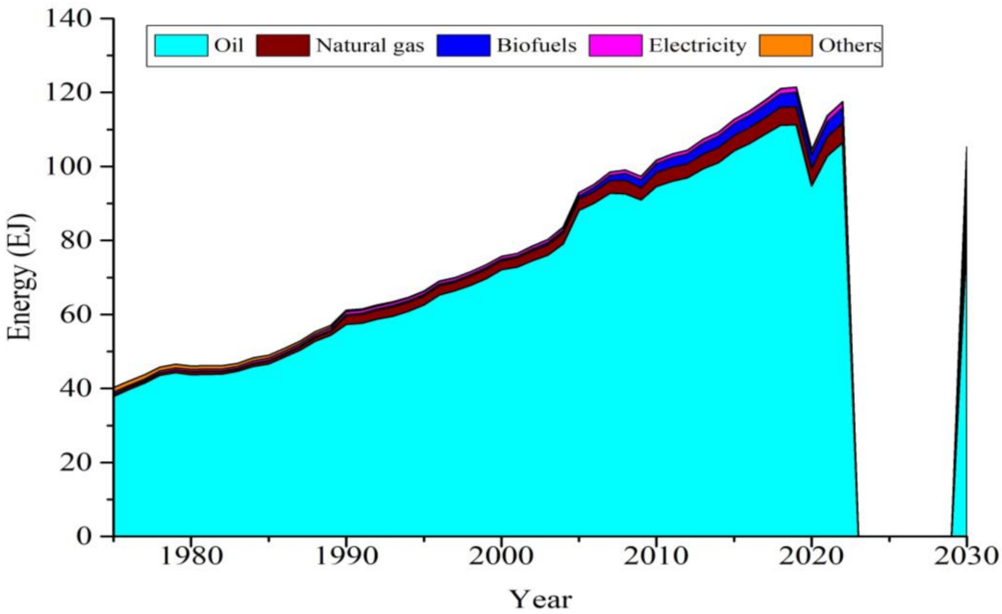


Figure 1.2: The global energy consumption by transport sector since 1970 to 2022

In 2022, the transport sector accounted for 62% of global oil consumption, with 80% allocated to road vehicles. Countries are encouraged to develop a low-emissions strategy under the Paris Agreement, focusing on environmental protection and investing in $CO_2$-neutral technologies (Hoang, Pham, & Vu, 2022; Sanjarbek, Mavlonov, & Mukhitdinov, 2022). Governments promote public transportation and BEV sustainability priorities (Outlook, 2023). The issue of climate change and energy sustainability necessitates a comprehensive approach, involving technological advancements, policy modifications, and alterations in consumer behaviour, crucial for the planet's health and future generations.

### 1.1.2 Global trends in Transportation Electrification

BEV fleets are expanding at a fast pace with 14% of all new cars delivered worldwide by 2022. As in prior years, the number of electric vehicles on the road climbed by 60% to 26 million due to higher sales, with BEVs contributing more than 70% of this rise annually. Across areas and powertrains, the growth in sales of electric cars varied, but China continues to lead the way. In 2022, China sold 4.4 million BEVs, a 60% increase over the previous year. In 2022, there were 2.7 million electric cars sold in Europe, a 15% increase from 2021. Europe remained the second-largest market for electric vehicles after China, accounting for 25% of all electric vehicle sales worldwide in 2022. Sales of electric vehicles rose by 55% in the US in 2022 over 2021. This increase accounting for the world's largest vehicle markets of China 60 %, Europe, and the United States in common 39 %. The three largest markets for electric vehicles worldwide in 2022 were China, Europe, and the United States, together accounting for approximately 95% of sales.

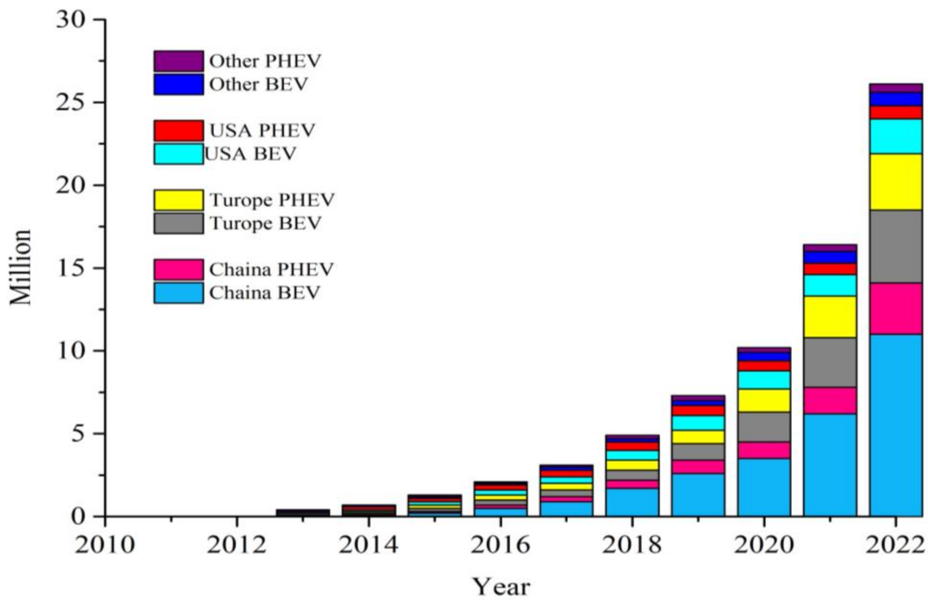


Figure 1.3 Uptake of global BEV stock in developed economy market since 2010

The market share of electric cars in developing countries and emerging markets (EMDEs) other than China is quite small. With less than 0.5 percent of total sales, electric mobility is now very minor in low- and middle-income countries (LMICs). Although the motorization levels on the African continent remain the lowest, most African countries are experiencing one of the fastest rates of vehicle growth over 10% when compared to just 4% in European nations. Moreover, just one out of every ten cars brought into the region is brand-new; the majority of automobiles are second-hand. These offers African nations a unique opportunity to reduce the fleet's emissions before motorization takes off much more (Outlook, 2022).

In 2021, governments increased their focus on electrifying road transport and aiming for net zero emissions. They also emphasized the need for strategic electric vehicle (EV) charging infrastructure and resilient supply chains. China reduced subsidies for new energy vehicles, while the US set targets for 50% EV sales by 2030 and 500,000 public chargers. The European Union's Fit for-55 package also aimed for 100% ZEVs by 2035. In 2021, Japan, Korea, and India introduced significant funding packages for EVs and charging subsidies (Outlook, 2023). They extended eligible funding until 2025 for slow chargers and EVs. India increased subsidies for electric two-wheelers and committed to battery-swapping policies and EV manufacturing. Most Asian and Latin American countries aim for 100% ZEV sales by 2030-2050. Africa has a small share of EVs, but countries are creating conditions to support electric mobility. The number of BEV models is expected to increase rapidly, particularly in emerging markets and developing economies (Chesterman & Chevallier, 2022).

However, the transition to electrification of transportation is a complex process involving a shift from fuel-intensive to material-intensive energy systems, raising policy questions and affecting sustainability, growth, and inclusion. E-mobility involves multiple value chains, charging networks, and multi-sectoral cooperation. It may add complexities to local systems and potentially be contested, impacting the environment, economy, and society. Transitioning to e-mobility is driven by sustainability and economic impact on supply chains and markets. The switch to electric mobility represents a substantial technological advance, and these changes are frequently accompanied by a change in the infrastructure from fueling to charging. Large electricity infrastructure expenditures are needed to support this transition.

Challenges vary across countries due to policies, consumer preferences, and infrastructure availability. Due to differences in baseline vehicle fleet age, performance, and composition, LMICs have particular transport policy contexts. (König et al. 2021). However, most studies in relation to electric mobility challenges have never been considered from the LMIC perspective. Therefore, pprioritizing sustainable economic development through efficient energy resource utilization at the national level is crucial to overcome these barriers (Hoang et al., 2022; G. Zhao, Wang, & Negnevitsky, 2022).

### 1.1.3 Prospective of E-mobility in Ethiopia

The second-most populated nation in Africa, Ethiopia, has challenges including poor water supplies, a lack of access to quality healthcare, a growing population, a lacklustre economic growth, poor institutional frameworks, and a lack of awareness. As the capital of Ethiopia and the headquarters of the African Union (AU), AA is home to a plethora of distinct economic, political, cultural, and diplomatic environments, in addition to population dynamics, shifting geography, and congested transit. AA is a densely crowded metropolis with over 5.23 million citizens, and it is increasing at a 4.4% yearly rate. The total number of vehicles in the nation exceeds 1,325,000, of which around 630,000 are registered cars classified as AA. The number of vehicles per km on a single-lane asphalt road is 168 (Gebisa, Gebresenbet, Gopal, & Nallamothu, 2022). The huge volume of fossil fuel usage requires significant foreign currency spending and has an impact on the balance of payments, as well as socioeconomic and environmental challenges that affect social infrastructures such as health care and education.

The administration is concentrating on important policy tools to deal with these problems. The nation's government has identified alternative energy sources to replace the use of fossil fuels, making the energy sector one of the core pillars of its Climate Resilient Green Economy (CRGE) policy. In 2022, a "targeted subsidy" system was implemented to reduce fuel subsidies, leading to a trade deficit and reduced investment in health and education (Gebisa et al., 2022). Ethiopia is implementing a CRGE strategy to reduce GHG emissions by 36 $MtCO_2e$ from 2010 to 2030. The government promotes alternative energy sources, hybrid and EVs fleets, and renewable rail networks. Ethiopia's government has reduced EVs tax rates to 15%, promoting environmental safety, public health, climate, biodiversity, and renewable energy use, while reducing fuel imports.

BEVs are considered an NDC-aligned scenario, with goals of meeting emissions targets by 2030 and 2035, as well as reaching net zero emissions (NZE) by 2050. Ethiopia is promoting electric mobility through a campaign and media, with ambitions to add 4,800 electric buses and 148,000 autos over the next ten years.

Ethiopia has the second-highest hydropower potential in Africa (45,000 MW) (Khan, 2017; Belay Kassa, 2019; Lin, 2004; Kabalan, 2020). Renewable energy sources such as hydropower, wind, and geothermal have a 1,402GW electricity exploitable potential. The region's low temperatures, low travel speeds, and everyday travel distances of less than 80 kilometres make EV solutions suitable. Driving BEV in Ethiopia is reported to be 88 folds cheaper, when 1kilo watt electricity compared with equivalent 1 litre of gas that can reduce the country's fuel expenditure by one-third. Typical 26kWh and 4-seater automobiles that are imported by Green-tech require only 9.10 Eth birr (about USD 0.17) to qualify full charge daily driving range of 200 km (Khan, 2017; Belay Kassa, 2019).

### 1.1.4 Overview of BEVs and Their Challenges

Globally, there is a growing interest in environmentally friendly technologies, with electric propulsion being a primary alternative to traditional vehicles and the electrification of road vehicles is an emerging trend. BEVs offer higher powertrain efficiencies, less maintenance, and zero tailpipe emissions, offering clean and efficient road transportation that is very different from the classical ICEV as shown in (Table 1.1). BEVs are valuable and commercially viable in complex intelligent transport systems due to their supervisory management and dynamic control capabilities (Sayed et al., 2020; Shin, Kim, Yoo, Kim, & Han, 2023). Electric vehicles have modular designs, making them compact and ideal for new technologies like ADASs and AD. They have high torque at low speeds, better dynamic performance, and wider speed range compared to traditional gasoline and diesel engines. Their noise, vibration, and harshness performance is also impressive.

These vehicles combine key automotive technologies, including mechanical, electric traction machines, power controllers, and energy storage devices. Powered by electricity and motors supported by rechargeable batteries, they can enhance energy security and macroeconomic resilience in countries generating electricity from renewable and alternative energy sources. EVs use an electric propulsion system, consisting of a motor drive, transmission device, and wheels, to overcome road load and resistance, generating power and delivering it to the wheels. BEV powertrains store energy in a battery and receive power from a Motor Generator (MG).

Table 1.1: Comparison of gasoline, diesel, hybrid EV (HEV) and BEV

| Drive cycle | Model | Fuel | Mass (Kg) | Power (kW) | Unadjusted. Fuel economy (mpg) |
|---|---|---|---|---|---|
| FTP | ML 250 | Diesel | 2495 | 150 | 29.5 |
| | ML 350 | Gasoline | 2381 | 225 | 21.9 |
| | RX450h | GHEV | 2268 | 183 | 41.2 |
| | Model X90D | BEV | 2495 | 310 | 124.2 |

The MG converts electrical power into mechanical power, which is transferred to wheels through a simplified transmission. Regenerative braking involves the MG converting mechanical power into electrical power to recharge the battery, ensuring that the braking energy is not completely lost. Variations in electric propulsion characteristics, energy sources, and control requirements lead to different EV configurations. The typical layout of a BEVs is simplified in Figure 1.4.

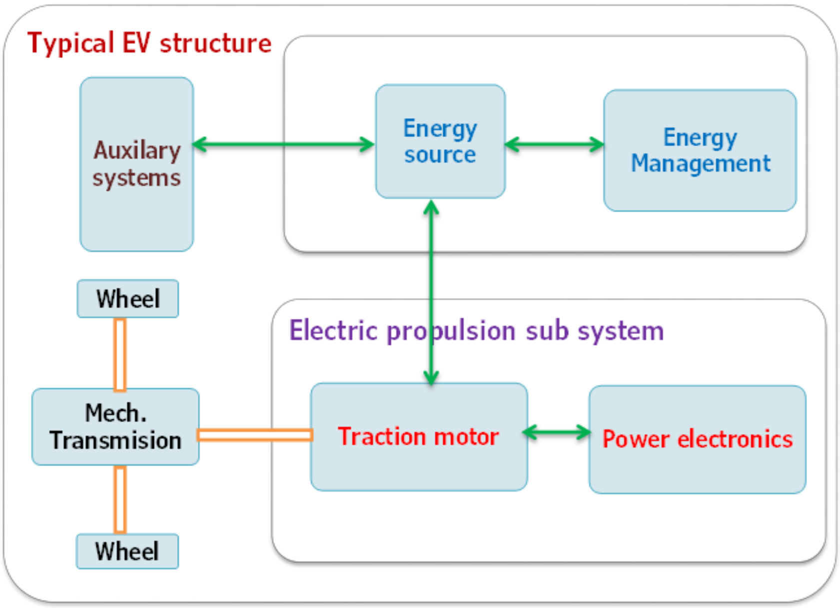


Figure 1.4: Simple schematic representation of a BEV

For automakers, the popularity of BEVs offers both possibilities and challenges. Novel design approaches are required for new models because of technological developments like regenerative braking systems and lightweight materials. During the BEV development phase, automakers are implementing conversion and purpose design ideas. Low investment costs are necessary for conversion design since it incorporates high-voltage components into the already-existing onboard system. Design flexibility is however constrained by the current package and layout of the conventional ICE vehicle. Several nations have made it possible for conventional automobiles to be converted to electric systems since 2020, providing possible remedies. According to Pierri et al. (2021) and Nicoletti et al. (2020), new design concepts that incorporate new vehicle models and component arrangements are required to improve competitiveness (Outlook, 2023Sankaran, 2022 #34). Thus, development of sustainable road transportation system, utilizing passenger vehicles with electrified driveline systems, face challenges in development due to a lack of standardized procedures, improper simulation methods, and unknown technical details. The uncertainty level affects vehicle architecture decisions, powertrain sizing and the implemented control strategy.

### 1.1.5 Importance of Modelling and Simulation in the Process of BEV Design

The design process for BEVs involves multidisciplinary engineering and art, requiring optimal integration of components, driving characteristics, energy consumption, vehicle safety, ergonomics, and design {Hossain, 2022 #100, Heimes, 2020 #93}. Prediction models, engineering design methodologies and simulation tools can be used to support the development of electric vehicles, taking into account relevant influencing factors (e.g., safety, vehicle dynamics) and components (battery, power electronics, motor, gear). Modelling and simulation is crucial in understanding its performance, efficiency, and behaviour under various driving conditions. Simulations with appropriate models helps estimate energy consumption and range of the BEV under various driving cycles and to optimize the design of the electric motor, gearbox, and battery pack to ensure optimal performance, efficiency, and durability.

In recent years, several studies have been reported for the formulation of BEV models including mathematical model {Kabalan, 2020 #137; Martyushev, 2023 #148}, steady-state model (Elkamel et al., 2019), multi-body dynamics model (Liu et al., 2018, Xia et al., 2020) and Detailed dynamic and transient models (Decker et al., 2021, Cinar, 2018) to address the characteristics of BEVs and their sub-components. It was found that most previous methods in characterizing BEV are based on pre-assumed parameters and does not integrate the models with vehicle synthesis at the conceptual design stage. In functional models formulation assumptions, approximations, simplification, linearization, and discretization of the model are unavoidable. Besides, time-based models have been used most frequently to represent the characteristics of a vehicle's operating profile and position-dependent models have not been assessed well. Hence applicable model of a physical system and assignment of adequate control strategy is crucial for optimal powertrain sizing and evaluating dynamic performance of BEV. Utilizing simulation tools and prediction models to analyze dynamic behavior may yield suggestions for promising vehicle segments and the demand for charging infrastructure prediction for typical cities or regions.

### 1.1.6 Significance of Addis Ababa and its Sub-Urban Driving Profile

In previous studies, readily available standard, legislative and representative driving cycles (DC) were used to evaluate and certify the design requirements of BEV (Zhao et al., 2021, Peng et al., 2020). However, there are significant differences in torque, power and braking characteristics of BEV and ICEV in a wide speed operating range (Yu et al., 2020, Sayed et al., 2020). In recognition of the significant differences in standard and real-data DCs to determine country-specific energy consumption and to certify the design requirements, most realistic driving cycles that are unique for each city or region have been developed (Wang et al., 2022, Peng et al., 2020, Khemri et al., 2019, Arun et al., 2017, Han et al., 2021). The previous studies conducted on the evaluation of BEV powertrains were based on data from the road conditions in developed countries (Chandrashekar et al., 2021). Few studies were conducted based on developing county's road conditions such as on Addis Ababa, Ethiopian (Gebisa et al., 2022), (Huzayyin et al., 2021). Furthermore, the influence of sub-urban on the inner city driving pattern and trip duration was not addressed. In most capital cities of low-income countries and like Addis Ababa, the driving pattern is influenced by roads mixed by pedestrians and different vehicles, single-lane vehicle composition, poor road quality, the absence of traffic signals and the interlinked traffic flow in suburbs and urban route setting {Outlook, 2022 #378;Chandrashekar, 2021 #74}.

As Ethiopia’s capital and the seat of the African Union (AU), Addis Ababa is characterised by a comprehensive economic, political, cultural and diplomatic environment, with varying topography, population dynamics and highly congested traffic conditions. Addis Ababa is characterized a highly populated city, with more than 5.23 million residents, and is growing at a rate of 4.4 % annually. The city has 630,000 registered vehicles and the count along a single-lane asphalt road is 168 vehicles per kilometre (Gebisa et al., 2022, Busho and Alemayehu, 2020). Addis Ababa is surrounded by small towns with 60 km of suburban routes from the city centre along cross-country main roads. Public transportation using city buses and passenger cars is the preferred means of transport by those in the low and middle-income class living in AA and looking for low-cost accommodation in the neighbouring towns {Belay Kassa, 2019 #9}.

Addis Ababa, the capital city of Ethiopia, is experiencing rapid urbanization and economic growth, leading to an increase in traffic congestion and air pollution. The Ethiopian government has set ambitious targets to reduce greenhouse gas emissions and improve air quality regarding road transport focused on green transport strategy via BEV deployment.

Ethiopia is developing a local electric platform for entry- and middle-level markets by incorporating BEV sustainability practices into its industrial ecosystem. However, the driving conditions in Addis Ababa are unique, with frequent stop-and-go traffic and steep hills, which can affect the performance and dynamics of BEVs. Therefore, it is essential to investigate the impact of these driving conditions on the powertrain size and dynamics characteristics of BEVs. The insight for improved energy consumption and efficiency, by improving vehicle design and production capabilities enhance local electric vehicle platform for entry- and middle-level market. Ethiopia's young population could benefit from electric mobility, reducing petroleum dependency and boosting energy security.

## 1.2 Statements of the Problem

In the current decade, one of the most important topics in automotive sector has been battery electric vehicles. Electric propulsion has been recognised as a main alternative that can be easily integrated into existing transportation networks to entirely replace traditional cars in the near future. The research on Battery Electric Vehicles (BEVs) has significantly advanced, focusing on battery technology, energy consumption, environmental impact, infrastructure development, economic feasibility, market adoption, and vehicle performance. Studies suggested to improve battery chemistry, enhancing energy density, charging speed, and lifespan, while optimizing energy consumption through advanced management systems and efficient powertrain designs. Infrastructure studies emphasize the importance of a robust charging network and grid integration. Economic analyses reveal that declining battery costs and operational savings make BEVs increasingly cost-effective. Policy and market adoption research highlights the influence of incentives and consumer attitudes on BEV penetration. Additionally, performance assessments demonstrate BEVs' superior dynamics, such as instant torque and better handling, underscoring their potential to revolutionize the automotive industry despite ongoing challenges in technology, infrastructure, and market acceptance.

Standard and legislative driving cycles (DC) have been created and employed to assess the performance of both Internal Combustion Engine Vehicles (ICEV) and Battery Electric Vehicles (BEV). However, most extensively studied realistic driving cycles pertain to developed countries and are not suitable for replication in low and middle-income countries due to differences in road infrastructure, vehicle types and compositions, and fleet characteristics. As Ethiopia seeks to transition to a more sustainable transportation sector, there is a growing need for adoption of BEVs in Addis Ababa. Despite the growing global interest in BEVs, there is a lack of comprehensive studies on how BEVs perform under the unique driving conditions of Addis Ababa. Existing research has primarily focused on traffic patterns, road conditions, and driving behaviours in developed urban areas, with little attention given to developing cities like Addis Ababa. This gap includes understanding the common traffic patterns, road conditions, and driving behaviours in Addis Ababa and comparing these factors to other urban areas. Key performance metrics for BEVs, such as energy consumption, range, and acceleration, have not been fully explored within this specific context.

The Addis Ababa driving profile, characterized by frequent stops, congested roads, and varying topography, poses unique challenges for BEV powertrains. Additionally, the impact of local traffic conditions and road infrastructure on BEV acceleration, braking, and handling remains under-researched. There is also a need to examine how different types of roads, including urban streets and highways, affect BEV performance. Furthermore, modifications or adaptations to BEV powertrains to better suit the local driving profile have not been adequately addressed. Optimization of energy consumption and battery life for the conditions of Addis Ababa is another critical area requiring investigation. Potential reductions in emissions and fuel consumption compared to conventional vehicles need to be quantified, alongside an assessment of current policies and incentives for electric vehicle adoption in Ethiopia. Addressing these gaps is essential for promoting the effective integration of BEVs in Addis Ababa and similar urban environments

This study examines the performance and dynamics of battery electric vehicle (BEV) powertrains in relation to the specific driving profile of Addis Ababa, Ethiopia. By analysing local traffic patterns, road conditions, and driving behaviours, the research aims to assess how these factors impact BEV performance metrics such as energy consumption, range, and acceleration. The study investigates the dynamic characteristics of BEVs, including their handling, braking, and acceleration, under typical Addis Ababa driving conditions. This study aims to develop a comprehensive model of BEV powertrain performance and dynamics characteristics under these conditions, with the goal of informing the design and optimization of BEVs for the Ethiopian market.

This study develops a simulation-based model that accurately captures the interactions between BEV powertrains and the Addis Ababa driving profile, enabling the development of optimized BEV designs that meet the needs of Ethiopian drivers. It explores potential optimizations for BEV powertrains to enhance efficiency and performance in this context.

Furthermore, there is limited data on the actual performance of BEVs in Addis Ababa, making it challenging to assess their feasibility for widespread adoption in Ethiopia. Hence, the study address this problem by collecting data on real-world driving patterns in Addis Ababa and using it to validate a simulation-based model of BEV powertrain performance under these conditions. Additionally, the research evaluates impacts of BEV adoption and considers the role of local policies and infrastructure to provide valuable insights for policymakers, manufacturers, and users seeking to better understand the potential benefits and limitations of BEVs in Ethiopian cities.

## 1.3 Objectives of the Study

### 1.3.1 General Objective

The goal of this dissertation is to assess the powertrain size of the BEV and its impact on dynamic performance characteristics of the evolutionary new vehicle by modeling and simulation in virtual set up that is initialized by typical driving cycle representing Addis Ababa and its suburbs, Ethiopia

### 1.3.2 Specific Objectives

The specific objectives of this study are to:-

- Synthesize representative BEV drive cycle for Addis Ababa and its suburbs driving profile with driving behavior
- Model and assess the characteristics of BEV powertrain size based on realistic Addis Ababa and its suburbs drive cycle
- Analyze static structural and dynamic characteristics of FEM BEV body structure integrating battery pack and main powertrain components
- Evaluate aerodynamic performance of the new converted BEV in relation to minimized energy consumption and improved stability
- Assess ride comfort and stability characteristics of the new converted BEV using full car dynamic model

## 1.4 Scope of the Study

The primary focus of this dissertation is on mathematical modelling and simulation of BEVs, which may be utilized in the predesign stage to examine and identify the best combination of multiple factors influencing powertrain design. To represent actual control variables and points, high-level supervisory management of the powertrain was linked with sizing optimization based on a realistic driving profile. This driving profile was created using field data from the Addis Ababa route. A methodology for optimal powertrain sizing and dynamic analysis is offered in order to improve the vehicle's performance and stability. In this study, a combination strategy including propulsion electrification and vehicle size at the early idea stage was used, with a body in white (BIW) conversion platform, to examine the dynamic performance of BEVs.

The study initially examines the normal driving cycle and driving behavior for Addis Ababa and its suburbs using GPS-collected real-world data. By using the synthesized drive cycle, it investigates a method for CS and the best control strategy for this integration notion via system modelling and simulation. The study utilizes 3D Euler/Navier Stokes equations and computational aerodynamic techniques to investigate car body aerodynamics, addressing the lack of research on powertrain evolution's impact on low-speed cars' aerodynamic performance and stability. Finally, the full car suspension Simulink model and applied mathematical analysis are replicable, allowing for a thorough evaluation of various design choices based on the interactions and trade-offs between various subsystems, assessing the effectiveness of the mathematical approach and validating the outcomes and control algorithms. Experiments were done to develop cost-effective and reliable instrumentation for gathering driving profile data from GPS-enabled vehicles. Detailed design of powertrain components, thermal effects of battery pack and component based controller design are out of the scope of this study.

## 1.5 Significance of the Study

The study focuses on BEVs and their powertrain dynamics, which is a critical aspect of electric vehicles' overall performance and efficiency. Addis Ababa, Ethiopia's capital, is chosen as the study location due to its unique driving conditions, which are characterized by varying road types, traffic congestion, and climate. The study contributes to the understanding of BEV performance and its suitability for adoption in Addis Ababa, a city with growing traffic congestion and environmental concerns. This information will help policymakers and stakeholders make informed decisions about promoting electric vehicle adoption.

The research adds to the existing body of knowledge on electric vehicle dynamics and powertrain modeling, providing a new case study on a developing country context. The research develops and validates a dynamic model of BEV powertrains, which can be used to predict and optimize vehicle performance in various driving conditions. This model can be applied to other cities with similar driving profiles, enhancing the overall efficiency and effectiveness of electric vehicles.

This research develops the first new AASU BEV DC for Addis Ababa's interconnected urban and suburban routes, using a novel micro-trip random selection-to-rebuild with behavior split approach and determining the maximum simulation period based on real-world data.

The study introduces demand power intensity analysis for vehicle operation, combining subsystem parametric models with vehicle-level energy flow and power demand analysis to visualise overall performances with respect to energy consumption, range, and efficiency in simulation framework. It also introduces a novel clustered design for packaging batteries, enabling air cooling and improved vehicle stability even in higher wind conditions. Another innovative component of this research is the investigation of an aerodynamically efficient architecture for the battery pack and its integration with the body and frame of the baseline vehicle, which has not before been investigated in the literature. It also evaluates the possibilities of a baseline suspension system for integrated packaging in offering maximum comfort within an acceptable vibration threshold of natural frequency.

The study provides valuable insights into the specific driving profiles and conditions in Addis Ababa, which can inform the development of BEVs tailored to meet local needs. This includes optimizing vehicle design, energy consumption, and range for the Ethiopian market. The study's findings can inform the design of BEVs tailored to Addis Ababa's driving conditions, ensuring optimal performance and efficiency. The research can help planners and policymakers develop charging infrastructure that meets the needs of BEV users in Addis Ababa. Understanding the impact of driving conditions on BEV performance can inform pricing strategies for electric vehicles in Ethiopia. Overall, this dissertation study has significant implications for promoting sustainable transportation options in Addis Ababa and beyond, while contributing to the broader field of electric vehicle research.

## 1.6 Organization of the Dissertation

This research's first chapter presents the topics and justification for the investigation. In order to address a particular audience and establish a wide framework for the topic, background and rationale are examined. Within an acceptable scope, research questions are addressed while defining the problem and stating its aims. Lastly, the research's significance and the target audience have been mentioned. The remaining portions of the dissertation are arranged as follows. A thorough assessment of prior research on BEV powertrain sizing, energy management techniques, and the vehicle's interconnected dynamic performance is provided in ‘Chapter 2’. The methodological framework developed is described in detail in ‘Chapter 3’, and it serves as the foundation for this research's model-based powertrain sizing, battery pack packaging, aerodynamics improvement, and trade-off assessment of suspension and body structure of the integrated systems of BEVs with a focus on vehicle dynamics analysis and system development. In ‘Chapter 4’ results and discussion are presented. ‘Chapter 5’ summarizes results and conclusions and makes recommendations for additional research.

# CHAPTER TWO
# LITERATURE REVIEW

## 2.1 BEV Development Methodologies

### 2.1.1 Overview of Engineering System Development

Design methodology is an organised process that integrates design science, cognitive psychology, and real-world experience to create technical systems. It encourages rationalisation, innovation, and impartial assessment. Good design techniques are supported by systems theory, which connects socio-economic-technical processes, procedures, and methodologies. Methods of Engineering design involve acquiring system needs, defining goals, and evaluating solution concepts. Systems theory has been applied in various contexts Pahl et al. (2007). According to the Defence Acquisition University (DAU) (2001), system Engineering (SE) is a process that transforms customer needs into system functional and performance descriptions, generating information for decision making and providing output for the next design and development phase.

Numerous authors have contributed to product design, focusing on mechanical design processes applied to complex systems. Pahl et al. (2007) discuss engineering design theory in relation to product life cycles, while Ulrich & Eppinger (2012) describe concept development as an iterative front-end process. Ullman (2010) presents a sequential design process.

Price et al. (2006) discuss challenges in integrating integrated approaches to Systems Engineering life-cycle design, including lack of basic models, cost considerations, multidisciplinary optimization, data flow, and low fidelity models, emphasizing cost integration. They proposed a new methodology for cost-effective, predictable system development, utilizing value-based statistical methods for commercial vehicle design, focusing on High Speed Civil Transport studies and evaluating value throughout the design lifecycle.

Kossiakoff and Sweet (2003) suggest that technological advancements and complex systems' obsolescence offer opportunities for system upgrades, design changes, or retrofits. They suggest a separate life cycle for systems development with phases like concept development, exploration, concept definition, and engineering development. Integration faces challenges due to repairs and configuration uncertainty.

Pugh's method and Design Structure Matrix (DSM) methods are proven approaches for comparing alternative concepts. Pugh's method involves a step-by-step approach, scoring each concept based on criteria. DSM is useful in engineering management and system modifications, predicting propagation of the change within complex systems.

Predicting design change relationships is necessary for managing complex system modifications. Trade-off studies lead to synthesis, which develops feasible system concepts. Systems analysis was utilized to develop concepts and define detail, using simulation, analysis models, and tools to evaluate results against criteria like TPMs and metrics.

### 2.1.2 The BEV System Design

Multidisciplinary engineering and art are used in the design of BEVs, which necessitates the best possible integration of parts, driving characteristics, energy consumption, vehicle safety, ergonomics, and design (Heimes, Kampker, Haunreiter, Davids, & Klohs, 2020; Hossain et al., 2022). SE as the core design strategy for electric driveline development, a widely used design approach for systems that are complex with different levels of verification cycles and correlations among interdisciplinary knowledge. The "V chart" is the foundation of SE design, describing the design and validation process. However, it is not clearly defined how to analyse such coupled methods of power management strategy (PMS) and CS where all options and value ranges are included, and the solution space might be very large, as shown on Figure 2.1.

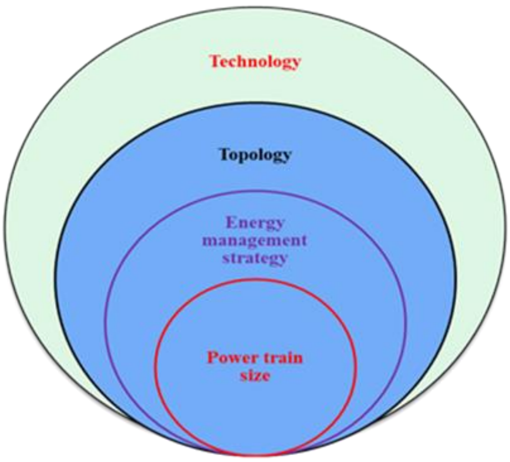


Figure 2.1: Possible design space in development process of BEV

Therefore, it is compulsory to device a method that involves gathering and manipulating components, decomposing elements, and verifying them to encounter customer and public expectations. This section presented the knowledge required to realize the technology behind and challenges of designing for fully BEVs; review of works done by different scholars related to BEV design approach, existing CS and vehicle dynamics analysis. The approaches were classified into various sub-types in a systematic manner, with essential features and limitations highlighted for each, and the gap in currently reported methodology was recognised and explained to provide a valuable reference for active researchers.

## 2.2 BEVs Layout

BEVs are intelligent machines that are primarily made up of important automotive, electrical, electronic, information, and chemical technologies. As a result, the subsystems that make up their system architecture are mechanical, electrical, electronic, and informational. There are different type possible EV configurations as a consequence of the variations in electric propulsion characteristics, energy sources and control requirement. The retrofitting process involves evaluating vehicle system architecture to avoid cost escalation and motion dynamics risks. The propulsion system, electric motor, controllers, external dimensions, power needs, and suspension system of the vehicle should be evaluated.

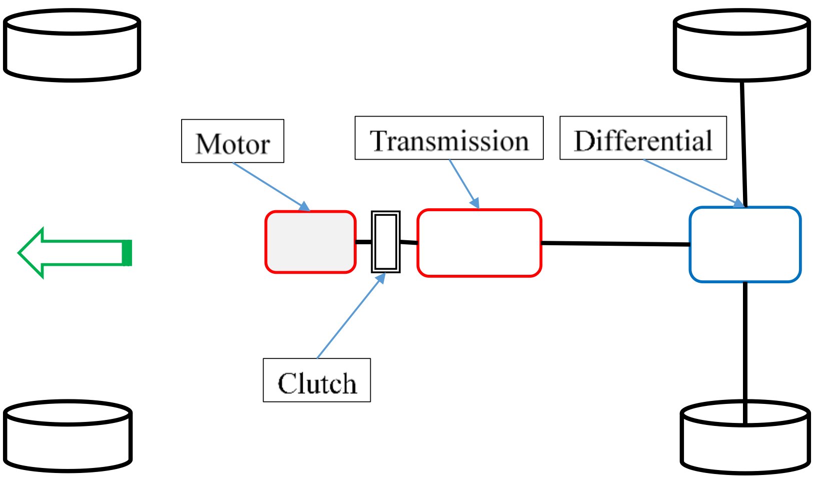


Figure 2.2: Single axle drive arrangements or basic BEV driveline architecture

The evolution of BEV powertrain architecture is basically from ICE vehicle drive line replaced by electric propulsion including electric traction machine, a clutch, a gearbox, and a differential. According to (Hassan, Mohd, Aris, Azura, & Ibrahim, 2015) Low level control

(LLC) is the arrangements of EV power hardware mainly energy storage system (ESS), electrical motor (EM), power converters and mechanical and electrical link. Different LLC architectures have reported based up on intended use addressing the design criteria of powertrain. Single assembly transaxle arrangement with simplified electronic control to produce high-torque low-speed and constant-power high-speed zones (Huang et al., 2018, Guo, Zhang, Dong, & Guo, 2019). Two traction motors by torque splitting control without mechanical differential (C.-C. Lin, Peng, & Grizzle, 2004) and further in-wheel drive train attained (Cinar, 2018; Lajunen, 2018).

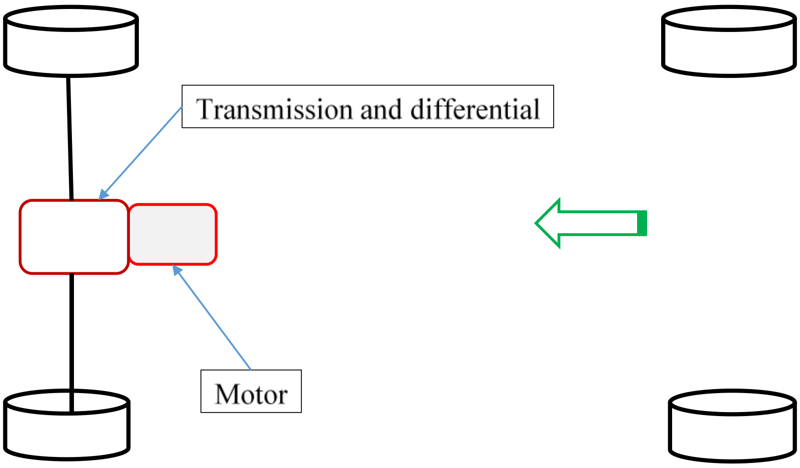


Figure 2.3: Single assembly transaxle layout

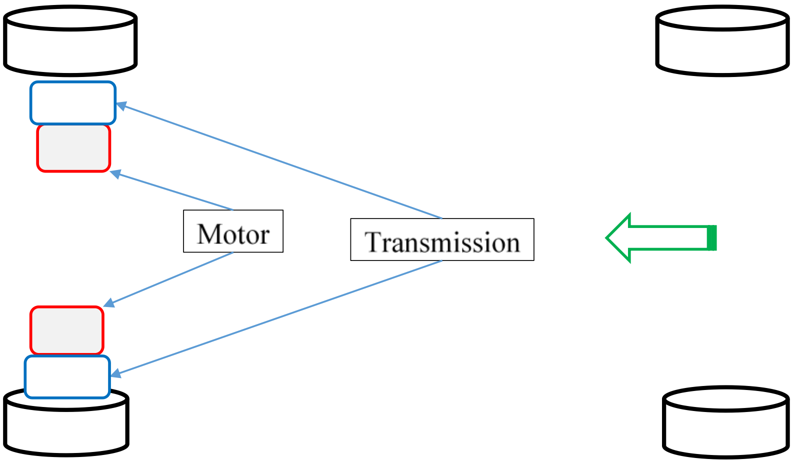


Figure 2.4: Wheel motor with torque splitting control or In-Wheel motor arrangement;

Moreover, the design of EV propulsion can be Single Motor (SM) shown in Figure 2.3 or Multiple Motors (MM) in Figure 2.4, (Grunditz, 2016) categorized as concentrated Single Axle (SA) or distributed through several. (Wager, 2017) categorized one-motor and two-motor based powertrains. (Pathak, 2019) introduced the term booster for assistant motor, where powered only when the vehicle power requirement is very high such as aggressive acceleration, climbing slopes, slope starting and tack over is required. Additionally, boosters enhance regenerative brake energy if drive wheels have both hydraulic and regenerative brake while boosted wheels are only regenerative brake.

Table 2.1: Summary of Low Level Component Architectures

| Topology | Key features | Limitations | Ref |
|---|---|---|---|
| SA SM drive | Smaller foot print, lower cost and simpler control algorithms | Less tractive effort than MM | (Pathak, 2019) |
| SA MM drive | Smaller foot print, a lower cost and requires torque vectoring | Complex control algorithms than SM | (Brahim, Abdelfatah, & Automation, 2012; Deur, Škugor, & Cipek, 2015) |
| FWD | Improved tractive effort based on geometry and axle load | High load on front Less braking | (Brahim et al., 2012) |
| RWD | Lower load on front steering wheels | Lower tractive effort than FFWD | (Ehsani, 2018) |
| 4WD | Increased tractive effort, fail safe functions, efficiency | Increased mass and complex control | (Silvaş, Hofman, & Steinbuch, 2012) |
| 4WD with boosters | Good tractive effort efficiency, regenerative braking | Increased mass and complex control | (Pathak, 2019) |

In summary, multiple motor Four Wheel Drive (4WD) configurations were found to have better vehicle characteristics of maximum speed, acceleration, and top speed. Because of the principle of longitudinal vehicle dynamics, having several propelling axles has the potential to improve tractive effort and dependability. Furthermore, this configuration is capable of providing fail-safe functionalities, allowing the vehicle to continue driving after a component fails. However, increasing the power mix to both axles improve efficiency until an optimum is reached, at which point efficiency falls (Pétursson, 2017). The disadvantages of this setup include the necessity of a sophisticated algorithm for power splitting and the increased weight and expense of additional components. On contrary, a propulsion system concentrated in a SA has a smaller footprint, lower cost, and requires simpler control algorithms, making it an excellent contender for low-cost vehicles.

## 2.3 MODELLING BEV

### 2.3.1 Battery Model

Batteries are the common energy storage devices used in BEVs. They are combined electrochemical cells that store chemical energy and release it back as the electrical energy when demanded. Lithium-Ion Batteries (Li-ion) that are broadly used in consumer electronics such as mobile phones, laptops, etc., because they are characterized by high energy to unit mass ratio compared to other types are identified as best fit for BEV. Besides, they are identified by their high specific power, high-energy efficiency, and better high temperature performance and low self-discharge. However, much research work is being conducted to make them more cost-effective, extend their usable life, and improve safety against overheating (Bisschop, Willstrand, & Rosengren, 2020; Martellucci & Krishna, 2021).

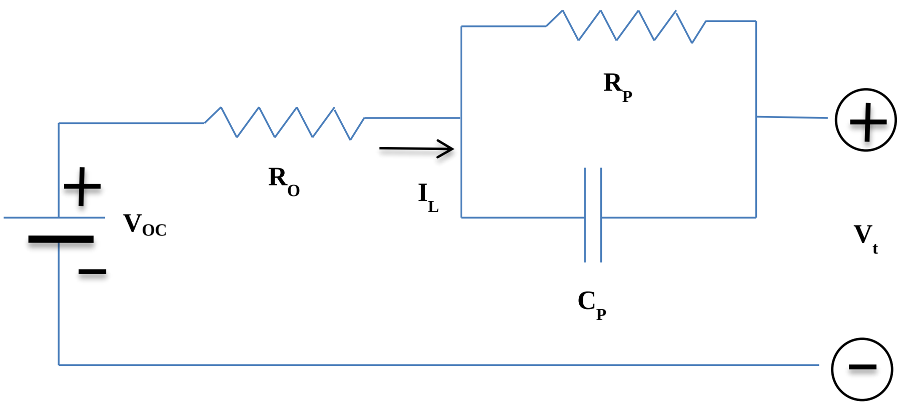


Figure 2.5: Equivalent circuit battery model

In the simulation study and analysis or control design for BEVs, an accurate battery model verifying its behaviour is required. Equivalent circuit models (ECM) are commonly used for SOC and SOH estimation.

Table 2.2: Comparison of the seven models for modern battery {Lekshmi, 2019 #203}

| Battery model | Remarks | Features |
|---|---|---|
| Shepherd model | Simplest electro-chemical model | Battery behaviour modelled in relation to voltage and flow of current |
| Unnewehr model | Simplified shepherd model | Variation in resistance modelled in terms SOC |
| Nernst model | Modified Shepherd model | SOC modelled as exponential function |
| Combined model | Most accurate electro-chemical model | Combination of three electrochemical models |
| Rint model | Equivalent circuit model | Simplest considering only internal resistance |
| Thevinin model | Based on Rint model | RC circuit added in series to consider polarization |
| Dual polarization model | Modified Thevenin and most accurate model | Two RC circuits to consider concentration and electro-chemical polarization separately |

This model is identified by easy online application and low computational burden. A simple ECM (Fotouhi et al., 2016a) (Propp et al., 2016) can consist of a resistor in series with one or many RC-elements, terminal voltage (Vt), load current (IL), internal resistance (R0) and polarization resistance (Rp) and capacitance (Cp) respectively shown on Figure 3.1(Zou et al., 2015). They are particularly of high interest to estimate battery state accurately (Reick, Kaufmann, Stetter, & Engelmann, 2021; Saldaña, San Martín, Zamora, Asensio, & Oñederra, 2019). Table 2.2: shows summary of model equations along with comparison of seven modern battery models are presented.

### 2.3.2 Electric Traction Machine and Transmission Models

Most reviewed electric machines are DC, AC, SAC, IM and AAC machines. DC machines (Hedon, 2018) benefit from an easy control, but their use in BEVs is limited due to performances, wear susceptibility and higher cost. Permanent magnet SAC machines (Un-Noor et al., 2017) present the best performances in relation to efficiency, torque and mass power, maintenance and controllability. However, because of the field weakening technique, those machines have extremely low efficiency at high speeds. The field-weakening zone can be better controlled in wound rotor machines, by acting directly on the current. However, the global efficiency is still lower than for permanent magnet machines (Ehsani, 2018).
In AAC machine, a difference exists between the synchronous speed and the operating speed. This machine is well known technology by little maintenance, performance, and a large scale of speed with a better efficiency even at maximum power and maximum speed (Jazar, 2017). However, its efficiency is below that of permanent magnets machines and heavier than synchronous machines in general.
An electric machine being complex to model, best compromise for trade-off between time of computation and accuracy can be done by using efficiency map based models (Hayes et al., 2019). However, the dynamic effects are not represented in this model. According to (Chavan and Talange, 2017), the Simulink model that expresses the vehicle's rotational speed and input torque best captures the dynamic effect. It has been shown that a powertrain with MM can distribute torque requests unevenly. The relation for motor drive model can described as;

$$T_e = J\frac{d}{dt}\omega_r + F\omega_r + T_m \tag{2.1}$$

Where, $T_e$ is electromagnetic torque, the maximum motor (TM) is mechanical torque and $\omega_r$ is motor speed.

With the available drive line gear ratios, the maximum tractive force of the vehicle can be achieved by creating traction with the highest power plant torque. Thus, having a solid considerate of the vehicle's engine plant and gearbox characteristics can help the implementation of traction controllers. The gearbox matches the speed-torque characteristics of the source with the load demand by supplying gear ratios {Dagci, 2018 #153}. For comparing lower and higher gear ratios, planetary gear gearbox with a constant differential gear ratio is preferred. These can be modelled analytically by Equations (2.2) and (2.3):

$$i_{gr,1} = \frac{N_R + N_S}{N_S} = \frac{W_{VG}\left(f_r cos\theta_{max} + sin\theta_{max}\right)}{T_{max} i_{gr,f} \eta_{tf}} \tag{2.2}$$

$$i_{gr,2} = \frac{N_R + N_S}{N_R} = \frac{\sum_i \omega_{em,i} R(1-i)}{V_{max} i_{gr,f}} \tag{2.3}$$

Where, $T_{max}$ is maximum torque of electric motor, $i_{gr,1}$ and $i_{gr,2}$ are the lower and higher gear ratios, $\eta_{tf}$ is combined efficiency of transmission and final drive, $\omega_{em,i}$ angular speeds of each electric motor, $N_S$ and $N_R$ are number of teeth of ring and sun gears respectively.

### 2.3.3 Regenerative brake model

The BEVs' use of regenerative braking greatly improves the required energy usage. In order to charge the battery, the technology transforms the kinetic energy emitted while braking into electrical energy. The system consists of a precisely controlled power converter coupled with an electric motor/generator {Jin, 2015 #315}. The vehicle deceleration can be used for braking force calculation as:

$$F_b = M_{GV} a_X = M_{GV}(-\frac{dV}{dt}) \tag{2.4}$$

Where, $M_{GV}$ is the vehicle's gross mass, $F_b$ braking force, $a_x$ is deceleration of vehicle and V is velocity of vehicle

When running on graded roads, the deceleration measured by the onboard sensor is the resultant of the deceleration on plain roads and acceleration due to gravity, g $\sin\alpha$, where $\alpha$

is the road angle. As the required force for braking are proportion to the coefficient of friction, its distribution is in accordance with the corresponding ratios on $R_f$ and $R_r$ {Itani, 2016 #316}. According to {Khodaparastan, 2018 #267} regenerative braking power can be described as,

$$P_{brake} = \frac{J_T[(\omega_2(\omega_2 - \omega_1))]}{(t_2 - t_1)} \tag{2.5}$$

Where, JT is total inertial reflected at traction motor shaft, $\omega_1$ is initial angular velocity and $\omega_2$ is final angular velocity.

### 2.3.4 Characterizing BEV dynamics

#### 2.3.4.1 Longitudinal dynamics

Until now, a great deal of research has been documented regarding the development of BEV models for verifying the top-level performance requirements and to characterize the vehicle with its sub-systems (Sayed et al., 2020, Hossain et al., 2022, Sanjarbek et al., 2022). Different authors developed the vehicle's basic dynamic model from fundamental physics of Newton's 2nd law applicable for motion. (Tudoroiu et al., 2018, Mastanamma et al., 2017, Patwardhan et al., 2019, Chavan and Talange, 2017). Most authors used simple estimation of tractive power to determine power required by EV against predefined conditions {Tudoroiu, 2018 #271;Ripaccioli, 2009 #231;Mastanamma, 2017 #240;Patwardhan, 2019 #297;Chavan, 2017 #296}.

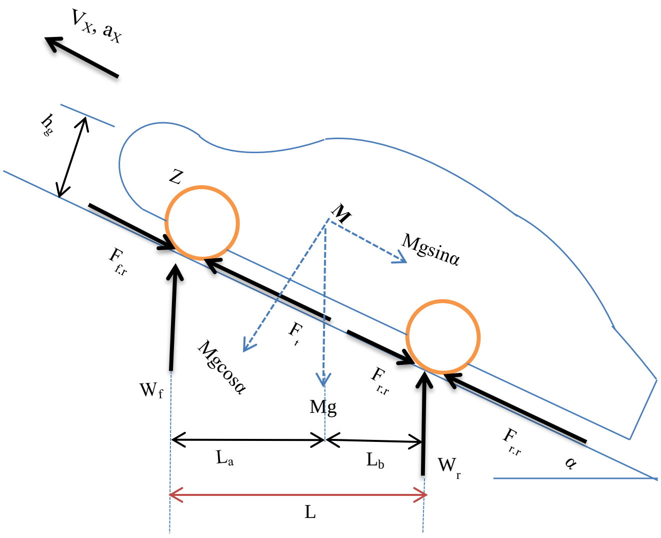


Figure 2.6: Typical road loads of longitudinal dynamic vehicle considering road slope

The total power required to overcome rolling resistance, aerodynamic drag, the weight component that must be compensated for while climbing slopes, and vehicle acceleration is used to compute this tractive power. In a specific DC, the tractive effort required to propel the vehicle is expressed as {Smith, 2020 #293};

$$F_T = F_{rr} + F_{gr} + F_{dr} + F_{ar} \tag{2.6}$$

Where, $F_T$ is total tractive effort whereas $F_{rr}$, $F_g$, $F_{dr}$ and $F_{ar}$ are rolling, grade, aerodynamic drag and acceleration resistances of the given vehicle respectively.

Numerous complex and simplified models having different degrees of freedom are also described mathematically to represent vehicle dynamics. A mathematical model (Martyushev, Malozyomov, Sorokova, Efremenkov, & Qi, 2023; Sharmila et al., 2022) steady-state model (Elkamel et al., 2019), multi-body dynamics model (Xia et al., 2020,Liu et al., 2018, Xia et al., 2020) and Detailed dynamic and transient models (Decker et al., 2021, Cinar, 2018) used to assess the characteristics of BEVs and their sub-components. The authors found that multibody dynamics model suitable for multi-degree vehicle dynamics, detailed for component-level effects, and a longitudinal model for energy and efficiency analysis, with the ability to represent the road slope. However, previous methodologies for characterizing BEVs often use pre-assumed parameters and do not integrate with vehicle synthesis during the phase of conceptual design. Time-based models are mainly used, but position-dependent models not yet evaluated properly.

#### 2.3.4.2 Vertical dynamics

BEV powertrain components, heavier than ICEV components, may expose them to vibrations in the critical frequency span due to mass and geometric location variations, affecting axle weight distribution.(Arora, Kapoor, & Shen, 2018; Pierri, Cirillo, Vietor, & Sorrentino, 2021). Such Vibrations can cause deflection, stress, malfunctions, decreased component lifetime, discomfort, and vehicle rollovers when component frequency matches applied load, amplifying oscillation. Besides, road irregularities impact vehicle’s ride and stability. Therefore, the imparted influence on suspension system performance as a consequence of BEV powertrain integration should be assessed considering road irregularities and the response of natural frequency (Gohrle et al. 2014; Kim and Choi, 2016, lexandru, 2020 #462}.

Research for ride comfort analysis has focused on optimizing parameters including excitation spectrum, rider's vibrating frequency response, and exposure duration in various automotive models. Numerous researchers have examined quarter-car model’s vertical behaviour using numerical analysis to determine changes in parameters like mass and ratios of dampers’ damping and springs’ stiffness as shown on Figure 2.7. Although, this model is the popular method for analysing suspension it fails to account for pitching, yawing, and rolling motions those are affecting vehicle ride quality and stability over uneven terrain (Funde, Wani, Dhote, & Patil, 2019).

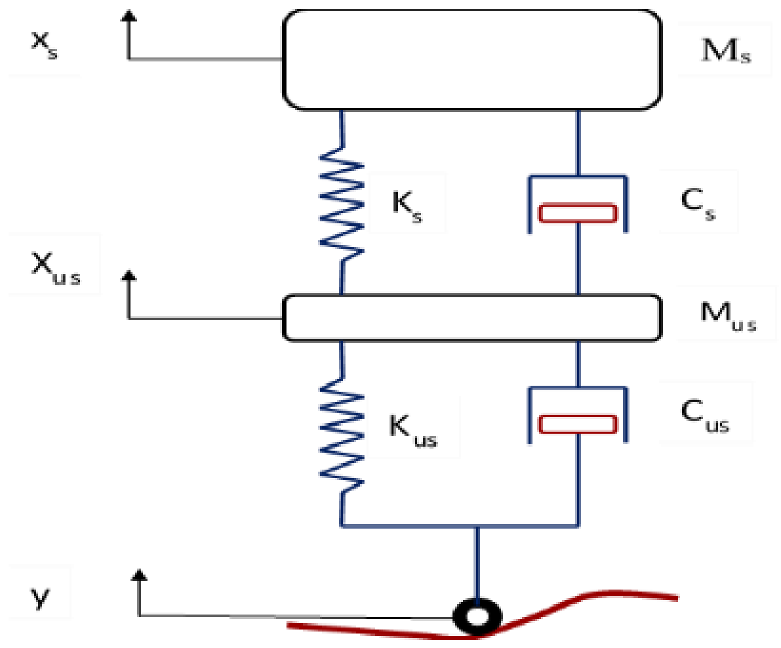


Figure 2.7: A quarter car model considering vertical behavior for the vehicle body

Studies aim to improve parameters related to ride and handling using half car model illustrated on Figure 2.8: considering bounce and pitch on rough roads, and propose suspension control systems (Al-Ghanim & Nassar, 2018; Alexandru, 2020; Khan, Abid, Ahmed, Wadood, & Park, 2020). Researchers have created full dynamics vibration models for vehicle dynamics analysis and integrated control, accurately representing the suspension and predicting dynamic performance and comfort (Deepankumar et al., 2021; Lefèvre, Kracht, & Schramm, 2020; van Kempen, 2019). Commercial software packages like ANSYS-Motion and Recur Dyna analyse vehicle dynamics, but impose computational burden and require experience. Therefore, a faster but affordable method that is capable for driving tests through simulation is desired (C. Liu, Fang, Liu, & Hu, 2018; Sharmila et al., 2022).

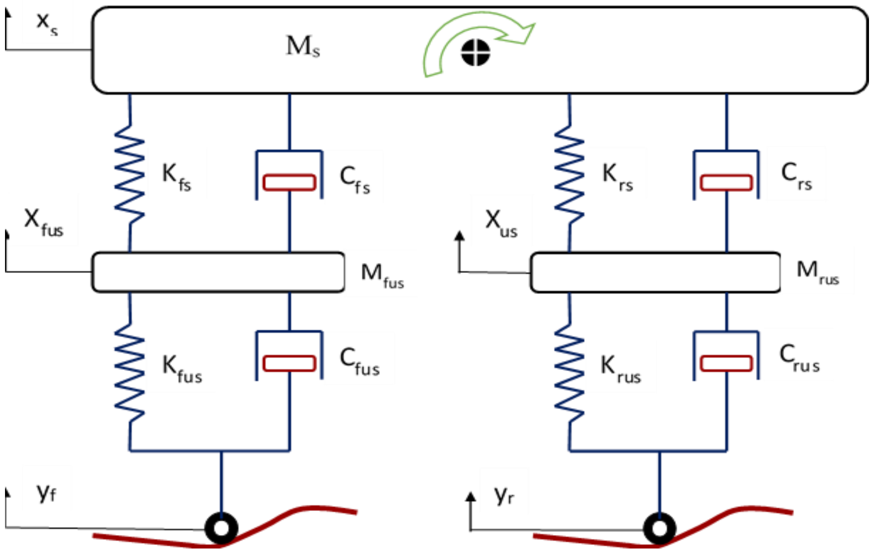


Figure 2.8: A model considering pitch bounce behavior for the vehicle body

#### 2.3.4.3 Aerodynamics of the BEV

To bridge the gap caused by limited battery technology, BEVs must improve how well they use the energy stored in their batteries and the efficiency of their motor. Furthermore, aerodynamics analysis is highly important as aerodynamic resistance significantly impacts energy demand and BEV stability, especially when running at high speeds, increasing the tendency of roll instability (Cavusoglu, 2017; Huluka & Kim, 2019; Muhammad Nabil Farhan et al., 2021). Reports indicated that the shape and powertrain arrangement affect aerodynamic characteristics of traditional fuel vehicles. However, BEVs have a unique structural layout for large battery pack replacing the fuel tank. This complicates layout planning and can disrupt airflow. More research should be conducted to better realize the influence of battery pack construction.

Experimental test by using wind tunnel tests, theoretical analysis, and computer calculations have been utilized to investigate BEV aerodynamics. Real-world tests yield accurate results but are expensive. Theoretical analysis models simple problems but cannot satisfy complex phenomena. Computational fluid dynamics (CFD) is used for accurate turbulence models (Cavusoglu, 2017; Muhammad Nabil Farhan et al., 2021), (Alexandru, 2020; Khan et al., 2020)

The study by Arora and Cavusoglu analyzed the battery pack’s effect on the aerodynamic characteristics of BEV in steady-state motion. It reveals that battery pack structural parameters impact drag and lift coefficients, with longer packs resulting in lower drag and higher lift, enhancing EV performance, fuel economy, and handling stability. Accurate results require quality mesh generation and proprietary code computation (Alexandru, 2020; Stanciu et al., 2021), Phoenics CHAM 2017).

#### 2.3.4.4 Tire model

Linear tyre models are frequently used for vehicle dynamic simulations, assuming constant tyre stiffness coefficients in both longitudinal and transverse directions. Since linear models are easily implementable, they have been accustomed for designing linear controllers for active systems. However, they do not fully represent nonlinear tyre behaviour. Many nonlinear tyre models, such as the Pacejka, Delft, Sakai, Buckardt, Brush, Dugoff, and Pacejka "magic formula" models, have been studied for simulation. These models, characterized by 10-20 coefficients for force generation, are mostly used in professional simulations for dynamics of a vehicle and racing car games because of their accuracy, ease of programming, and quick solution. The popular magic formula can be expressed by equations (2.7) and (2.8).

$$Y = D\sin\left(C\arctan\left(B\phi\right)\right) + S_V \tag{2.7}$$

$$\phi = \left(1-E\right)\left(X + S_h\right) + \left(E/B\right)\arctan\left(B\left(X + S_h\right)\right) \tag{2.8}$$

Where, Y is lateral force, longitudinal force or aligning moment, X is slip angle or longitudinal slip, B is stiffness factor, E is curvature factor, C is shape factor, D is peak factor, $S_h$ is horizontal shift and vertical shift factor in magic formula ($S_V$) is vertical shift.

## 2.4 Characterization of Vehicle operation over longer events

Different drivers use vehicles in typical environments, requiring different capability requirements of static and dynamic road load. Understanding that use phase for modelling vehicle operation independently is crucial for successful design and fair comparison. A driving cycle can model vehicle operation, including driving patterns, road type, speed levels, and daily driving range {Grunditz, 2016 #7;Jacobson, 2016 #60}.

### 2.4.1 Driving Cycles (DC)

The DC is a standardized testing tool for vehicle performance evaluation, used globally by EPA, UDDS, FTP-75, and WLTC.

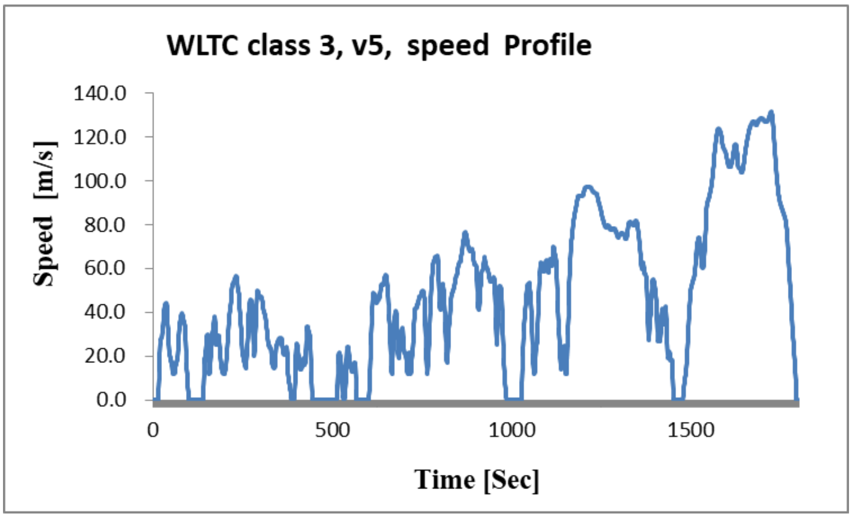


Figure 2.9: WLTC Class-3, V5 driving cycle for 1800sec duration

It certifies new designs and evaluates vehicle performance, with modified versions used since 1969 for pollutant emissions and fuel economy tests {Outlook, 2020 #132;Yildirim, 2022 #430}. The EPA developed the NYCC cycle for congested traffic in large cities, used in HEV and PHEV testing {Dhand, 2015 #156;Cinar, 2018 #158}. The Artemis project, involving 40 European research labs, developed three WLTC drive cycles for vehicles' power-to-mass ratios between 22 and 34W/kg, estimating pollutant emissions founded on data from European countries {, #557;, #279;Mohagheghi Fard, 2016 #633;Gidofalvi, 2008 #635}. DC data can be collected by on-road vehicles using sensors like GPS, cameras, Lidar, and radar connect microscopic vehicle activity to macroscopic modelling. DCs can be synthesized using extrapolation, selection, and simulation methods (Rashed, Li, Pang, Zhao, & Kheshti, 2021).

Time, speed, and acceleration-related derived parameters can be used to assess the vehicle's performance. Like total time, driven distance, and acceleration, these parameters can be combined together as level parameters. Relative time spent motionless, during acceleration, and between predetermined intervals are examples of distribution measurements. An oscillatory metric called Relative Positive Acceleration (RPA) is used to identify high power accelerations (Jiang, Shan, Du, & Pu, 2022; Jihui et al., 2022).

With RPA values ranging from 0.17 to 0.20 m/s2, test cycles SOC03 and Artemis Urban have the highest peak acceleration levels. The maximum RPA value and peak acceleration, both positive and negative, are found in the UC (LA92) cycle. The highest peak acceleration values are seen in the US06 and REP05 cycles; however, the RPA value and the average and standard deviation of acceleration are higher in the US06 cycle. The strongest braking acceleration occurs at high speeds on the Artemis Motorway cycles, which feature the highest acceleration values throughout the speed range. Accelerations and decelerations typically last longer than decelerations (Berjoza, Pirs, & Jurgena, 2022; D. Zhao et al., 2022), (Gebisa et al., 2022).

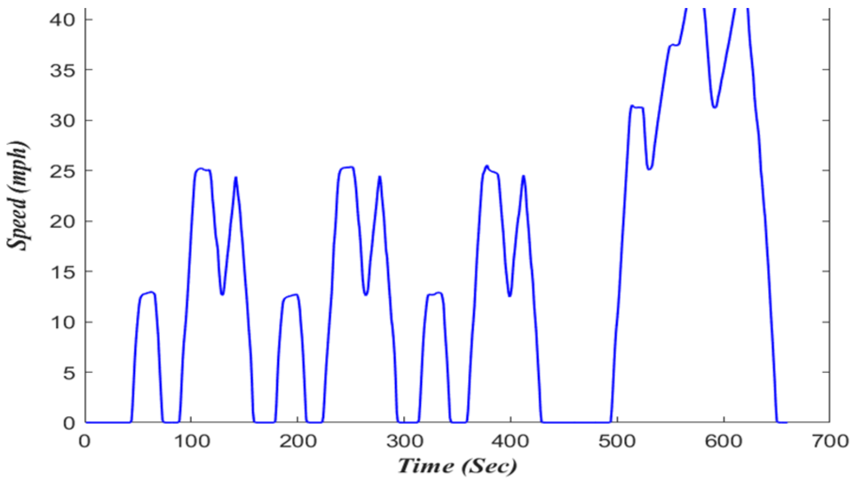


Figure 2.10: J1015 PRUIS sample real world drive cycle

To analyse and validate BEV design requirements, researchers and automakers use standard and legislative DCs. The torque, power, and braking characteristics of BEVs and ICEVs differ significantly, making correct calculation difficult. In response, some nations and producers have created customised DCs for every city or area (Khemri, Supina, Syed, & Ying, 2019; Peng, Jiang, Ding, & Tan, 2020; Wang, Wang, Song, Niu, & Hu, 2022).

Prior research has synthesised traffic data through the use of modal analysis, clustering, random selection, and pattern classification. Random selection is effective but requires extensive statistical analysis. Pattern classification is useful but requires accurate measurement. Modal method cycles fail to match real-data parameters (Chandrashekar, Agrawal, Chatterjee, & Pawar, 2021, Han, Wu, Gu, Ji, & Xu, 2021, Khemri et al., 2019; D. Zhao et al., 2022). Previous research on BEV DC synthesis has primarily examined the road conditions in industrialised countries, with minimal or no input from emerging and low-income countries. Driving patterns in the cities of emerging and low-income countries are significantly influenced by mixed use, single-lane vehicle composition, poor road quality, and lack of traffic signals (Gebisa et al., 2022), (Huzayyin, Salem, & Hassan, 2021), (Chandrashekar et al., 2021).

### 2.4.2 Driving Pattern

Although driving behaviour has a significant role in urban driving patterns, driving profile factors make it challenging to measure in a direct manner. Several approaches, such as the classification of driving behaviour as aggressive, average, or mild, have been put forth to ascertain driving behaviour from data. Research has demonstrated a relationship between acceleration, cycle velocity, and driving style; aggressive driving uses more energy. However, most of the previous studies focus on acceleration behaviour and ignore braking (Bouhsissin, Sael, & Benabbou, 2023; Ghandour, Potams, Boulkaibet, Neji, & Al Barakeh, 2021; Jonas, Hunter, & Macht, 2022), (Berjoza et al., 2022; Busho & Alemayehu, 2020; Huzayyin et al., 2021; Thomas, 2020; M. Zhao et al., 2021).

A DC can be condensed into the driving pattern, a 2-dimensional speed-acceleration function. Studies show that high acceleration levels and speed significantly impact energy consumption, even though the frequency is small (Singh, Pathivada, Rao, & Perumal, 2022).

### 2.4.3 Road Type and Speed Limit Specifications

Speed levels are crucial for determining vehicle top speed and are often assigned to urban, rural, or motorway categories. Differences in speed limits and definitions exist across regions. For example, rural speed is almost 100% at 80 km/h in Japan and Korea, while 100% in European countries is 100 km/h. Time spent at different speeds determines the adaptation of road classifications. Maximum grade levels for newly constructed and upgraded roads are advised by the Swedish Office of Traffic (M. Zhao et al., 2021) {Lasocki, 2021 #582;, #531}. Highway cycles typically have longer uphill and downhill segments, with 80% of uphill occasions shorter than 25s or 38s. Grade climbing time is twice acceleration time. Electric car driving ranges depend on typical travel distances. (Chandrashekar et al., 2021; Han et al., 2021).

## 2.5 BEVs Powertrain Sizing and Energy Management

The design process for electrified vehicles should focus on minimizing energy utilization and improving powertrain efficiency, considering typical operating profiles, EV components, driving characteristics, and constraints. A comprehensive analysis of multidisciplinary art and engineering is vital for fully BEVs, including technology, topology, dynamic characteristics, and optimal use of stored energy (Pierri et al., 2021; Xia et al., 2020) (Hossain et al., 2022; Jiang et al., 2022; Wang et al., 2022).

### 2.5.1 Energy and Power Management Strategies

PMS optimizes energy consumption, improves vehicle performance, prolongs battery life, and reduces system replacement costs. Control strategies for energy management in BEV applications include rule-based, optimization-based, and learning-based approaches, which align with existing EMSs (Huang et al., 2018) for EV applications.

Rule-based strategies are effective control methods for embedded processors, offering simplicity and real-time implementation. However, these strategies may be affected by driving conditions, necessitating other optimization techniques. Deterministic and fuzzy logic strategies are broadly used, including filter control, finite state machine, wavelet-transform, logic threshold control, optimized membership fuzzy control, adaptive fuzzy control, and predictive fuzzy control (Guo et al., 2019), (Elkamel et al., 2019).

Deterministic RB-EMS extracts rules from experience, focusing on optimizing energy expenditure and minimizing transmission loss. Finite state machine-based energy management use Bayesian Monte Carlo algorithms to estimate battery and ultra-capacitor capacity and power. FL-based EMS is adopted in BEV by lifetime degradation model. Adaptive FL-based EMS maximizes efficiency and minimizes battery current variation, but FL strategies cannot guarantee optimal performance {Wang, 2019 #325;Wang, 2019 #329;Wager, 2017 #154}.

Optimization Based (OB) EMS aims to find the optimal control sequence that minimizes a cost function while meeting dynamic global and local state constraints. Offline and online OB strategies are grouped based on prior knowledge of driving conditions. Offline power management is non-causal and globally optimal, using a widespread range of input information. Offline OB strategies use four types of problem-solving approaches: direct, indirect, gradient, and derivative free. Direct algorithms approximate optimal control problems as static optimization, while indirect algorithms are dynamic based on optimal control theory. Gradient algorithms can reduce calculation time and increase robustness {Kessels, 2008 #342;Song, 2015 #324;Yu, 2020 #300}.

Online strategy involves instantaneous optimization of offline EMS, with ECMS and MPC being popular real-time EMSs. ECMS offers best energy consumption reduction and battery stress reduction. MPC addresses DP algorithm issues and achieves global optimal control with advance driving profile information. OB method finds optimal power allocation for specific loads, but requires specific operating conditions. Improving online algorithm accessibility is an urgent problem.

Research evaluates energy management using various indicators, including battery life and system efficiency. The DP algorithm's performance is crucial, as it seeks the optimal result in reverse direction. Filter control performs better than other RB algorithms due to its softer and more detailed energy distribution. RB methods are faster than OB methods, but DP is difficult to apply to actual systems as it requires in advance knowledge of working conditions {Hussain, 2019 #357}, {Liu, 2019 #356}.

Table 2.3: Comparison of optimization strategies for energy management

| Technique | Key features | Limitations | Ref |
|---|---|---|---|
| Direct DP (off-line) | Global optimality Benchmark for other EMSs | Driving cycle information needed in advance, High computational cost | {Pourabdollah, 2014 #348} |
| Indirect PMP (off-line) | Global trajectory optimal control | Model approximation to reduce computation effort, Complex mathematics | (Guo et al., 2019) |
| Gradient (LP, QP, SQP, and CP) (off-line) | Fast computation | Complex mathematics Strong model simplification | {Panday, 2016 #345} |
| Derivative free (SA, GA, MOGA, PSO) (off-line) | Capable of local optima by stochastic solution search | Limited amount of iterations, Optimality not guaranteed | (C. Lin, Gao, Wang, & Chen, 2016) |
| ECMS (on-line) | Real time implementable Interpretation of single cost function | Only local optima DC sensitivity of equivalence factor | (Elkamel et al., 2019) |
| MPC (on-line) | Adaptive and predictive, Online close to global optima with less computational effort | Preview driving pattern and future driving information Prediction horizon sensitivity | {Zhou, 2017 #352} {Wang, 2019 #353} {Wang, 2019 #355} |
| Sliding mode control(on-line) | Robust to uncertainties and parameters change | Complex mathematic formulation | {Zhang, 2015 #354} |

### 2.5.2 Powertrain Components Sizing

Component sizes determine the powertrain’s potential and the success of the implemented PMS of the propulsion system. The methods of CS can be classified into experience-based, equivalent calculation, and OB sizing. Traditional methods are centered on past performance databases, design experience, or trial-and-error simulations. Equation-based sizing is grounded on vehicle operating circumstances and dynamic performance indexes. Both methods are simple but not optimal or sub-optimal when feasible domains are different or large. Solving energy management and CS problems separately is not justifiable as they are coupled by nature. {Huang, 2018 #279;de Castro, 2012 #245}, {Verbruggen, 2020 #217}. Researchers are increasingly using optimization algorithms to solve complex systems (CS) and control problems. These algorithms search for combinations of optimization variables in a multidimensional parameter space, aiming to minimize or maximize an objective function. The implemented algorithm for optimization should work with a powertrain model to achieve the best solution. This combination of CS and controller optimization is achieved through four coordination structures: iterative, sequential, simultaneous, and bi-level. Iterative optimization approach improve component size without considering control performance, but convex optimization size components using obtained management strategies. In sequential coordination approach, the component sizes should be optimized initaly and then controller optimization will be followed in a sequential manner.

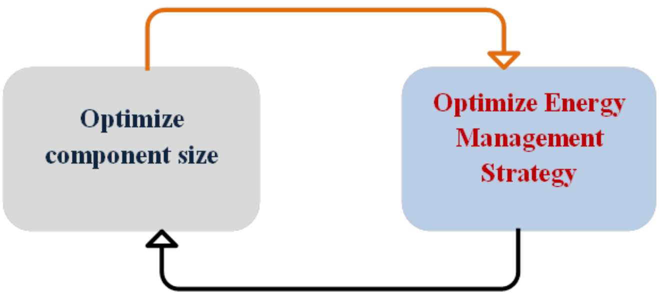


Figure 2.11: Iterative coordination of CS and control

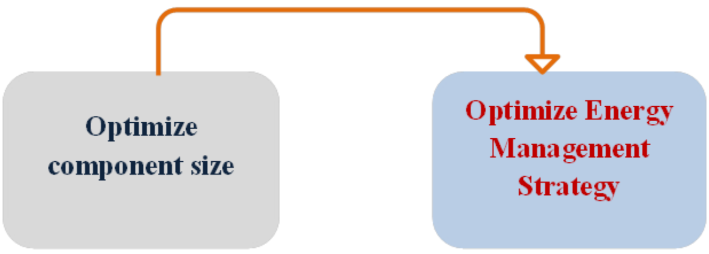


Figure 2.12: Design first, then optimize approach

A bi-convex model integrates powertrain components' size and operation to optimize energy consumption. Sequential optimization uses predefined strategies for control, not solving couple problems (Guo et al., 2019)

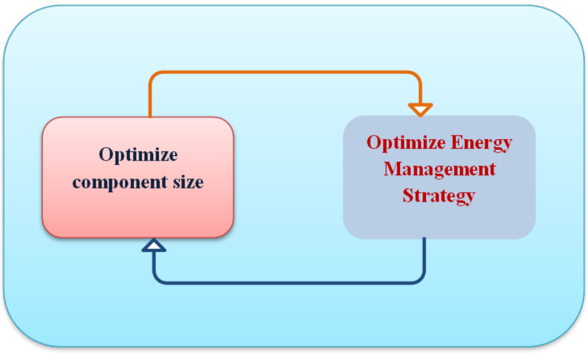


Figure 2.13: Nested Bi-level coordination

Nested bi-level coordination employs two loops in a nested optimization framework, while the outer loop for component sizes optimizing and the inner for designing optimal controllers. An integrated sizing and energy management framework combines an inner and outer layer to maximize vehicle performance, achieving optimal torque allocation via dynamic programming and desirable powertrain parameters on the outer layer (Huang et al., 2018).

Some authors have used DP and Pareto optimization algorithms to achieve system-level optimality in powertrain parameters. They used two loops that are nested to solve component size problems and control problems using DP.

Simultaneous coordination optimization involves finding optimal component sizes as well as control in one loop. A multi-objective optimization was proposed, incorporating battery, super capacitor, and vectored fuzzy inference systems {Dharumaseelan, 2019 #295}.

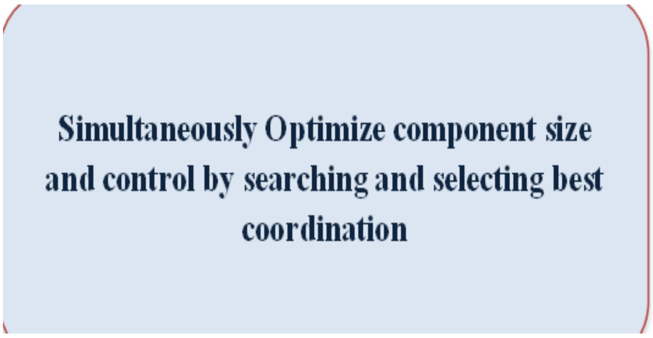


Figure 2.14: Simultaneous coordination of component size and control

Table 2.4: Comparison of four optimal CS structures

| Coordination | Optimization Algorithm | Key Features | Ref |
|---|---|---|---|
| Iterative | DP | near-optimal offline | (Zimmermann, 2016) |
| Sequential | DP; PSO | It is simple but sub-optimal; offline | (Wang, 2018) |
| Nested | GA | Globally optimal with a heavy computational burden; offline | (Kouchachvili et al., 2018) |
| Simultaneous | SDP; PCOA CO | Globally optimal; time-consuming and mathematical challenge; offline | (De Castro, 2012, Erb, 2016) |

### 2.5.3 Modelling the Simulation Set up

Vehicle dynamic research primarily focuses on virtual modelling followed by simulation, but prediction models, design methodologies, and tools that can support BEV's development by considering relevant factors and components are needed.

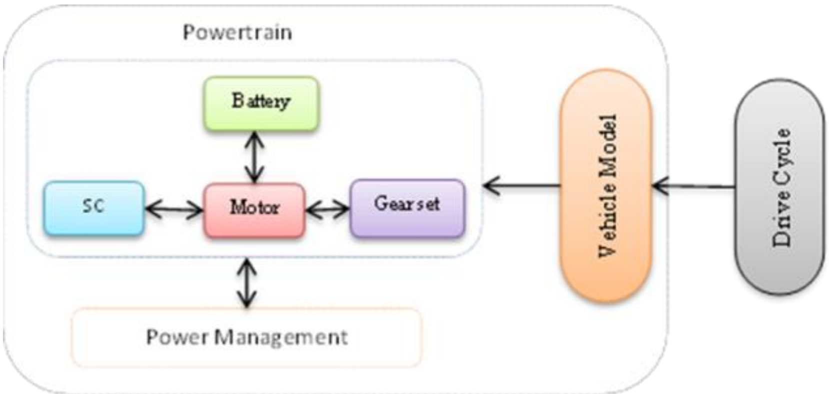


Figure 2.15: Back ward-facing modelling approach

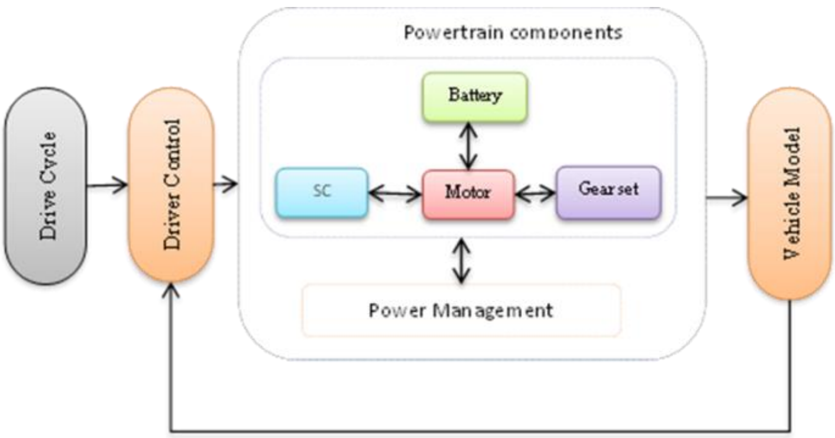


Figure 2.16: Forward facing modelling approach

Recent research has shown promising results in dynamics of vehicle and control research without the problems of full-sized testing. Modelling approaches for EV power train development include forward-facing and backward-facing models. Backward-facing models use motions as inputs and calculate the demanded power for specific drive profiles (Sharmila et al., 2022; R. Yuan et al., 2020). Forwards-facing modelling shown on Figure 2.17 is perhaps the most natural approach for engineers, taken by default, which the 'inputs' are forces and torques; the 'outputs' are the resulting motions. This approach gives a designer lot of flexibility in designing the components due to access of internal variables.

## 2.6 Battery Packaging

Nowadays, it's common practice to develop BEVs from commercially available car models by taking use of their lower costs and more developed production platforms. Electric motors, large battery packs, controllers, energy management systems, cabling, and mounting components all entirely different from the original powertrain are used in BEV conversions. BEV drive train components should be placed in unused spaces without major modifications of BIW concept, when adopting existing automotive body and chassis architecture. The ICEV platform should accommodate the evolutionary powertrain of BEVs, with axle housings being ideal for motors and transmissions. To make battery packs cost-competitive and market penetration, modifications to size of battery cell, layout, and packaging clearance can make them compact, lightweight, and thermally stable (Arora, 2017; Outlook, 2022), (Sandeep, Shastri, Sardar, & Salkuti, 2020) , (Krüger, Spohr, Merdivan, & Urban, 2022; Pierri et al., 2021).

Cells of lithium-ion battery that are the most preferred type for BEV applications, available in pouch, cylindrical and prismatic architectures. The packing density of smaller cylindrical cells is higher, while pouch cells have two times less packing density (Nicoletti, Köhler, König, Heinrich, & Lienkamp, 2021). The packaging compactness affects thermal performance, with increasing cell-to-cell spacing causing 1°C loss of temperature in steady-state (M. Li et al., 2020; Martellucci & Krishna, 2021). Prismatic cells are simple for assembly, while pouch cells require special precautions to prevent stress development and delamination needed for electrode layers. BEV designers face challenges in maintaining satisfactory integrity of body structural and battery pack during car accident. Therefore, it requires robust design to address thermal runaway, crash safety and vibration isolation at cell and modular levels (Krüger et al., 2022).

Table 2.5: Battery pack's long term performance and USABC goals (Arora et al., 2018)

| **Parameter (units)** | **Minimum target of commercialization** | **Long term target** |
|---|---|---|
| Specific energy @ discharge rate of C/3 (Wh/kg) | 150 | 200 |
| Discharge specific power @ 80% (DOD)/30s (W/kg) | 300 | 400 |
| Regeneration specific power @ 20% (DOD)/10s (W/kg) | 150 | 200 |
| Energy density @ C/3 discharge (Wh/L) | 230 | 300 |
| Power density (W/L) | 460 | 600 |
| Specific power to energy ratio | 2:1 | 2:1 |
| Nominal recharge time (hours) | 6 | 4 |
| Life (years) | 10 | 10 |
| Cycle life @ 80% DOD (cycles) | 1000 | 1000 |
| Power and capacity degradation (%) of rated spec | 20 | 10 |
| Selling price of 25,000 units @ 40kWh ($/kWh) | <150 | 100 |

Battery packs of BEV should be placed in unused areas to minimize mechanical stresses and fatigue on the mounting frame. They should be located outside the occupants' compartment to protect the battery from potential impacts (Arora et al., 2018; Martellucci & Krishna, 2021). The ideal space is at the vehicle's middle part beneath the floor, but limited ground clearance in passenger vehicles requires careful design (Sandeep et al., 2020; Yang, Fang, Li, & Xie, 2019). The front engine bay or bonnet offers weather protection but faces safety issues like high voltage shock and battery explosion (Pierri et al., 2021; Razak et al., 2019). The car's packaging should be considered for providing occupant accommodation space while granting their protection from car accident. Accordingly, the Seating Reference Point coded by SgRP being the most crucial point for ergonomic positioning. The SAE's 95$^{th}$ percentile of male manikin is taken for ergonomic positioning, determining the volume occupants should control the vehicle or sit as passengers. Visibility is set by angles over and below the horizontal datum line, with an upper angle of 14 degrees and 4 degrees for lower angle. Body components must ensure structural integrity, restrict deflection, and maintain static stiffness while minimizing mass (HAILU & Kibret, 2016; Niroomand, Bach, & Elser, 2021). The vehicle's underbody stiffness for torsion should be assessed esentially to meet safety requirement and the induced value should be as low as 200 kNm/rad. It's essential to avoid body resonance, especially in the frequency range of suspension's resonance and cabin noise. Safety characteristics in vehicle design are vital to maintain passenger compartment integrity and reduce deceleration and injuries (Ping et al., 2022, Pierri et al., 2021, Sharmila et al., 2022, Wang and Zhao, 2016).

The electric and electrical systems of the car were the subject of numerous earlier studies, but the handling and comfort of an EV conversion was not one of them. As a result, it's unclear how the vehicle's suspension system would function after an EV conversion, as well as how well the passenger compartment will be isolated from the car's severe road profile. It is possible for BEV conversions that entail the retrofitting of new evolutionary technology to incur additional or decreased weight. Additionally, provided the design and development are completed without significantly altering the current chassis and body platform, the BEV conversion may be feasible. Utilising the area inside the chassis that was previously occupied by the benchmark vehicle's traditional power plant is one such approach.

Any change in the amount of weight on the chassis during packaging design will result in a shift in the weight distribution between the front and rear axles of the vehicle. Due to the fact that the current suspension system tuning was not created with the increased weight and load distribution at the front and rear axles in mind, this may affect the vehicle's handling performance and ride comfort. Numerous earlier research, mostly pertaining to the traction and yaw stability control systems, were discovered to concentrate on enhancing the stability of EV conversion during manoeuvring. In EV yaw stability control, the emphasis is on yaw motion control, which involves managing the motor's operation, and traction control system, which regulates the electric motor to prevent wheel skidding when accelerating, thereby guaranteeing complete control over the vehicle.

## 2.7 Summary of Literature Review

Electric motors offer high performance and energy conversion efficiency, making BEVs attractive for sustainable transportation. However, the shift to electrified transportation presents challenges due to lack of standardized development procedures, inconsistent design methods, and unknown technical details. To alleviate these limitations, innovative designs and manufacturing methods are required to utilize limited space for BEV powertrain components.

The design process for BEVs involves multidisciplinary engineering and art, integrating components, driving characteristics, energy consumption, safety, ergonomics, and design. BEV system architecture consists of mechanical, electrical, electronic, and information subsystems. Multiple motor 4WD configurations offer better speed -acceleration, but require complex algorithms. They are heavy and costly. Concentrated propulsion systems offer smaller footprints, lower costs, and simpler control algorithms.

Lithium-ion batteries are ideal for BEVs due to their high power-to-weight ratio and energy efficiency. DC machines benefit from an easy control, but their application in BEVs is limited due to performances, wear susceptibility and higher cost. PMSMs offer superior efficiency, torque, specific power, maintenance, and controllability. These motors are also suitable for implementing appropriate control strategy for regenerative braking. Besides, regenerative capability is highly influenced by the capacity of selected energy storage, the driving profile and driver behaviour.

The vehicle's dynamics are studied using mathematical, steady-state, multi-body dynamics, and detailed models. A multibody dynamics model was found suitable for multi-degree of freedom vehicle dynamics. Concentrated mass longitudinal model is capable of modelling road slope and minimizes computational burden. BEV functional models rely on backwards-facing models for steady-state functions, whereas forwards-facing models require driver models and controller design. The most frequently used models are time-based that are implemented to represent the vehicle and its operating profile characteristics.

Accurate control strategy is necessary for optimal powertrain sizing and dynamic assessment of BEVs. Standard numerical models are needed for analysing the demand energy, efficiency and cross-coupling dynamics.

Prior research on the synthesis of BEV DC has primarily depended on data from developed countries, with few contributions from developing nations like India. Scholars and manufacturers employ standard or legislative DCs; nonetheless, precise approximation may be challenging, given the notable distinctions between BEV and ICEV torque, traction power, and braking attributes.

The design of BEV systems require careful consideration of topology and power management strategies to optimize component size. Control based on rule sets is simple and time-efficient in embedded processors. OB methods find optimal power allocation but require specific operating conditions.

Battery pack layout in EVs is unsolved issue involving factors like space, collision safety, and heat dissipation. The most reported placement is the chassis, which can compress space and affect airflow. Analyzing the pack's architectural impact on vehicle aerodynamic flow and pressure field is also crucial, since it affects the energy demanded and stability of BEV. CFD has been used to study aerodynamic body shapes, calculating accurate turbulence models using high-performance computers.

## 2.8 Research gap

- The dynamic characteristics of BEVs are significantly different from those of internal combustion engine vehicles, making them vulnerable to various factors affecting their performance, efficiency, and safety. Despite the growing interest in BEVs, there is a lack of research on the specific dynamic characteristics of BEVs in developing countries like Ethiopia, where driving patterns and infrastructure differ significantly from those in developed countries. Existing studies have focused primarily on European or North American driving profiles, neglecting the diverse driving conditions found in Africa.
- Standard and legislative DCs fail to represent the operating profile of a typical city or region. No investigations have been conducted on connected urban and suburban settings, such as emerging large cities like AA. There is a need to develop a comprehensive understanding of the driving profile in Addis Ababa, including speed distribution, acceleration, braking patterns, and traffic density, which will allow for more accurate simulation and validation of BEV dynamics.
- Most existing studies on BEV dynamics have focused on idealized powertrains, neglecting the impact of real-world powertrain designs on vehicle performance and efficiency. Most previous studies on BEV dynamics rely on theoretical models or simplified simulations. A data-driven approach is needed to validate the accuracy of these models and provide more reliable predictions of BEV behavior.
- Weather conditions, road quality, and altitude variations can significantly affect BEV performance and efficiency. These factors need to be incorporated into the analysis to provide a more comprehensive understanding of BEV dynamics in Addis Ababa. Driver behavior plays a crucial role in shaping vehicle dynamics. Investigating driver behavior in Addis Ababa, such as acceleration and braking patterns, can help improve the accuracy of simulations and reduce the risk of accidents.
- The placement of a battery pack in a limited space could result in protruding, compressing space, changing car shape, and impacting airflow. The effect of pack placement and architectural variation on energy consumption and dynamic characteristics was not studied well. Aerodynamic characteristics, battery pack integration with body structure and its stiffness, suspension performance addressing the trade-off in ride comfort and stability not assessed well for converted BEV.

# CHAPTER THREE

# METHODOLOGY

## 3.1 Description of the Study Area

The energy consumption and efficiency of BEV can be improved by improving the component's technology, rectifying topology/structure, and allocating appropriate dynamic control method. The improvement is crucial for achieving mission objectives that depends on the powertrain components being assembled and sized properly. This research explores the integration of propulsion system electrification in vehicle sizing and synthesis, aiming to reduce mass and space claim, while improving efficiency and dynamic performance. Using GPS data, the study looks at the impact of driving habits and patterns of AA and its surrounding areas on BEV energy consumption and powertrain efficiency. Its objectives are to investigate CS method for this integration concept, design an efficient battery pack architecture and assess its impact on aerodynamic characteristics, ride comfort and stability of converted BEV based up on BIW concept.

## 3.2 Source of Information and Benchmark Data

This dissertation uses sources like Google Scholar, Scopus, and the websites of Automotive OEMs, SAE, EPA and testing and licensing organizations. The benchmark data was collected from the best-selling BEVs based on homologation compliance. Homologation is a process of testing and certification to facilitate international technical harmonization and streamline internal market restrictions of vehicles used on public roads. The benchmarked vehicles are tested and certified by manufacturers, SAE and EPA as well as approved by their corresponding countries' authority.

The driving profile data was collected from AA and its suburbs, Ethiopia using GPS instrumented six vehicles.

## 3.3 Research Design

The interdisciplinary engineering process for creating BEVs is examined in this study. It integrates driving characteristics, operational circumstances, ergonomics, energy usage, and componentry to balance end user expectations with final design.

Since the use of cutting-edge computer technology makes virtual tools potent in the realization of physical systems, modelling and simulation form the foundation of this study's methodology. To gather trustworthy field data for driving cycle generation, an experimental investigation was carried out to find affordable and dependable instrumentation. The flow chart on Figure 3.1 presents the overall methodological approach that was used.

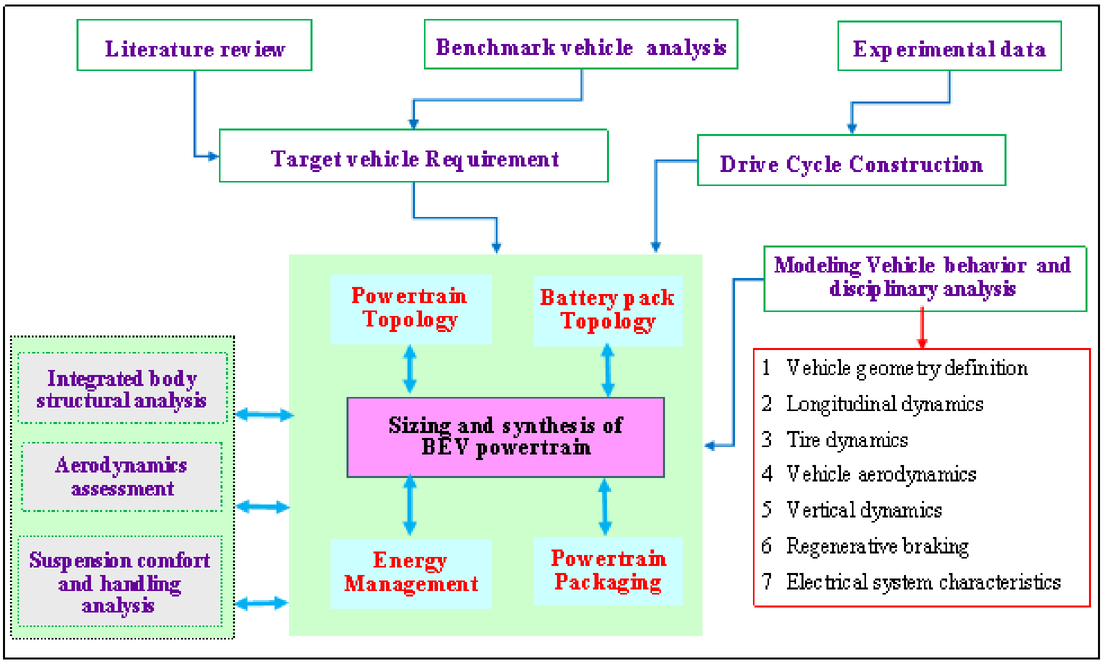


Figure 3.1: Schematic flow representing the implemented methodological framework

A simulation-based SE approach was used to design vehicle powertrains and assess dynamic characteristics of the BEV. This comprehensive methodology links customer expectations to final component specifications and validates recommended configurations. The proposed methodology integrates powertrain in vehicle sizing concept with the help of Bi-level modelling approach. This method effectively assesses several design iterations using a simulation-based technique, speeds up the design of vehicle dynamics, and optimizes targets at the vehicle, sub-system, and component levels.

To this end, a methodological framework developed, which forms the building blocks in this research contribute towards model-based powertrain sizing, battery cell packaging, and assessment of structural integration with body structure, aerodynamics characteristics, and suspension performance with regard to ride comfort and stability of converted BEVs focusing on a class of system development and vehicle dynamics analysis.

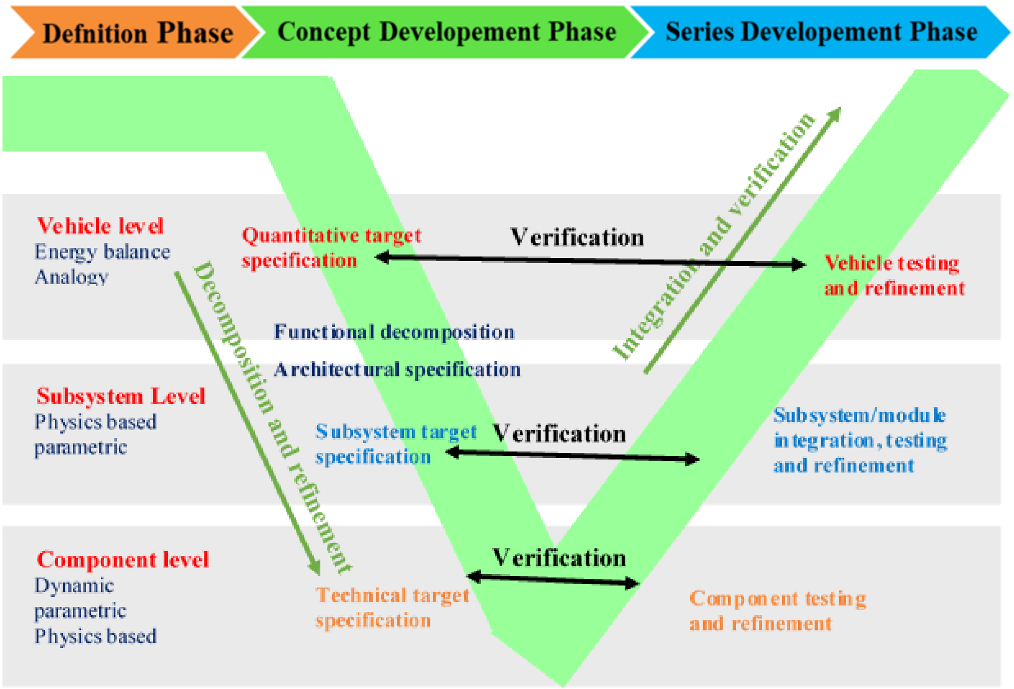


Figure 3.2: The V-chart methodology

- ✓ Top vehicle level models were modified with modular weight estimation and energy based modelling approach for analyzing of point and mission performance
- ✓ The implemented approach for sizing and dynamics characterization was made possible by the capturing of sub-system performance parameters using bi-level, physics-based parametric models that were connected to the requirements at the vehicle and mission levels.
- ✓ The definition of EV propulsion designs is sufficiently adaptable to take into consideration different topologies and their effects on the vehicle and mission levels. Optimal operating conditions for every topology type are obtained by integrated PMS.
- ✓ The process of sizing facilitates the shift from high-level to granular investigations, enabling the dynamic models to catch important transients.
- ✓ Representative DC typical for AA and its suburbs, Ethiopia was modelled using GPS collected data.

Various computer programs were used for modelling and analysis of the vehicle, its sub-systems and components such as MATLAB/Simulink, CATIA, MS-Excel, ANSYS and commercial Phoenx.

Data analysis verification and validation were conducted at multi-level based up the nature source and type of data. Statistical analysis of experimental data was performed for confirming its representativeness to the whole population and filter out false data. Correlation and regression analysis are performed at various instances in this work. Physics based parametric, mathematical and numerical models were verified by employment of virtual experimentation. The synthesized AASU DC validated based up on experimental data and standard dive cycles. The generated concept vehicles and powertrain layouts were validated by comparing with the results of benchmark analysis, manufacturer and homologation index standards. Furthermore, some of the results are validated against published experimental work.

## 3.4 Benchmark Analysis and Target Definition

The benchmark data for fully electric vehicles was collected from over thirty SAE and EPA-indexed models that have been the top-selling light-duty BEV models globally since 2010. This served as a point of reference. The majority of crucial design and performance information has been obtained mostly from automakers. Table B.1 lists all of the car models from various manufacturers and categories, together with their characteristics, the data that was gathered, and the references that correspond with it. Vehicle size, passenger capacity, curb weight, top speed, acceleration time, approved driving range, and energy consumption are the most crucial factors.

The current car models are divided into three groups, small, medium-large (midsize), and high performance, based on the European passenger car category to facilitate benchmarking even more. The small cars, known as B or economy, are suitable for urban driving. The midsize segment, C, D, and E, is wider class from economy to executive and high performance includes luxury and sport segments. The first three segments of European passenger vehicles categories account the largest share of the global passenger car market.

The economy segment cars are the most preferred by most middle level people living in AA and the surrounding small towns. Since small and midsize economy cars are ideal for Ethiopia and emerging markets, small (urban) and midsize (long range) cars conceptualized to address customer concerns. Although, limited high performance BEV models, like Tesla

S long range plus, are available on AA roads, midsize (High performance) car conceptualized for comparison and analyse conversion design capability.

The three concepts aim to provide four + cargo transportation in Ethiopia and emerging economies, requiring efficient packaging to maximize interior space and minimize cost, weight, and aerodynamic drag. The concepts must qualify top vehicle-level entities, including attributes, functions, and requirements for vehicle development. Primary needs include performance, drivability, energy consumption and driving range and while maintaining acceptable ride comfort and stability for urban and suburban driving. These qualitative targets were specified by quantitative measures including top speed, acceleration time, maximum grade negotiable, and driving range per full charge.

The next section discusses three concept light duty passenger BEVs, each with specific qualitative and quantitative performance requirements shown in Table 3.1.

Table 3.1: Three concepts of midsize BEVs

| | **Number of seats** | **Vehicle class** | **Top speed** | **Accelerati on time** | **Grad ability** | **Range** |
|---|---|---|---|---|---|---|
| City | 4 | Small car | Medium | Medium | Medium | Medium |
| Highway LR | 4-5 | Midsize | High | Short | High | Very Long |
| Performance | 4 | Midsize | Very High | Very Short | Very High | Long |

### 3.4.1 Curb Weight and Geometric Parameters

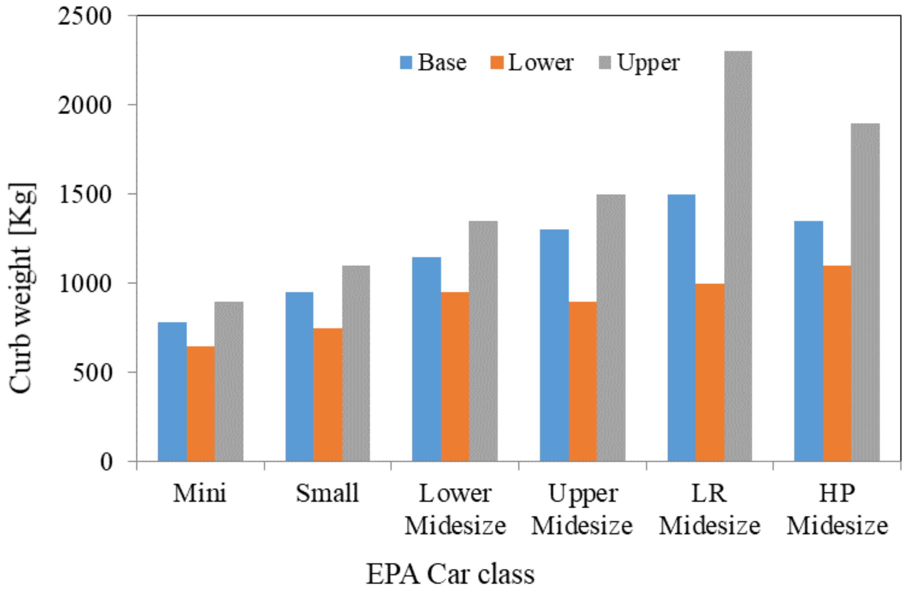


Figure 3.3: EPA categorized car classes based on curb weight of each vehicle

Data on curb weight is available for all BEV models. In general, the small cars have the lowest masses: around 750-1100 kg and the standard midsize cars' weights are 900-1500 kg. The high range midsize models weigh between 1000-2300kg and the high performance models in the range of 1100-1900 kg as shown in Figure 3.3.

The purpose and external dimensions determine a vehicle's class that can be represented by overall exterior dimension of all passenger cars as-

$$V_{V,ova} = L \times W \times H \tag{3.1}$$

Where, $V_{V,ova}$ is the overall exterior dimension, L is the overall length, W is the maximum width and H is the maximum height of the vehicle.

Passenger vehicles are now categorized into compact, mid-sized, and premium sedans. Automakers use "module" or "platform" strategies to avoid creating new chassis for each variant. OEMs have limited chassis and powertrain configurations, with economical options at lower end and sophisticated, luxurious, and expensive options at upper end.

Accordingly basic exterior dimensions of each concept are selected from lower to upper limits with in standard class to meet OEM packaging requirement.

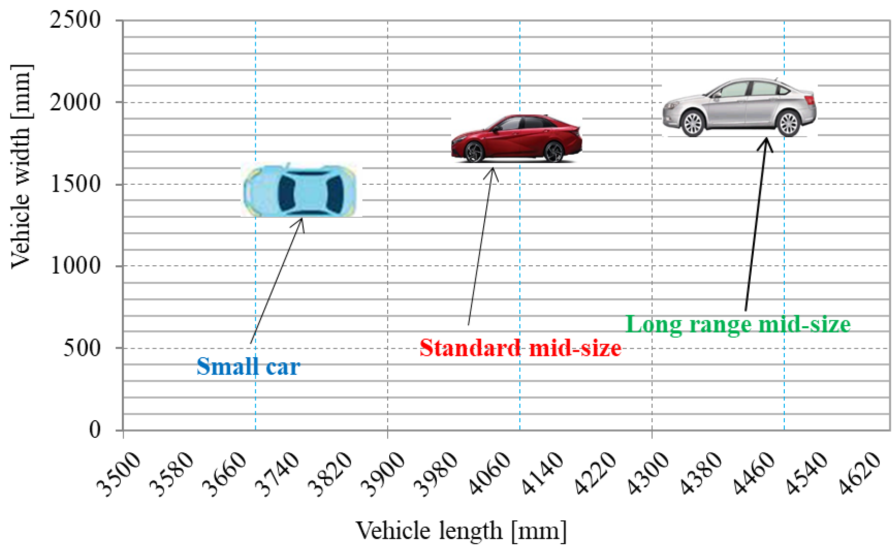


Figure 3.4: Exterior dimensions reference BEVs since 2010 with their class or category

The concept city car's gross weight is set at 1200 kg, representing both small (higher range) and standard midsize (base range) cars. The highway car's long-range capability weighs 1800 kg, reflecting midsize (higher range) car values. The high-performing car's curb weight is set at 2000 kg. The small cars have a footprint of 2.1m$^2$, providing ample passenger and cargo space for city taxis and highways. Midsize cars have a footprint of 2.25m$^2$, with a wheel base of 60% of vehicle length. The static weight distribution for BEVs ranges from 42:58 to 50:50, with 44:56, 48:52, and 50:50 weight distributions assigned for small, long-range, and high-performance cars.

Height (h) of COG can be determined experimentally based on given vehicle geometry for any inclination θ or for maximum inclination ($\theta_{max}$).

$$\tan\theta_{\max} = \frac{l_2}{h} \tag{3.2}$$

However, as a starting point it can be estimated to be 30-40% of total length, with 38% for small and long range cars and 34% for sport cars. Data on vehicle front area has shown linear relation with vehicle class and approximately 86% of the product of height and width.

Top-selling BEVs in 2020 use tire sizes ranging from 15 to 20 inches, with high-pressure tires used for passenger vehicles to minimize rolling resistance. City cars used 16 inch tire, and long range used 18 inch tire with 55% aspect ratio to withstand 2.6bar, aim to reduce road loads for improved energy consumption.

### 3.4.2 Performance attributes

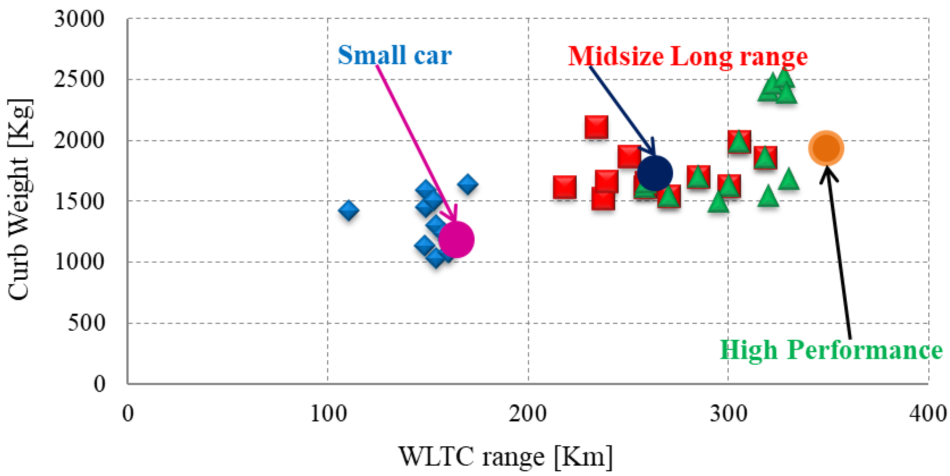


Figure 3.5: The relation between driving range and curb weight for high performance and long range BEVs

Small-midsize models typically have top speeds of 120-160 km/h, with high-performing models reaching 190-249 km/h. Most countries have a top speed limit below 120km/h. The maximum achievable speed for small concept cars is 130 km/h, while long-range highway cars reach 160 km/h, matching the fastest midsize BEVs. The acceleration time for high-performance models is shortest at 3s-6s, while small cars have a larger spread of 8s-13s. City cars maximum time is set to 10s, while highway cars have a maximum time of 6s.

The WLTC range for small cars is 69-150 km, midsize cars 162-200 km, long-range models 250-402 km, and high-performance cars 200-600 km. The concept city car has a WLTC range of 160 km, 250 km for standard midsize cars, covering 90% of average daily driving distances. High performance long range cars have a WLTC range of 350 km, matching Model S models. The concept vehicles' grad ability is not based on typical BEV values, but on specific requirements. They should start in 25% uphill grade, drive at 88.5 km/h in 3% grade, and 72.4 km/h in 6% grade. Long-range and high-performance cars should sustain 120 km/h at 6%, while city cars must negotiate 90 km/h. Table 3.2: depicts dimensions and performance attributes of the three concept cars.

Table 3.2: Performance requirements and relevant parameters of the three concept BEVs

| Parameters | City car | Long-range | High performance |
|---|---|---|---|
| Number of Seats | 4 | 4-5 | 4 |
| Curb weight [kg] | 1200 | 2000 | 1800 |
| Acceleration time (0-100 km/h) [s] | 10 | 6 | 4 |
| Top speed [kph] | 130 | 160 | 180 |
| WLTC range [km] | 160 | 250 | 350 |
| Drag coefficient ($C_d$) | 0.35 | 0.3 | 0.28 |
| Area [$m^2$] | 2.05 | 2.3 | 2.0 |
| Tire size [in] | 16 | 18 | 19 |
| Tire pressure [bar] | 2.5 | 2.6 | 2.7 |
| Starting grad ability [%] | 25 | 25 | 25 |
| Grad ability (Speed at grade) %[kph] | 6 (90) | 6 (130) | 12 (130) |

## 3.5 Methods and Materials for Synthesising AASU DC

### 3.5.1 Route Selection

AA is surrounded by small towns such as Bishoftu (east), Sandafa (north), Sululta (north-west), Holeta (west) and Sebeta (south), with 60 km of suburban routes from the city centre along cross-country main roads. Public transportation using city buses is preferred by most low-income people and extends to the five towns as destinations starting from the central station (stadium), operating daily from 5.00 am to 9.00 pm. Furthermore, passenger cars are the preferred means of transport by those in the middle-income class living in AA and looking for low-cost accommodation in neighbouring towns (Busho & Alemayehu, 2020). Routes were selected so as to represent typical driving patterns observed in the study area considering home-to-work trips, population differences and road classifications (Gebisa et al., 2022).

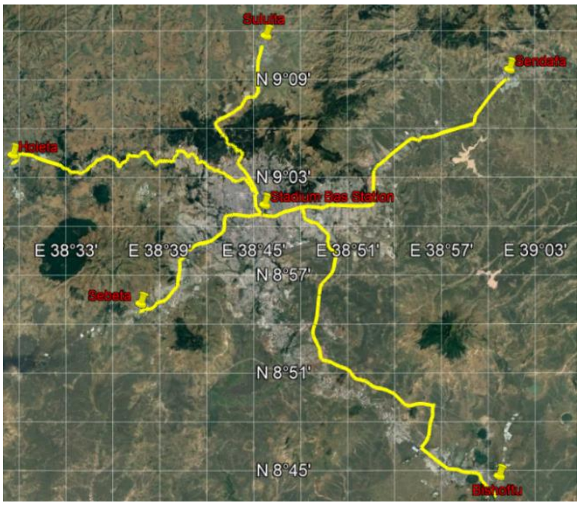


(**a**) Selected route for the study


(**b**) AA inner city road network

Figure 3.6: Road network of the study area of AA and suburbs.

Accordingly, the inner city routes covering all types of routes and trip segments and extending to all five neighbouring towns were selected, marked in yellow in Figure 3.6(a). The inner city road network is shown in Figure 3.6(b). The longest route, which also features an expressway, stretches from AA to Bishoftu. Overall, this route is 59.8 km long and is comprised of a 19.8 km expressway, a 15.9 km suburban ring road and a 4.8 km feeder road, while the remaining 10.6 km and 8.7 km are the AA and Bishoftu inner city routes respectively.

### 3.5.2 Data Collection and Processing

Initially, the driving profile data files were recorded by GPS at a frequency of 0.1 Hz using six vehicles: three from each passenger and city bus category. The collected raw data were filtered and de-noised to minimize errors and to obtain a smooth data, and then concatenated into a unified dataset using MATLAB code, as shown in Figure 3.7(a). Initially a car speed below 1 m/sec was changed to 0 m/sec as its real applicability was insignificant, while speeds above 120 km/h were adjusted to the allowable maximum speed limit of 120 km/h. Next, data corresponding to the dwell time where vehicles stop for a duration of more than 180 seconds were removed. Higher acceleration values due to a GPS error and sudden peaking speed were considered outliers. A void in speed values and alternating zero speed values may be recorded due to a GPS sensor defect or by being blocked by tall buildings (Y. Liu & Zhang, 2021; Rashed et al., 2021; M. Zhao et al., 2021). The outliers of void and false data were treated using shape-preserving cubic interpolation, followed by the Bayes wavelet signal de-noising method to smooth and transform to 1 HZ.

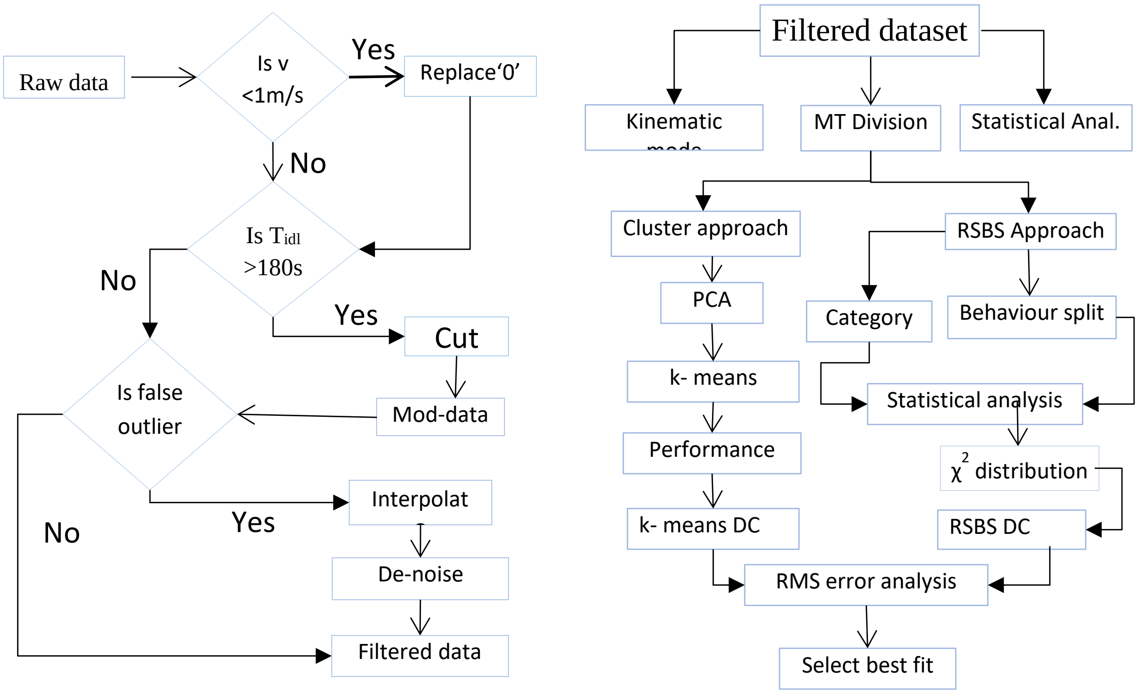


(**a**) Flow chart of data processing to filter noise

(**b**) Development methods of DC

Figure 3.7: Systematic flow chart of data filtration and driving cycle development.

Finally, processed data equivalent to an approximate distance of 1,390.47 km were determined for use in DC development methods, as shown in Figure 3.7(b). Table 3.3 summarizes the processed data, where zero drift and void are only 0.5 % and 0.11 % respectively. 8.18 % of data were removed due to the long dwell time. The speed-acceleration distribution of the filtered and unified dataset can be seen in Figure 3.8.

Table 3.3: Unified dataset before and after filtration process.

| Data type | Total number of data | Percentage of data (%) |
|---|---|---|
| Raw data | 179894 | 100.00 |
| Long dwell | 14724 | 8.18 |
| Zero drift | 900 | 0.50 |
| False zero | 200 | 0.11 |
| Removed | 15824 | 8.80 |
| Filtered | 164070 | 91.20 |

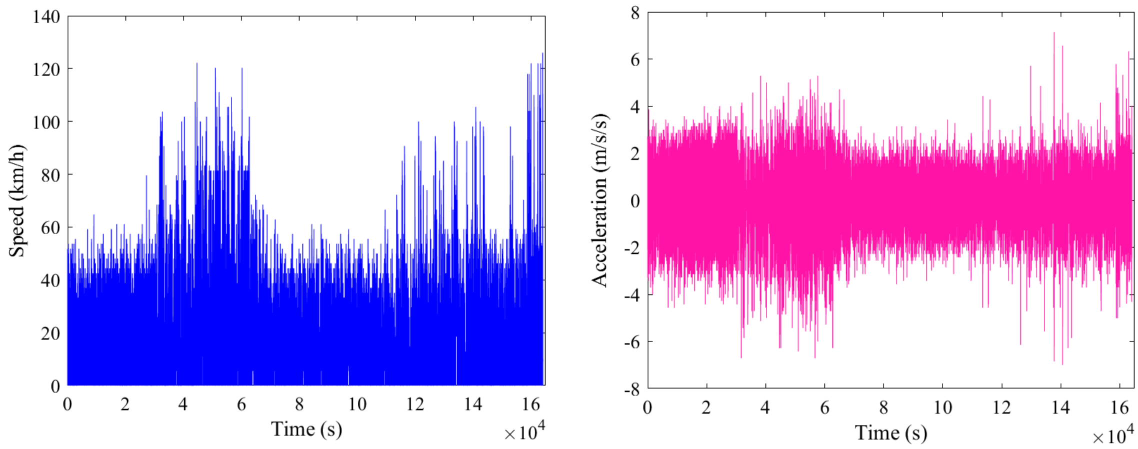


(a) Driving speed distribution (b) Driving acceleration distribution

Figure 3.8: Speed-acceleration distribution of the unified and filtered dataset.

### 3.5.3 Driving Feature Definition and Pattern Characterization

Numerous studies have proposed different calculated parameters related to speed-acceleration distribution and time proportion in order to define driving features. They are categorised as level, distribution and oscillatory measures (Rashed et al., 2021).

However, there is no clear evidence of relevant parameters to predict the power and energy demand of a BEV. In this study, the twelve most prominent features with more variability and less of a relationship between them were selected, after box plot statistical correlation analysis had been performed on seventeen feature parameters presented in Table 3.4.

Table 3.4: Features used to characterize AA and its suburban driving pattern.

| No. | Feature category | Driving features | Symbol |
|---|---|---|---|
| 1 | | Average speed (Km/h) | $V_{ave}$ |
| 2 | | Maximum speed (Km/h) | $V_{max}$ |
| 3 | | Average running speed (Km/h) | $V_{rave}$ |
| 4 | | Average acceleration ($m/s^2$) | $a_{ave}$ |
| 5 | Level measures | Maximum acceleration ($m/s^2$) | $a_{max}$ |
| 6 | | Average deceleration ($m/s^2$) | $d_{ave}$ |
| 7 | | Maximum deceleration ($m/s^2$) | $d_{max}$ |
| 8 | | Total duration (s) | $T_{tot}$ |
| 9 | | Approximated distance (km) | $D_{lng}$ |
| 10 | | Relative positive acceleration ($m/s^2$) | RPA |
| 11 | Oscillatory measures | Positive aggressiveness index ($m^2/s^3$) | PAI |
| 12 | | Relative negative acceleration ($m/s^2$) | RNA |
| 13 | | Negative aggressiveness index ($m^2/s^3$) | NAI |
| 14 | | Time percentage of idling (%) | $T_{idle}$ |
| 15 | Distribution measures | Time percentage of cruising (%) | $T_{cruz}$ |
| 16 | | Time percentage of acceleration (%) | $T_{accel}$ |
| 17 | | Time percentage of deceleration (%) | $T_{decel}$ |

When characterising driving patterns, the impact of driving behaviour mainly as a result of the driver's driving style must be included (Singh et al., 2022). Although it is difficult to measure driving behaviour, there is a high correlation between driving style and acceleration-related feature parameters. Hence, acceleration-related features including $a_{ave}$, $d_{ave}$ PAI, NAI, RPA and RNA were analysed to define different driving behaviours to characterise the driving pattern. RPA and RNA were considered principal components since they have a high correlation with the BEV energy consumption rate and the regenerative potential of braking kinetic energy per range respectively (Kabalan, 2020; Lasocki, 2021; Zhou, Zhao, Cheng, & Min, 2019). RPA and RNA are defined as (Rashed et al., 2021):

$$RPA = \int V(t)a(t)^{+} \Big/ \int V(t)dt \tag{3.3}$$

$$RNA = \int V(t)a(t)^{-} \Big/ \int V(t)dt \tag{3.4}$$

where V(t) is speed, $a(t)^{+}$ is positive acceleration, $a(t)^{-}$ is negative acceleration and dt is the change in time.

### 3.5.4 Trip and Micro Trip Division

A trip cycle here covers the driving profile from the dispatching centre to the destination without a prolonged stop duration. For AA intercity and feeder routes, the segmentation of trips was based on a long stop of more than 1200 s. However, a trip on the ring road and expressways was extracted by matching the google map location with data points. Trip data points established from criteria set to define kinematic modes as shown on Table 3.5: were used to remove outliers. Thereafter the 490 trips found were categorized into three speed phases (low/medium/high) based on a speed threshold of (40/80) {Nagaraj, 2021 #411}. The AA and its suburbs route showed the majority of the distances travel at vehicle speed 1-40km/h along 740.68 km (53.3%) and travel in 101994 s with 69.94 % to the whole trips. The lowest distances travel at medium speed category 41-80 km/h with only 249.86 km (17.97 %) to whole distances travel and take 26227 s in the duration of travel (17.99 %).

Table 3.5: Criteria set to define kinematic mode trip cycles and micro trips.

| Kinematic mode | Speed (V) | Acceleration (a) | Duration (T) | Distance (D) |
|---|---|---|---|---|
| Stop mode | V < 1m/s | >-0.15m/s$^2$ & < 0.15 m/s$^2$ | $T_{idle}$ | 0 |
| Acceleration | V >1m/s | > 0.15 m/s$^2$ & < 4.5 m/s$^2$ | $T_{cruz}$ | Dcruz |
| Cruising | V >1m/s | >-0.15 m/s$^2$ & < 0.15 m/s$^2$ | $T_{accel}$ | Daccel |
| Deceleration | V >1m/s | < -0.15 m/s$^2$ & > -4.5 m/s$^2$ | $T_{decel}$ | Ddecel |

The high speed 81-120km/h trips with medium distances of travel 399.93 km (28.75 %) and contributed the least about 17485 s, which is 12.01% of the whole travel time. Similarly, filtered and smooth data were classified into micro trip (MT) and stop bins based on criteria set to remove unrealistic values, and there were 4463 MT and 3236 stop data bins. Statistical models were built to obtain an idea of how the different parameters of trip cycles and MTs behave and what their distribution is.

### 3.5.5 Random selection-to-RSBS method

A new approach was devised to utilize the suitability of random selection for heterogeneous traffic conditions such as AASU routes, and to characterise the driving behaviour split based up on acceleration-related features, focusing on the assessment of their influence on demand power intensity and energy consumption.

Table 3.6: Characteristic distribution for short trips and stops of the three-speed phases.

| Profile Characteristics | Low | Medium | High |
|---|---|---|---|
| Traffic speed limit (km/h) | 30-40 | 40-80 | 80-120 |
| Real data proportion (%) | 70 | 18 | 12 |
| Phase duration (s) | 924 | 238 | 159 |
| Average short trip duration (s) | 64 | 251 | 131 |
| Average stop duration (s) | 11 | 5 | 5 |
| Short trips | 10 | 1 | 1 |
| Stops | 11 | 2 | 2 |

The length of the total duration of candidate cycle for AASU routes was set based on the statistical results of trip cycles, whereas phase durations for each of the three speeds were calculated proportionate to the collected data. The results are presented on Table 3.6.

Equations (3.5) and (3.6) used in the synthesis of WLTC were adapted to determine the optimum number of short trips (ST) for each speed phase. Thus, ten (10) STs were obtained with a corresponding eleven (11) stops for the low speed phase, and single but relatively longer trips for the medium and high-speed phases. A separate statistical analysis was performed to assign the first ST and chaining sequence of each. Then, driving behaviour was split based on the position of the average score on a quartile graph obtained from cumulative diagram functions (CDF) of acceleration-related features (T. Yuan et al., 2022). The combination of STs was made from each mild and aggressive acceleration and braking behaviours.

$$N_{ST} = (T_{SP} - T_{AS})/(T_{AST} - T_{AS}) \tag{3.5}$$

$$N_S = N_{ST} + 1 \tag{3.6}$$

where number of ST ($N_{ST}$) and $N_S$ are the numbers of ST and stops, and $T_{SP}$, $T_{AST}$ and $T_{AS}$ are the durations of speed phase, average short trip and average stop respectively. After combining STs, the candidate cycle with the smallest chi-squared values of RPA and RNA were selected from each behaviour. Finally, the combination cycle consisting of each behaviour in proportion to the percentile score distribution was synthesized as a candidate cycle for the AASU driving profile.

### 3.5.6 K-means clustering method

Here, the k-means clustering approach was implemented to group the samples with data similarity without a given classification category. Initially, the features were scaled to the same range before applying a dimensionality reduction by principal component analysis (PCA). Dimensionality reduction was performed by employing PCA to avoid crowding and visualize the results more effectively. Then, eigenvectors and eigenvalues of the exposed covariance matrix were calculated, which helped to select the most essential initial features based on the variability being prioritised. The quality and representativeness assessed through the variance were explained using a Pareto graph.

Finally, MTs were grouped by k-means clustering, which calculated the distance between data points to find the closest ones based on their driving features. Prior to clustering, the silhouette coefficient employed and cluster quality were evaluated to find the ideal number of clusters that best fits the data set. A representative number of MTs were selected from each cluster based on their closeness to the cluster centres until a cycle duration of 1320 s cycle was achieved. The duration distribution for each cluster was calculated in proportion to the data count as follows (Chandrashekar et al., 2021):

$$T_{MTC(i)} = \left( \frac{T_{C(i)}}{T_{DC}} \right) T_{MT} \tag{3.7}$$

where $T_{MTC(i)}$ is the duration of MT from the $i^{th}$ cluster, $T_{C(i)}$ is the duration of the $i^{th}$ cluster, $T_{MT}$ is the total duration of MTs clustered, and total duration of the candidate drive cycle ($T_{DC}$) is the total duration of the candidate DC.

## 3.6 Modelling and Sizing of the BEV Powertrain

Detailed analysis of vehicle dynamics is starting point in sizing of BEV powertrain. The energy flow within vehicle and the interaction between vehicle and longitudinal road loads were characterized based on physical models to analyse the energy consumption. The main energy flows in proposed model was considered from the battery pack to the wheels for propulsion of the vehicle, from the wheels to the battery pack during regenerative braking. Forward facing method was implemented to fully capture the dynamic effects of powertrain sub-components and driving condition modulated by driver model.

### 3.6.1 Characterization of Vehicle Longitudinal Dynamics

The road vehicles are subjected to forces that the propulsion system has to overcome in order to propel vehicle. The tractive effort ($F_T$) which needs to overcome these forces by transmitting power via the vehicle drive wheels and tires to the ground. The modelling of the propulsion system performance was embedded within a function ($\phi_{PSP}$) of Equation (3.8), which was responsible for computing the propulsive power ($F_T V_{i,X}$) and the rate of change of vehicle energy content (dE/dt) (Decker, Förster, Gauterin, & Doppelbauer, 2021; Martyushev et al., 2023).

$$\left[(F_T V_{i,X}), dE/dt\right] = \phi_{Pf}\left[P_D, F_T, V_{i,X}, i_{tf}, \eta_{tf}, \eta_M, P_M, T_M\right] \tag{3.8}$$

where, $V_{i,X}$ is velocity, $P_D$ is the power demand to overcome total road load, $P_M$ and $T_M$ are motor power and torque, $\eta_M$ is efficiency of motor, $i_{tf}$ and $\eta_{tf}$ are combined transmission gear ratio and efficiency respectively. The total power demand of a vehicle to overcome the road loads for complete trip is expressed in Equation (3.9) and the excess power can be used to meet the acceleration or gradability requirement based on change of state variables.

$$P_D = P_{DR} + P_{RR} + P_{GR} + P_{aR} + P_{IR} \tag{3.9}$$

where: $P_{DR}$, $P_{RR}$, $P_{GR}$, $P_{aR}$ and power demand to overcome translational inertia ($P_{IR}$) are power demand to overcome aerodynamic drag, tire rolling resistance, road slope, translational inertia of the vehicle, and rotational inertia of the wheels and transmission elements during acceleration respectively. The power intensity influenced by instantaneous state variables of driving profile such as velocity, acceleration and road slope and can be resolved as presented in Equations (3.8-3.20):

The instantaneous power demanded to overcome aerodynamic drag resistance ($P_{D,i}$) to the forward motion of a ground vehicle can be calculated by using the drag equation (W. Gao et al., 2021) as:

$$P_{D,i} = 1/2\,\rho_a C_D A_f (V_{i,X})^3 \tag{3.10}$$

$$P_{D,i} = \beta_a V_{i,X}^3 \tag{3.11}$$

where: $\rho_a$ is the density of air in (kg/m$^3$), $C_D$ is the overall drag coefficient for the vehicle, $A_f$ is the projected frontal area (m$^2$) of the vehicle, and $\beta a$ is the coefficient of drag power intensity.

The rolling resistance equation can be used to estimate the power overcoming resistance due to hysteresis of the tire at the contact patch with the roadway as:

$$P_{R,i} = \mathrm{M}_G \mathrm{g} C_o V_{i,X} + \mathrm{M}_G \mathrm{g} \mathrm{C}_1 V_{i,X}^3 \tag{3.12}$$

$$P_{R,i} = \beta_S V_{i,X} + \beta_D V_{i,X}^3 \tag{3.13}$$

where: $M_G$ is the gross mass of the vehicle (Kg), $g$ is the acceleration due to gravity (9.81m/s$^2$), $C_O$ and $C_1$ are static and dynamic coefficients of rolling resistance of the vehicle's tires, $\beta_S$ and $\beta_D$ are coefficients of rolling resistance power intensity respectively.

The power intensity required for overcoming the translational inertia ($P_{a,i}$) of the vehicle at a time instant ($i$) can be determined using Newton's second law of motion:

$$P_{a,i} = a_{i,X} V_{i,X} \tag{3.14}$$

where $a_{i,X}$ is the translational acceleration of the vehicle along the longitudinal direction of motion.

The finite difference of time instant ($i$) was utilized to calculate the overcoming PI,$_{i}$), where the change in rotational kinetic energy within a short timespan ($\pm \Delta t$) divided by the timespan duration:

$$P_{\mathrm{I,i}} = \left(\frac{1}{2\Delta t}\right)\frac{I}{2}\left(\omega_{i+1}^2 - \omega_{i-1}^2\right) \tag{3.15}$$

where: $I$ is the total equivalent rotational inertia (kg.m$^2$) for all the wheels and rotating transmission elements of the vehicle and is the rotational speed of the wheels (rad/s). Factoring the squared difference and multiplying the numerator and denominator by the square of the effective radius of the wheels ($r_w$) and then rearranging terms as $\Delta t$ tends to zero Equation (8) can be simplified (Hamza & Laberteaux, 2018) as:

$$P_{I,i} = \left( I / r_w^2 \right) a_{i,X} V_{i,X} \tag{3.16}$$

The term in the parenthesis can be substituted by the equivalent mass of the rotating components ($M_r$), and the ratio of ($M_r/M_G$) is the proportion of inertia mass factor ($\beta_I$), which depends on operating gear.

$$P_{I,i} = \beta_I a_{i,X} V_{i,X} \tag{3.17}$$

Combined inertia power intensity ($P_{A,i}$), which is the sum of demanded powers overcoming the translational and rotational inertias at a time instant ( $i$ ) can be expressed as:

$$P_{A,i} = \left[1 + \beta_I\right] a_{i,X} V_{i,X} \tag{3.18}$$

The component of power ($P_{G,i}$) due to the gross weight of a vehicle along the road slope and overcoming its uphill motion can be determined using elementary mechanics as:

$$P_{\mathrm{G,i}} = \mathrm{g} V_{i,X} \sin\left(\arctan(s)\right) \tag{3.19}$$

Where: $s$ is the slope of the road (%), with a positive value indicating an uphill climb.

The total instantaneous power intensity ($P_i$) in a vehicle, which was attributed for overcoming all resistance forces at a time instant within a mission trip can be expressed as:

$$P_i = \left[1 + \beta_I\right] a_{i,X} V_{i,X} + \left[\beta_S + g \sin(\arctan(s))\right] V_{i,X} + \left[\beta_D + \beta_a\right] V_{i,X}^3 \tag{3.20}$$

Maximum availability in terms of energy and power during braking can be obtained from changes in kinetic energy and rate of initial kinetic energy as expressed in Equations (3.21) and (3.22) respectively.

$$E_{r,\max} = M_G / 2\left(V_{(i,X)o}^2 - V_{(i,X)f}^2\right) \tag{3.21}$$

$$P_{r,\max} = M_G / 2\left(V_{(i,X)o}^2 / t_{D,\min}\right) \tag{3.22}$$

where, $V_{(i,X)o}$ and $V_{(i,X)f}$ are the initial and final velocities of the vehicle in braking instance respectively. $t_{D,min}$ is the minimum time of deceleration to stop the vehicle as a possible shortest stopping distance. Full recapturing has not achieved yet due to loss of energy during conversion as well as the very short deceleration time required to stop the vehicle. The efficiency of regeneration was determined from simulation, which in turn influences the size of the on-board ESS.

### 3.6.2 Modelling Powertrain Components and The Simulation Setup

In this section the simulation setup that is flexible for different type vehicle category and capable to handle different architectures was modelled in Simulink window. MATLAB code was written to initialize the simulation, input vehicle characteristics, and allocate power split and energy management strategy. Here it was decided to use combined approach using backwards models for coarse-tuning at vehicle and system levels and forwards models for fine-tuning transient effects of individual component. A backward-facing technique was utilised to anticipate the energy consumption of a typical driving profile, which was then used to compute the power required to track that specific drive profile. Forward modeling is the most realistic approach, where the inputs are forces and torques and the outputs are the resulting motions. In this approach also typical drive profile taken as input, but driver model (PID) is incorporated to exactly trace the profile and minimize errors so as to adjust the trajectory to reference or set point cycle (Huang et al., 2018). Figure 3.9: depicts the whole simulation setup of forward facing, which allows for flexibility in component design due to access to internal system variables.

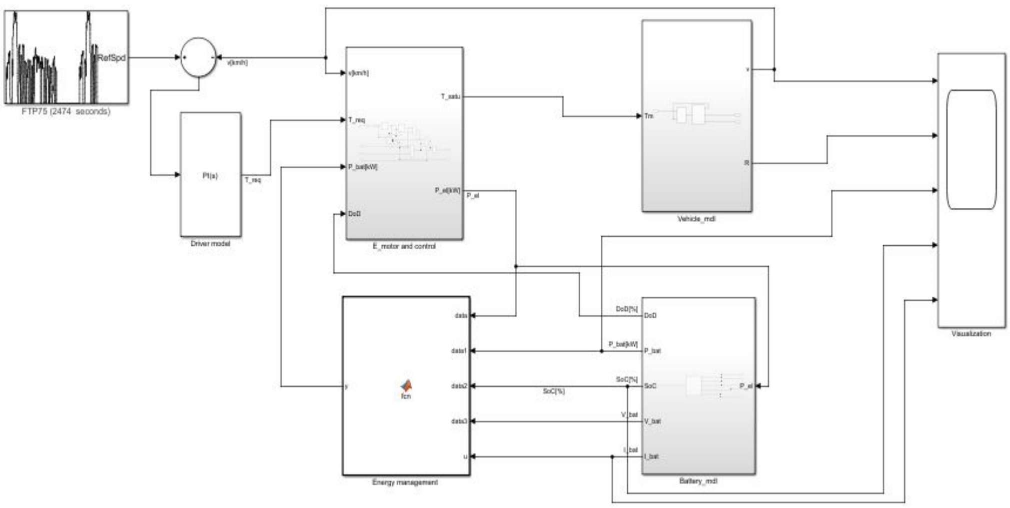


Figure 3.9: MATLAB/Simulink simulation setup for sizing the BEV powertrain

Code was written in MATLAB function as m-file to be utilized as power split Simulink block for overall simulation as shown on Figure 3.10 and 3.11. Besides user defined MATLAB function blocks were built in editor window based up on hi-level parameters of each component. Overall simulation set up in MATLAB editor window consists of run block to initialize each function blocks such as vehicle, motor, battery, and power split blocks. Besides predefined Simulink blocks and simulation set up was used to visualize and analyze the expected output. Longitudinal Kinematic of concept car was modelled based up on energy and power conservation and magic formula was used to model tire dynamics.

```
EV_Simmodel_run.m | Motor_Effcncy.m | road_load0723.m | dc_plot_new.m | cdf_plot.m | plotacc.m

clc
clear
close all

m_gv=2000; % mass in Kg,
Cd=0.3; % drag coefficient
A_f= 2.15; % frontal area m2
w_tr =215;% tire width mm
S_as=50; % aspect ratio %
D_rm=18; %rim diameter inch
p_tr=2.60; %tire inflation pressure bar
alpha = atan(0/100);      % vehicle slope
g = 9.81;        % [m/s^2] gravity acceleration
rho = 1.18; % [kg/m^3] air density of Addis Ababa in october 2021
Jw = 0.6; % [kg*m^2] wheel inertia
Jm = 0.06; % [kg*m^2] motor inertia
mu_x = 0.85; % [-] coefficient of friction during traction
mu_b = 0.8; % [-] coefficient of friction during regenerative braking
%% drived relations
R = ((25.4*0.5*D_rm)+ (s_as/100*w_tr))./1000; % [m] tire rolling radious
b.v_max = 130/3.6; % [m/s] vehicle maximum speed
c_o = 0.005 + 0.01*(1/p_tr); % [-] static rolling resistance coeff.
c_1 = (0.0095/p_tr)*(b.v_max/100)^2; % [1/m^2] dynamic rolling resistance coeff.
A = m_gv*g*(c_o*cos(alpha)+sin(alpha)); % road load static contribution
B = m_gv*g*c_1*cos(alpha)+0.5*rho*Cd*A_fv; % % road load dynamic contribution
Re = 0.98*R; % [m] effective rolling radious
```

Figure 3.10: Sample of script in editor window used for MATLAB function blocks

```
Editor - EV_Simmodel_run.m | Project - EV
EV_Simmodel_run.m | Motor_Effcncy.m | road_load0723.m | rlload_lrang.m | dc_plot_new.m


clc
clear
close all
% Tractive effort
fprintf('please enter F_FWD\n');
F_FWD = input('Enter the value: ');
fprintf('please enter F_RWD\n');
F_RWD = input('Enter the value: ');
fprintf('please enter F_AWD\n');
F_AWD = input('Enter the value: ');
if F_FWD < F_RWD && F_FWD < F_AWD
    F_t2 = b.mu_x * F_FWD;
    Fz = F_FWD;
elseif F_RWD < F_FWD && F_RWD < F_AWD
    F_t2 = b.mu_x *F_FWD;%
    Fz = F_RWD;
else
    F_t2 = b.mu_x *F_AWD;
    Fz = F_AWD;
end
F_tmax = min(Ft_1,F_t2);
fprintf ('Tmax = %d\n',F_tmax);

T_requet=b.i_n*b.thou_t*b.Re*F_tmax; % motive torque of moto
b.Fb_max=b.mu_b*m_gv*g;
```

Figure 3.11: M-file in editor window used for MATLAB function block of vehicle

FWD, RWD and 4WD with single traction motor topologies are analyzed to access traction limit due to static weight distribution and dynamic load shift in front and rear axles. Two

speed planetary gear ratios are incorporated to analyze toque and speed improvement capability at low and high speeds respectively. All possible and feasible topologies are generated using energy flow matrix among all energy and power sources. Power and energy management strategy was allocated by classifying vehicle operation modes and characteristics of each source and power electronics.
The vehicle block input is the torque value coming from the motor block, the outputs are the actual vehicle speed and the distance travelled. The inside structure shown on Figure 3.12: where the first section is dedicated to the wheel representation, the second one collects the dynamic equations that rules the motion, a third block is employed to evaluate the travelled distance.

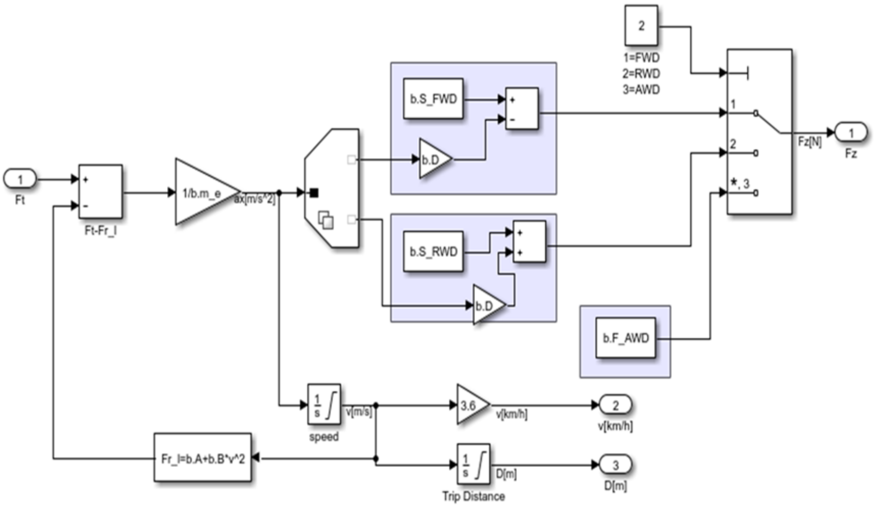


Figure 3.12: Vehicle dynamic model in Simulink to visualize traction tractive effort

The dynamic equation that rules the vehicle motion and weight distribution on the traction wheels. It receives as input the traction force that will subtract for the resistant forces that are computed in the dedicated block. While the vehicle speed is the output of the whole vehicle block, the vertical force will be exploited to the traction force evaluation of the previous wheel model block

### 3.6.3 Weight and Power Constraint Analysis

Primarily, dimensional constraints that could be imposed on BEV concepts because of legislation, ergonomic issues, and drag force were analysed. In addition, the specific power constraint based on the ratio of the overall mean power ($P_A$)-to the gross weight of the vehicle was analysed. The specific power of the new design must be equal to or greater than that of the baseline vehicle limit for successful design as shown in Equation (3.23).

Regardless of the propulsion system architecture, the overall power-to-weight ratio of the new design must be equal to or greater than that of the baseline vehicle,

$$\left(P_A / W_{VG}\right)_{Concept(i)} \geq \left(P_A / W_{VG}\right)_{Benchmark} \tag{3.23}$$

Where, $P_{ava,ova}$= Overall available power, $P_{ava,i}$= available power in individual power source

The candidate design must have uniform distributed design static and dynamic loading at front and rear axles based up on pre-fixed axle ratio so as gross weight of the vehicle distributed in wheelbase-track area and supported by four wheels at each corner. That was to satisfy chassis structural strength as well as vehicle dynamic operational requirements.

$$\left(W_{VG} / A_{fpt}\right)_{Concept(i)} \geq \left(W_{VG} / A_{fpt}\right)_{Benchmark} \tag{3.24}$$

On the other hand over all dimension of the vehicle is constrained by legislation and ergonomic issue while effective frontal area is constrained by drag force.

$$\left(V_{Intrr} / A_{frnt}\right)_{Concept(i)} = \left(V_{Intrr} / A_{frnt}\right)_{Benchmark} \tag{3.25}$$

Where, $A_{fpt}$ is area covered by footprint, $A_{frnt}$ is frontal area; $V_{Intrr}$ is interior volume of the vehicle

The vehicle sizing is an iterative process in which each iteration includes the recalculation of vehicle geometry, component weights, and the required energy of each energy source for the design and reserve missions.

### 3.6.4 Energy Constraint Analysis

The main goal of the energy based constraint analysis is to obtain a proper relation between scaling parameters such as propulsive effort required to overcome road loads at various operating conditions and surplus power to take over even at high speeds and adequate suspension support of dynamic and static weight. This can be related by normalized wheel load ($F_{rl}/W_{VG}$) at different speeds and road grades as well as exterior vehicle dimensions, occupant interior volume and effective frontal area. The scaling parameters are independent of the size of the vehicle and thus, this analysis is applicable to vehicle of all sizes.

The energy constraint analysis was based on the energy balance with in-vehicle and the interaction with longitudinal road loads. The total instantaneous power intensity Equation (3.20) was modified as shown in Equation (3.26) to determine the rate change of its total kinetic and gravitational potential energies from the rates of energy supplied or removed from the propulsion source, tire road traction, and aerodynamic drag.

$$(F_T V_{i,X}) - (P_{DR} + P_{RR}) = \frac{d}{dt}\left( W_G \sin(\arctan(s)) + \frac{1}{2}\left(\frac{W_G}{g}\right) V_{i,X}^2 \right) \tag{3.26}$$

The difference between $(F_{Tra}V)$ and total resistive power of (DV) and $(F_{RR}V)$ is called the excess power (Ps), and can be modulated through the vehicle's control effectors to change the energy state of the vehicle, through a change of kinetic and/or gravitational potential energy. Depending on the driving cycle phase and the intended manner in which it is to be flown, the excess power can be suitably apportioned to kinetic and potential energy rates, thus allowing computation of vehicle acceleration (dV/dt) and rate of grad ability (dh/dt). The numerical integration of these time derivatives along with time derivatives of vehicle energy consumption rate form the core of the mission performance analysis method.

In order to visualize the design space, a diagram which incorporates the effects of the constraints on the road load wheel forces (aerodynamic drag and rolling resistance) for each of the concept BEVs have been estimated at speed levels within their specified speed ranges dimensional parameters can be plotted as shown in previous section. Due to the aerodynamic drag, the wheel force shows a strong dependence on speed. The high performance car demands the largest wheel force at a certain speed level compared to the other cars, and the city car demands the lowest. The contour lines represent wheel power for a certain combination of speed and force.

The difference between tractive power and total resistive power ($P_{DR}$+$P_{RR}$) in Equation (3.26) is the excess power that could be utilized to provide either grade ability or acceleration performance depending on the vehicle state and intended control of the vehicle. The propulsive effort and the power demanded by urban and long-range cars were obtained by normalizing wheel load at different speeds and road slope as shown in Figures 3.13.

The peak power demands of the urban and long-range concepts to negotiate 6% grade at high speed (90km/h) were 27.5 kW and 70 kW respectively as shown in purple contour highlighted with red points in Figures 1 and 2. However, the initial or starting force was found to be significantly higher with 3kN for urban and 5kN for long range at 25% grade. For the stated demanded levels of force and power based on the requirements of top speed, high-speed grade ability, and high-slope take off, it could be noted that the implied acceleration capacity of each car would be rather limited.

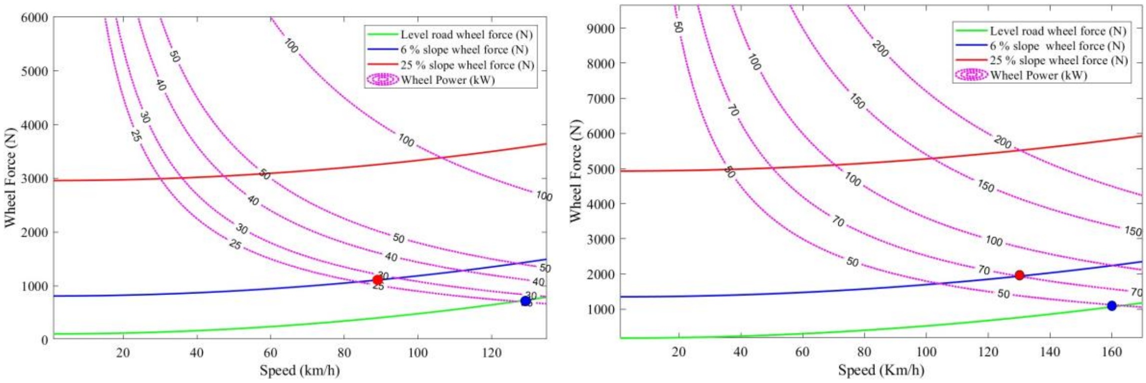


(a) Urban car (b) Long range car

Figure 3.13: Road load and power demand of the urban (a) and long-range (b) car

To set the acceleration requirement in design template, three combinations of initial maximum levels of wheel force and wheel power limits were identified at the base-to-top speed ratios of 1/4, 1/3, and 1/2 and analysed for each BEV. The torque and speed characteristics of typical electric machine was assumed to fulfil the acceleration requirement of the three conditions.

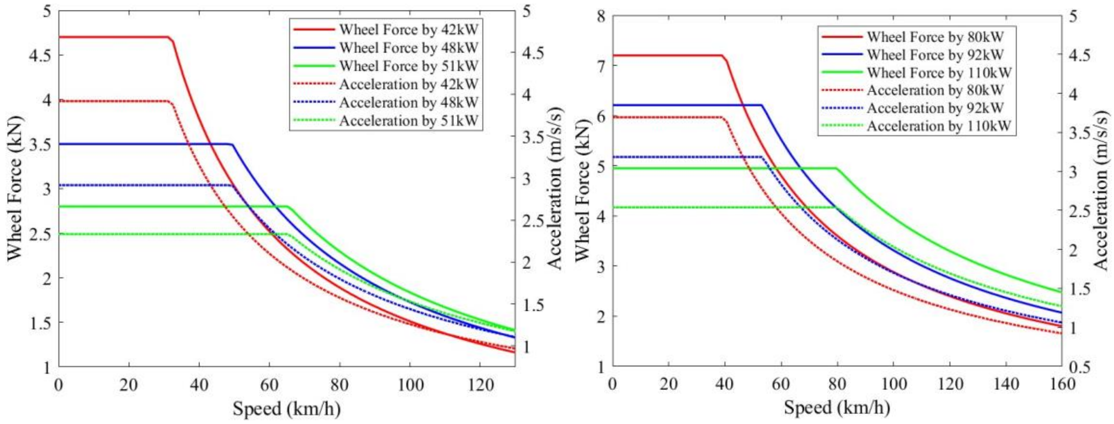


(a) Urban car (b) Long range car

Figure 3.14: The acceleration requirement and normalized wheel force

In illustrative Figure 3.14 normalized wheel forces are presented in blue colour for 42kW, 48kW and 51kW power levels respectively and the corresponding accelerations are presented in red colour. The maximum acceleration of 3.9 m/s$^2$ was obtained for urban car at the lowest base speed and lowest power (42kW) highlighted in red solid line on Figure 3.14 (a). The largest power (51kW) was observed to provide the minimum acceleration capacity of 2.4m/s$^2$ at a half-speed ratio. The maximum acceleration levels of the long-range car were observed to be lower than urban car.

In specifying the acceleration performance, the minimum time to accelerate is the dominant indicator than the maximum acceleration attained. Acceleration time differs widely for each BEVs, since it is influenced by the characteristics of power source and traction limit. To address the effect of power source, full power acceleration was analysed at wide speed operating range for the two BEVs.

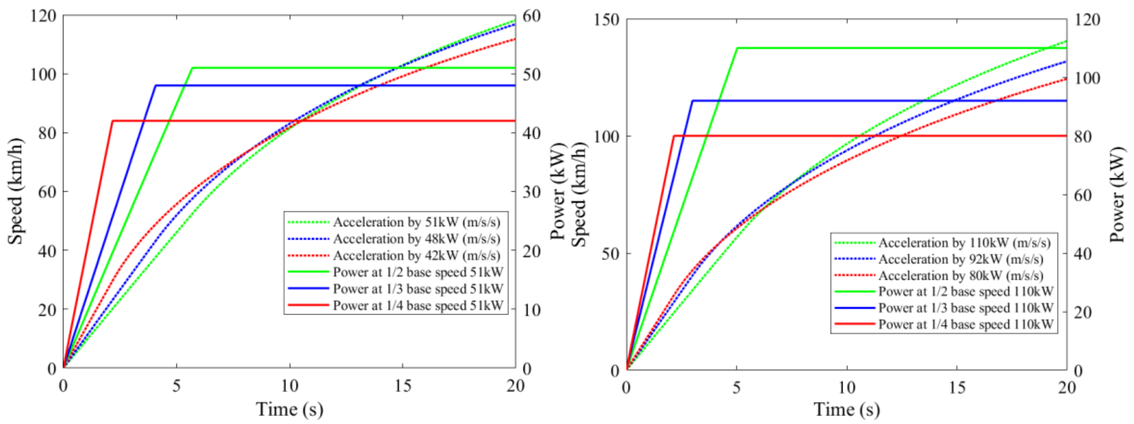


(b) Urban car (b) Long range car

Figure 3.15: Full power acceleration of urban car (a) and long-range car (b)

The acceleration requirement of 0-100km/h was achieved around 15 s by the three power and force levels of the urban and long range cars as shown in Figure 3.15. However, the acceleration levels at low and high speeds were observed to be different. The lowest base speed related to the largest initial force (4.7 kN), and lowest power (42kW) was found to provide the fastest acceleration of 0-50 km/h (just approximately 4 s), while the acceleration time of 50-100 km/h was the longest (around 11 s).

The full power acceleration performance of urban car was found to be best fit at lower speeds than the high speed. Besides, the top-level requirement of this car was set based on the city driving conditions, the low-speed acceleration performance should be preferred over the high-speed and the lowest power level should be the design template. The acceleration time (0-100km/h) of long-range car was lower than the urban car for all power levels. The minimum time attained was 10.5 and 11 seconds by the largest and middle powers respectively. However, the middle power (92 kW) attained the best low-speed performance (3.8 s when accelerating 0-50 km/h) as compared to that of 5 s largest power. Therefore, the long-range car should be designed to perform well at higher speed levels, and thus the base-to-top speed ratio of 1/3 is chosen.

The simulation results showed that the demanded power intensity for acceleration (42kW) is the highest when compared with power intensities to overcome high speed (24kW), 6% grade at speed (27.5kW) and 25% grade take off (22kW) resistances for urban car. Therefore, it could be concluded that the acceleration requirement demands the largest instantaneous force and power from the drive system. However, the requirement on acceleration time from 0-100 km/h alone is not enough when seeking to specify a vehicle's acceleration performance over the operational speed range. Since the acceleration time from 0-50 km/h, hence also 50 -100 km/h differs for all combinations and should be analysed independently

### 3.6.5 Energy and Power Analysis for Typical Drive Cycles

The cumulative energy consumption rate by urban and long range cars to negotiate the road load were calculated for the synthesized AA and its suburbs DC, WLTC2 and UDDS driving cycles. Speed acceleration distribution of ASU DC is shown in Figure 3.16 and characteristic distribution of the most essential driving features are presented in Table 3.7.

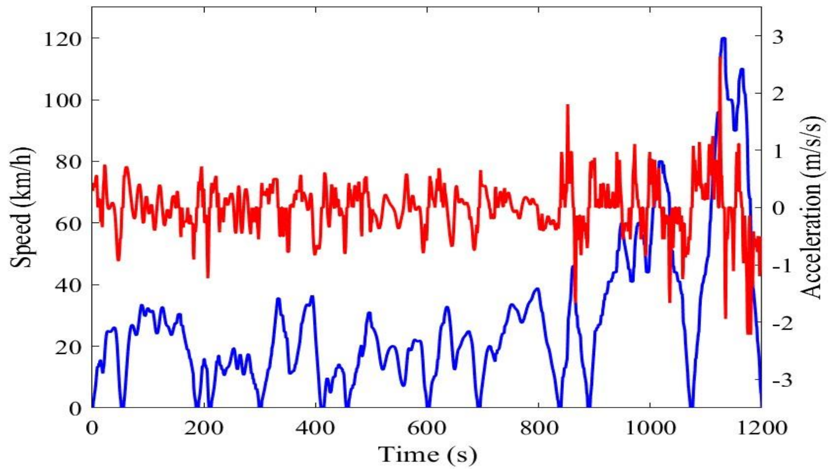


Figure 3.16: Speed profile and acceleration distribution of synthesized drive cycle

In Figure 3.17, the area under the curve of the UDDS cycle peaked higher at 0.65 kWh at a greater speed compared with the AASU’s 0.57kWh for urban car. Less energy was consumed by AASU DC than by the WLTC-2 and UDDS cycles at a wide operating range, except at peak velocity.

Table 3.7: Representative parameters of the synthesized driving cycle

| Drive cycle Parameters | Drive cycle phases | | |
|---|---|---|---|
| | Low | Medium | High |
| Total Duration(s) | 840 | 216 | 144 |
| Average Speed (km/h) | 19.0 | 49.7 | 74.0 |
| Maximum Speed (km/h) | 38.85 | 80 | 120 |
| Average Acceleration (m/s$^2$) | 0.22 | 0.62 | 0.367 |
| Average Deceleration (m/s$^2$) | -0.25 | -0.71 | -0.39 |
| Distance (Km) | 4.196 | 2.942 | 2.835 |
| Relative Positive Acceleration (m/s$^2$) | 0.185 | 0.5 | 0.29 |
| Relative Negative Acceleration (m/s$^2$) | -0.22 | -0.66 | -0.32 |

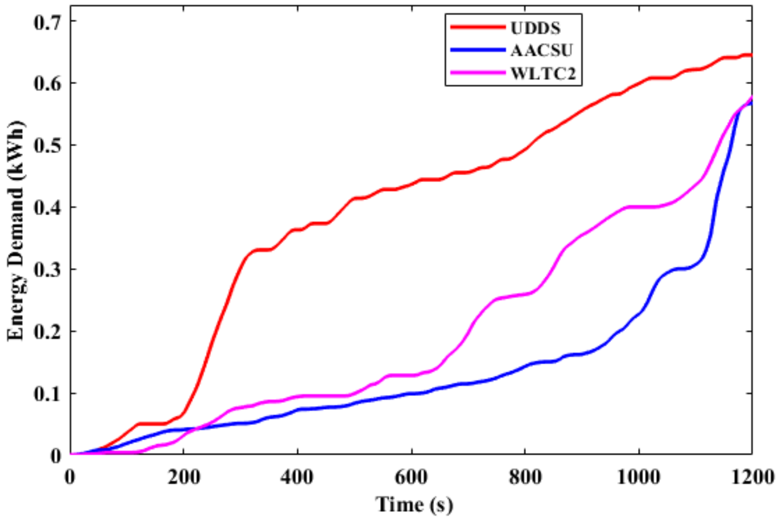


Figure 3.17: Energy demand rate of urban cars for all simulated drive cycles

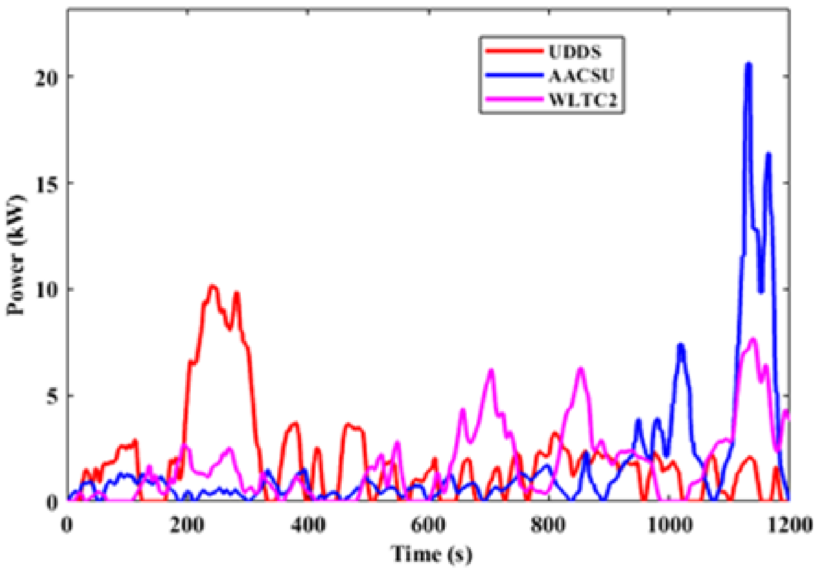


Figure 3.18: The power demand of urban car for simulated drive cycles

For the high-speed expressway part of the AASU DC, a distinct operating point could be found at 120 km/h, where the urban car demanded more power (20kW) as shown in Figure 3.18. However, the proportion of the route segment with high speed was only 10 % and the cumulative demand of cycle was lower. A summary of power and energy demands to negotiate different road loads are presented in Table 3.9.

Table 3.8: Summary of energy and power requirements of concept cars for tested cycles

| Parameters | Urban car | Long-range |
|---|---|---|
| AASU energy (Wh/km) | 70 | 92 |
| WLTC2 energy (Wh/km) | 74 | 97 |
| UDDS energy (Wh/km) | 82 | 107.4 |
| Change in potential for 6% (Wh/km) | 18 | 40 |
| Change in potential for 25 % (Wh/km) | 22 | 45 |
| Range requirement (km) | 160 | 250 |
| Design power demand (kW) | 44 | 92 |
| Design battery demand (kWh) | 18.92 | 46.7 |

### 3.6.6 Implemented battery model

The battery cell used was a Lithium-ion cell of laminate type, which was used in Nissan Leaf BEV models (Kaleg, Hapid, & Kurnia, 2015). The estimation of battery capacity was based on an equivalent circuit model, where open circuit cell voltage ($V_{oc}$) has been estimated by approximating the resistive voltage drop during a C/3 discharge rate, as shown in Figure 3.19 and 3.20. The average open circuit cell voltage within the used SOC window (10 to 90%) has been estimated to 3.89 V.

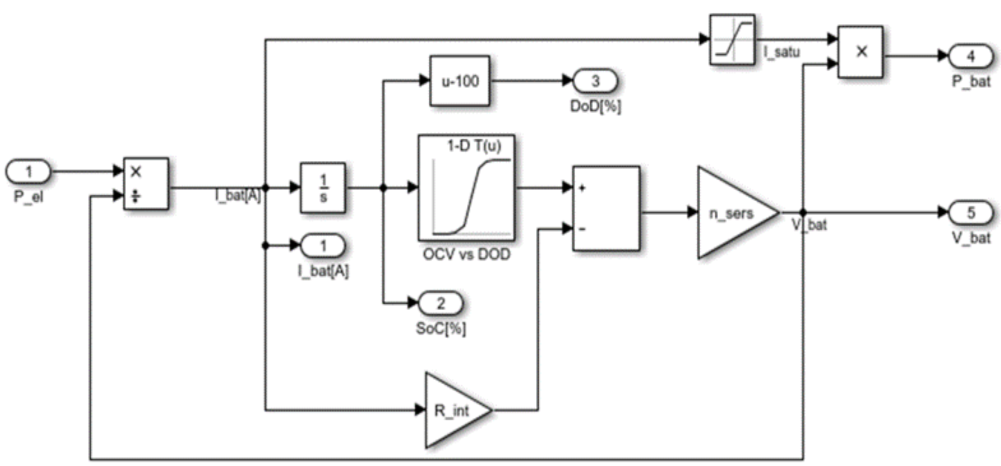


Figure 3.19: Simulink model of Battery model

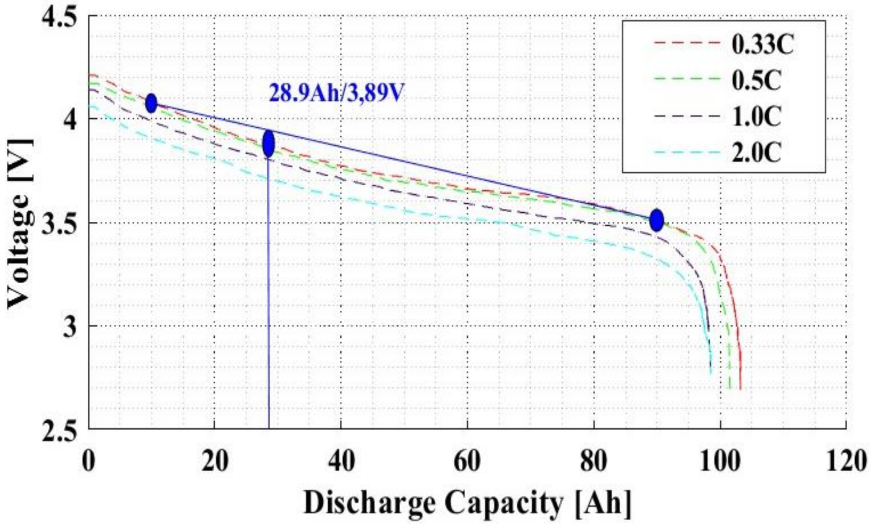


Figure 3.20: Lithium-ion battery cell discharge capacity and voltage in (10-90)% SOC

To determine the battery energy content of each car desired WLTC driving range and early calculated wheel energy consumption from Table 4 were utilized. The average number of series cells was 97.799 for both cars. The number of cells in parallel was found by the current criterion. A summary of battery data along with calculated parameters shown in Table 3.9.

Table 3.9: Summary of Battery cell data

| Parameters | Urban car | Long range |
|---|---|---|
| Capacity (ah) | 28.90 | 28.90 |
| Maximum voltage (V) | 4.2 | 4.2 |
| Nominal voltage (V) | 3.78 | 3.78 |
| Minimum voltage (V) | 2.5 | 2.5 |
| Voltage @90%SOC (V) | 4.09 | 4.09 |
| Voltage @10%SOC (V) | 3.62 | 3.62 |
| Number of parallel cells | 1.81(2) | 2.76 (3) |
| Number of series cells | 97.799 | 97.799 |
| Discharge resistance (mΩ) | 160.4 | 103.4 |
| Charge Resistance (mΩ) | 134 | 86.4 |
| WLTC Range (Km) | 160 | 250 |
| Total voltage @90% SOC (V) | 332 | 320 |

### 3.6.7 Implemented electric machine and transmission

In this work, PMSM is preferred as it is intended for passenger-class EVs (Chen et al., 2020). Loss-based motor model was developed instead of assuming a constant efficiency as represented in Equation (3.28). This model is reported to be suitable for all types of motors and approximates variable efficiency for known operating conditions in terms of motor torque and rotational speed (Z. Gao et al., 2019). The dynamic effect of this machine can be best represented by motor power Equation (3.27) and Simulink model on Figure 3.21.

$$P_M = T_M \omega_M + K_C T_M^2 + K_i \omega_M + K_W \omega_M^3 \tag{3.27}$$

$$\eta_M = \frac{T_M \omega_M}{T_M \omega_M + K_C T_M^2 + K_i \omega_M + K_W \omega_M^3} \tag{3.28}$$

where: $K_C$, $K_i$ and $K_w$ are coefficients of power losses due to copper, iron winding respectively and $\omega_M$ is rotational speed of motor.

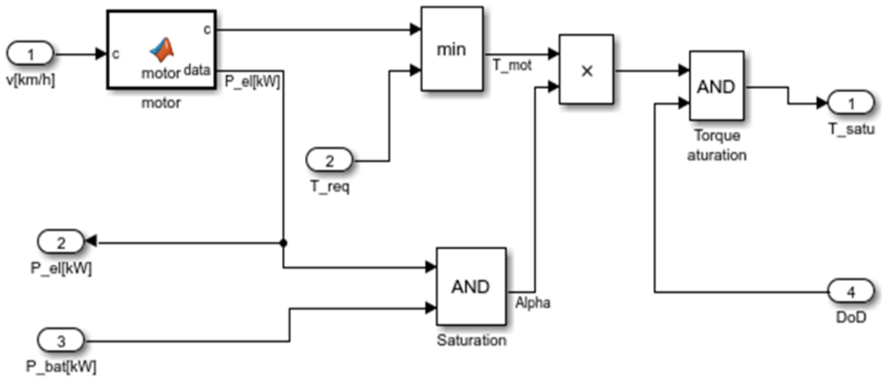


Figure 3.21: MATLAB function block in Simulink for traction machine and controller

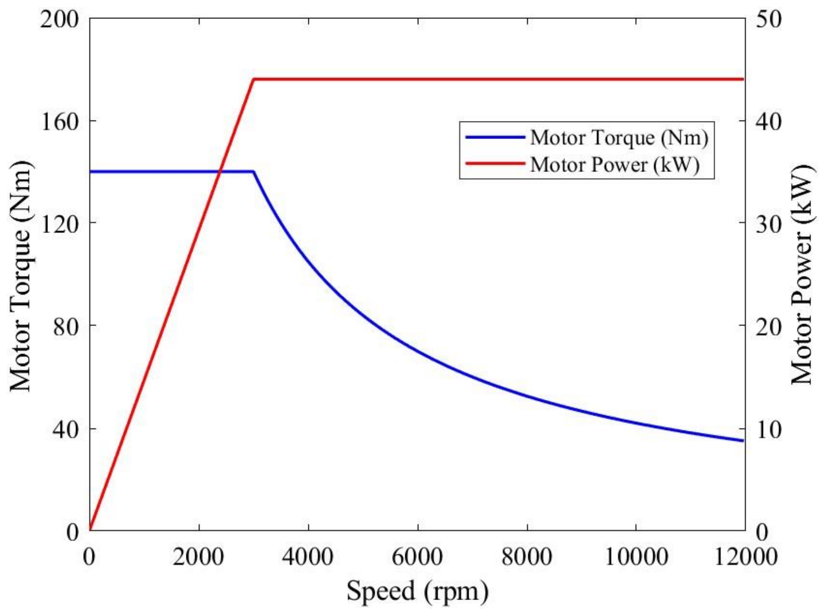


Figure 3.22: The power torque and speed characteristics of motor used for urban car

Table 3.10: Summary of PMSM data for the Urban and long-range BEV motors

| Parameters | Urban Car | Long-range Car |
|---|---|---|
| Peak Power (kW) | 44 | 92 |
| Max Torque (Nm) | 140 | 220 |
| Base speed (rpm) | 3000 | 4000 |
| Max speed (rpm) | 12,000 | 12,000 |
| Gear ratio | 10.5 | 9.7 |
| Max DC voltage (V) | 400 | 400 |
| Max rms phase current (A) | 115 | 225 |
| Peak Efficiency at 400 $V_{dc}$ (%) | 96.4 | 96.8 |

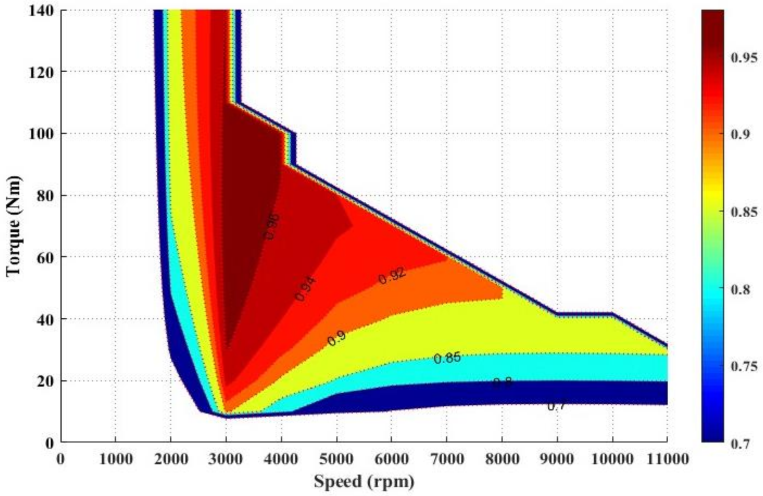


Figure 3.23: Implemented motor efficiency as a function of speed for urban car

The sizing parameters for the traction motor can be explored from torque and power plots in a wide speed range in Figure 3.22 and the efficiency map as shown on Figure 3.23 for urban cars. A 44 kW and 92 kW PMSM motors have been chosen to meet the power requirement during the instances of acceleration and maximum grade take-off during the grading of the road slope. Additionally, the design details along with published machine parameters can be seen in Table 3.10.

The efficient region was found to be at lower torque around (3000rpm) and moderate torque (4000-6000rpm) for urban and long-range cars respectively. The high-speed gear ratio was determined from the motor's maximum rotating speed and the motor's torque capacity to reach this top speed using Equations (20).

$$i_{th} = \omega_M r_w / V_{(i,X)max} i_f \tag{3.29}$$

The maximum vehicle speed ($V_{max}$=130km/h) for urban car and ($V_{max}$ =160km/h) for large cars produces a minimum ratio of 10.5 and 9.7 respectively.

Table 3.11: Implemented electric machine parameters

| Motor Parameters | Urban | Long Range | |
|---|---|---|---|
| | 1-speed | 1-speed | 2-speed |
| Low-speed gear ratio | 10.5 | 9.7 | 9.7 |
| High-speed gear ratio | | | 6.3 |
| Maximum motor speed (rpm) | 12000 | 12000 | 12000 |
| Energy consumption (kWh/100Km) | 10.57 | 17.436 | 17.485 |
| Maximum power (kW) | 44 | 92 | 92 |
| Maximum Torque (Nm) | 140 | 220 | 220/250 |

The low-speed gear ratio was calculated by considering maximum takeoff gradability (25%) using Equation (3.30).

$$i_{tl} = W_G \left( \beta_S cos\theta_{max} + sin\theta_{max} \right) / T_{M,max} i_f \eta_{tf} \tag{3.30}$$

where: $\theta_{max}$ is the maximum slope angle the vehicle can take off and $i_f$ is the final drive gear ratio and At low speeds, the aerodynamic drag is assumed to be zero and the maximum motor torque ($T_{M,max}$ =220Nm) of a range car produces a minimum ratio of 6.3 and was checked against a calculated high-speed ratio of 5.9. Since the calculated value is lower than 6.3, it was taken as a low-speed ratio. The implemented motor parameters along with transmission ratios can be seen in Table 3.11.

## 3.7 Powertrain Packaging and Structural Analysis

In this section, the integration possibility of ESS or battery pack in long range concept vehicle was evaluated, aiming to maximize energy and power density while considering technical and geometrical constraints. The battery pack's type, geometry, and disposition determine the total number of cells and vehicle range. The selection of battery typology and geometry is crucial for capacity and weight efficiency, while the battery pack location ensures vehicle stability and optimizes space.

The rated voltage capacity, energy density, power density, c-rate, SOC, and DOD are some of the operational metrics that are taken into account for evaluation. The driving performance is ensured and battery systems can be compared using these characteristics. Power density is the highest possible power of unit volume, whereas energy density is correlated with the weight or volume of the battery. The high energy produced by power density, and the corresponding discharge rate, or c-rate, is determined by the charging as well as discharging current. The residual energy and discharged capacity are denoted by SOC and DOD.

This study uses laminated lithium-ion pouch cells that are used for Nissan Leaf BEV models, with a maximum voltage of 400V to achieve top speed cursing power requirement for high speed cursing power demand. Parallel cells are observed under transient situations (Yang et al., 2019). Table 3.12: presents a summary of the battery cell data along with the parameters that were determined.

Table 3.12: Summary of Battery cell data

| Parameters | Value |
|---|---|
| Maximum voltage (V) | 4.15 |
| Voltage of nominal (V) | 3.78 |
| Minimum voltage (V) | 2.5 |
| Number of parallel cells | 2.76 (3) |
| Number of series cells | 97.799 |
| Discharge resistance (mΩ) | 103.4 |
| Thickness | 7.2 mm |
| Width | 129 mm |
| Length | 217 mm |
| Weight/cell | 428 grams |
| Specific energy | 174 Wh/Kg |

### 3.7.1 Battery Pack Sizing

The nomenclature of cell order arrangement is shown by a 4S3P battery, which indicates there are 4cells are in series with three in parallel. The total cell count in sub-module (see Figure 3.24 (b)) nine and that of module's pack (see Figure 3.24 (c)) consists of two sub-modules, where its voltage would be 3.78V x 6 = 22.68V; nearly equivalent to 24V battery system of vehicles. The module pack capacity would be 38Ah x 3 = 114Ah, which can deliver constant velocity current of 114A at 1C discharge rate and transient acceleration or grade start ability current of 342A at 3C discharge rate. The maximum battery pack power rating would be 400V× 114Ah = 45.6kWh. Battery pack parameters are presented in Table 3.13.

Table 3.13: Battery pack and module performance parameters

| Criteria | Parameters |
|---|---|
| Power rating | 45.6 kWh |
| Number of total modules | 16 |
| Nominal pack voltage | 400 V |
| Total pack capacity | 114 Ah |
| Total pack weight | 360Kg |
| Total weight controllers | 65Kg |

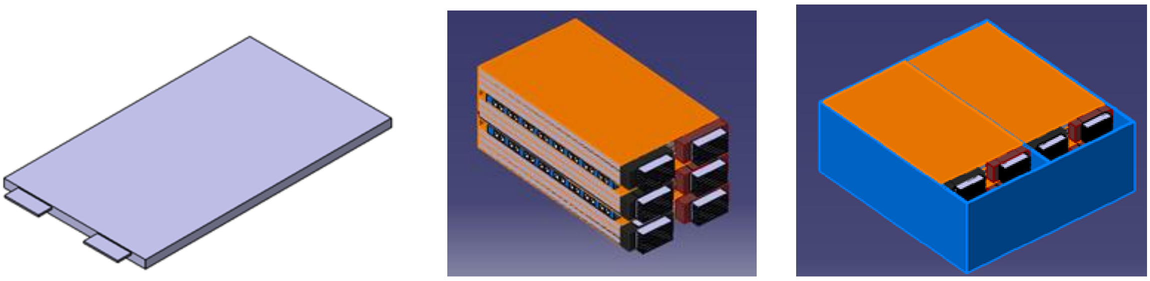

(a) Cell (b) Sub-module (c) Module

Figure 3.24: Battery pack construction cell (a), sub-module (b) and module (c)

### 3.7.2 Weight Estimation

Weight estimation has been done by the sum of the weights of major chassis components which makes up glider weight, powertrain weight and payload, as shown in Equation (3.31).

$$W_{gross} = W_{glider} + W_{powertrain} + W_{payload} \tag{3.31}$$

Table 3.14: Weight distribution for sub-components of concept vehicle

| S. No | Sub-component | Mass (Kg) |
|---|---|---|
| 1 | Body and structure | 570 |
| 2 | Chassis | 285 |
| 3 | Others (10%) of body and structure | 95 |
| | Glider mass | 950 |
| 1 | Motor and transmission | 85 |
| 2 | Controllers | 65 |
| 3 | Battery pack | 360 |
| | Power train mass | 510 |
| 1 | Passengers and driver | (5×75) = 375 |
| 2 | Luggage and spare tire | 115 |
| | Maximum Payload mass | 490 |
| | Gross mass of the vehicle | 1950 |

Futuristic glider weight for BEV is identified as base, lower and higher limits by indicating possible percentage in light weighting. Considering 10% reduction in weight 950Kg for long range concepts were estimated as initial guess of glider weight. The weights of the traction machine and power electronics from (gravimetric power densities, kW/kg) and batteries energy (based on gravimetric density, Wh/kg) were estimated {Singh, 2019 #294;Kavi, 2022

#474;Sayed, 2020 #473}. Overall vehicle sub-component's weight distributions are presented on Table 3.14.

### 3.7.3 Concept Development and Selection

Light weighting has an effect on battery sizes, and hence decreases the battery costs in future years. Battery size in turn affects the major manufacturing cost of battery electric vehicles. It can be seen that higher-range BEVs have a greater impact on manufacturing costs. Battery total energy will decrease significantly owing to other component improvements such as improved weight distribution and ergonomic packaging without major modification on body structure and efficient battery cooling. The battery pack should be easily removed as multiple modules, which are lightweight for one man to carry. A candidate design should have a low centre of gravity, preliminary crash safety features and high voltage protection using appropriate insulation materials. Efficient air-cooling via forced or natural convection so that the entire battery pack to achieve acceptable cell temperatures is essential consideration.

Figure 3.25: A CAD model for packaging concepts of battery pack for functional analysis

Table 3.15: Results of functional analysis for each concept using geometrical model

| **Criteria** | **Front loaded** | **Mid-loaded** | **Rear loaded** | **Clustered** |
|---|---|---|---|---|
| Battery location | Under bonnet | Under seat | Under boot | F:M (25:75) |
| Weight distribution (F:R) | 59:41 | 43:57 | 38:62 | 48:52 |
| CG height position (mm) | 628.5 | 585 | 617.5 | 592 |
| Ground clearance (mm) | 170 | 150 | 170 | 170 |
| H-point limbs (mm) | 350 | 375 | 350 | 350 |
| H-point head (mm) | 250 | 250 | 250 | 250 |
| A60 (degree) | 14 | 14 | 14 | 14 |
| A61(degree) | 5 | 5 | 5 | 5 |

To address afore mentioned requirements with in constrained design space the functions were described in the functional analysis. This analysis generated the need for four different design concepts of powertrain layout; namely clustered, front, mid, rear loaded powertrain layout, as can be seen in Figure 3.25. The functions were described by determining CG points and ergonomic analysis of driver and passenger posture as presented on Table 3.15.

### 3.7.4 Calculation of CG Locations

Longitudinal position of CG included the longitudinal distance of front (lf) and rear (lr) axle from the CG of the vehicle. 'lf' and 'lr' calculated considering all weight items and their corresponding distance from the front axle as reference, using the equation below:

$$l_f = \frac{\sum_1^n m_n l_{fn}}{M} \tag{3.32}$$

Where, $l_f$ is distance of CG from front axle, M vehicle mass, n number of items, $m_n$ mass of component, $l_{fn}$ corresponding distance between components' CG and the centre of front axle. Vertical CG was calculated for maximum tilting angle ($\theta_{max}$) of 32° based on given vehicle geometry.

$$h = R + \left( \frac{W_r l_2 - W_f l_1}{W} \right) \cot \theta \tag{3.33}$$

Where, $W_f, W_r$; are Static weight distributions on front wheels and rear wheels respectively, $W$; vehicle curb weight, R; wheel radius, $\theta_{max}$; inclination angle of front axle from horizontal, $l_1, l_2$; are longitudinal position of COG from front and rear axles respectively.

### 3.7.5 Ergonomic Analysis

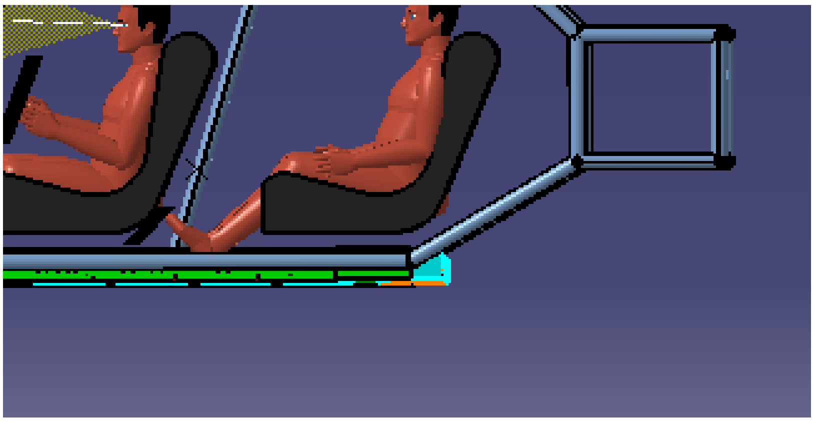

Figure 3.26: Driver and rear passenger manikin ergonomic analysis

In packaging design the position of the driver and passengers is extremely important because it sets the shape and dimensions of the cabin. To create the driver positioning 95$^{th}$ percentile of SAE male manikin was used based on Ethiopian anthropometric data(Bere, Dudescu, Neamtu, & Cocian, 2021). The most essential point set was Seating Reference (SgRP) or Hip Point (H-Point), which set the lower limbs and upper body angles and dimensions. The visibility is set by the angles over and below of the horizontal axis from the eyes of the driver. As it can be seen on Figure 3.26: the visibility of the project is set to 14 degrees for upper angle and 5 degrees for the lower angle of visibility.

### 3.7.6 Concept Evaluation and Selection

The four different concepts of powertrain layout concepts generated earlier have been evaluated in a selection matrix using twelve selection criteria's which are also placed within a priority rank as presented in Table 3.16. This qualitative assessment was based up on a design alternative evaluation scale, which has been used to assess the quality and feasibility of multiple design alternatives for a product, service, or system. It is a structured approach to evaluating the pros and cons of different design options, helping designers and decision-makers to make informed choices. Accordingly, the net results within each priority rank are multiplied by the priority weight factor which is 1.0, 0.5 and 0.25 for high, medium and low priority respectively. The highest and lowest scores of the criteria are defined shown in Table 3.17. Based up on the evolution of quantitative and qualitative screening criteria set, mid-loaded and the new clustered battery pack concept with 25% front and 75% mid-load has shown improved weight distribution. However, the most reported mid-loaded concept requires major modification of body structure.

Table 3.16: Packaging concept evaluation criteria and score (minimum and maximum)

| Criteria | Minimum score (1) | Maximum score (5) |
|---|---|---|
| Front impact safety | Not safe | Very safe |
| Side impact safety | Not safe | Very safe |
| Rear impact safety | Not safe | Very safe |
| Weight distribution (F:R) | (<40:60 and >60:40) | (50:50) |
| Extent of modification: | Major | Minor |
| Complexity of battery cooling design | complex | simple |
| Energy consumption for battery cooling | High | Low |
| Occupant packaging (ergonomics) | complex | simple |
| Suitable for BIW concept | Not suitable | suitable |
| Suitable for BEV | Not suitable | suitable |
| Easy for manufacturing | Hard | Easy |
| Benchmark layout | Less available | Highly available |

Table 3.17: Packaging concept selection criteria along with priority rank

| Rank | Selection criteria | Front | Rear | Mid | Clustered |
|---|---|---|---|---|---|
| High | Front impact safety | 1 | 5 | 5 | 3 |
| High | Weight distribution | 1 | 1 | 4 | 5 |
| High | Extent of modification | 2 | 2 | 2 | 4 |
| High | Energy consumption for battery cooling | 5 | 1 | 2 | 4 |
| Medium | Occupant packaging (ergonomics) | 5 | 5 | 3 | 4 |
| Medium | Side impact safety | 4 | 4 | 2 | 3 |
| Medium | Suitable for BIW concept | 1 | 3 | 4 | 4 |
| Medium | Suitable for BEV | 1 | 1 | 5 | 4 |
| Low | Rear impact safety | 5 | 1 | 5 | 5 |
| Low | Complexity of battery cooling design | 2 | 2 | 2 | 4 |
| Low | Maintenance | 4 | 4 | 3 | 4 |
| Low | Benchmark layout | 1 | 1 | 5 | 1 |
| | Net sum | 31 | 29 | 42 | 55 |
| | Weighted sum | 17.5 | 17.5 | 23.5 | 26.75 |
| | Criteria Qualification | No | No | Yes | Yes |

### 3.7.7 Modelling and Structural Analysis

#### 3.7.7.1 CAD model

Space allocated for battery pack was in front and under floor in passenger compartment as presented on Figure 3.27. The volume of front pack is (287mm×1600mm ×120mm) and the maximum dimension of mid-pack is (1887mm×1600mm×120mm). The lateral dimensions around car doors reduced by 350mm as shown on Figure 3.27(a).

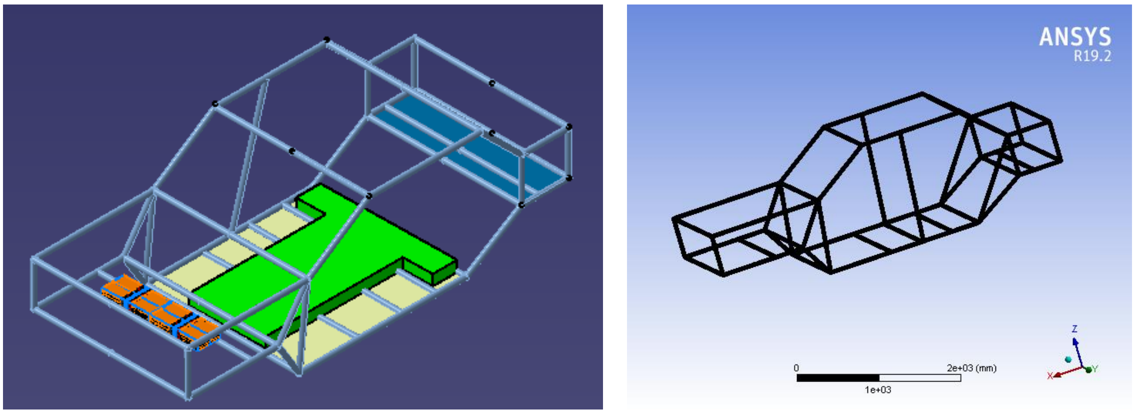


(a) CAD Model (b) Mesh

Figure 3.27: A CAD model (a) and mesh generated (b) on ANSYS workbench

An entire body structure of perimeter frames and cross members was designed for 60, 65 and 70mm diameter cross sections of 1mm thick as shown on Figure 3.27 (a).

The body model created was designed keeping in mind the geometric constraint requirements and further edited and disfeatured in ANSYS DESIGN MODELLER. Given that obtaining the most precise results was the goal of this research, a high order tetrahedral mesh model with 182505 elements and 60844 nodes was created, as seen on Figure 3.27 (b).

#### 3.7.7.2 Material selection

The benchmark BEV evaluation and lightweight parameters were taken into account while choosing suitable materials from a variety of types commonly utilized in vehicle body structures. Two materials, structural steel and aluminum alloy, were chosen for comparison. Aluminum alloy can be comparable with steel in strength, but at a third of the weight. It is much lighter, durable, and weather proof not affected by ultra violet (UV) rays.

Table 3.18: Important properties considered for materials

| Property | Aluminium alloy | Structural steel |
|---|---|---|
| Body structure mass | 31.227 | 88.495 |
| Battery Pack mass | 166.5 | 236 |
| Density (Kg/mm$^3$) | $2.77\times10^6$ | $7.85\times10^6$ |
| Poisson's ratio | 0.33 | 0.3 |
| Young's Modulus (MPa) | 71000 | $2\times10^5$ |
| Bulk Modulus (MPa) | 69608 | $1.6667\times10^5$ |

#### 3.7.7.3 Load and Boundary condition

Passenger vehicle body and structural assembly mainly manufactured as unified space frame to support all functional chassis systems and payload. Gravitational acceleration (9810 mm/s$^2$) is applied over the entire geometry. Front and rear suspension mounts are assigned as fixed support in all the conditions, except torsional loading case where front suspension is free to rotate about x-axis due to applied torque. Weights of powertrain including battery pack, controllers, motor and transmission along with payload under an effect of gravity is applied for static bending analysis. Frontal impact forces due to deceleration were calculated for three initial speeds of 120, 90 and 60km/h, which is equivalent to 30, 20 and 10g were applied. The structure is intended to provide full protection from intrusion to passenger compartment due to impact forces of 30g and destruction of battery pack by 10g. Finally 5, 4 and 3g side impact forces were applied on structure.

## 3.8 Aerodynamic Characteristics

The conversion strategy may cause changes to the position of the powertrain, exposing BEVs to aerodynamic drag and lift forces that affect stability even at lower speeds and consume power (Huluka & Kim, 2019). This study examined the aerodynamic characteristics of long-range capable BEV and low-speed Baja-Quit, focusing on power consumption and stability. The CAD model was developed for the two cars by using Catia-v5 software, imported to Phoenix CFD domain and numerical grid generated in the rectangular coordinate system. The same models were also imported to ANSYS software for comparative assessment between the implemented simulation tools as a cross validation {Lander, 2023 #459;Kavi, 2022 #474}.. {DINESH, 2022 #463}(Aiyan & Sagar, 2022). Calculations were conducted in optimized grid distribution obtained by thorough grid dependence evaluation and converged with an error cut off less than 0.01%. The aerodynamic characteristics were studied when the long range and low speed cars are moving at top speeds (120km/h) and (60km/h) respectively.

### 3.8.1 Aerodynamic Characteristics of the Car Body

When a vehicle is moving at a considerable speed, the air passing over it imposes various forces and moment on the vehicle (Sabater & Görtz, 2021). The essential coefficients of aerodynamic force and moments can be calculated by the following analytical relations.

$$C_L = \frac{F_L}{1/2\,\rho(V_\infty - V)^2 A} \tag{3.34}$$

$$C_D = \frac{F_D}{1/2\,\rho(V_\infty - V)^2 A} \tag{3.35}$$

$$C_S = \frac{F_S}{1/2\,\rho(V_\infty - V)^2 A} \tag{3.36}$$

$$C_{RM} = \frac{M_R}{1/2\,\rho(V_\infty - V)^2 At} \tag{3.37}$$

$$C_{YM} = \frac{M_Y}{1/2\,\rho(V_\infty - V)^2 At} \tag{3.38}$$

$$C_{PM} = \frac{M_P}{1/2\,\rho(V_\infty - V)^2 At} \tag{3.39}$$

where lift coefficient ($C_{L)}$ is lift coefficient, $F_L$ is lift force, $C_D$ is drag coefficient, $F_D$ is drag force, $C_S$ is side force coefficient, $F_S$ is side force, $C_{RM}$ is rolling moment coefficient, $M_R$ is rolling moment, $C_{YM}$ =is the coefficient of yaw moment, $M_Y$ is yaw moment, $C_{PM}$ is pitching moment coefficient, $M_P$ is pitching moment, $V_\infty$ is free stream velocity, V is total wind velocity, A is projected frontal area, and t is reference equal to wheelbase (L) may be taken.

### 3.8.2 Modelling and Definition of the Car Geometry

The long-range model car designed with new CMBP was derived from the existing modular electric drive matrix for BEV's conversion design based on BIW concept. Dimensions and technical parameters of the designed concept car and Bajaj quit car (for comparison of low speed aerodynamic characteristics) are presented on Table 3.19 and their CAD models are shown on Figure 3.28.

Table 3.19: Technical specification of model car

| Parameters | Long-range car | Bajaj Quit |
|---|---|---|
| Peak Power | 92 Kw @ 4000 RPM | 9.9 Kw @ 5500 (Kw @ RPM) |
| Maximum Torque | 220 Nm @ 4000 RPM | 19.6 @ 4000 (Nm @ RPM) |
| Passengers and driver mass | 375 kg | 375kg |
| Luggage and spare tire | 115 kg | 400Kg |
| Glider mass | 950Kg | 400Kg |
| Battery pack mass | 360Kg | 70Kg 30Kg |
| Motor and transmission mass | 85Kg | 30Kg |
| Controllers and on board charger mass | 65 kg | 15kg |
| Gross mass | 1950Kg | 800kg |
| Max. Speed | 160km/h | 70km/h |
| CD | 0.35 | 0.45 |
| CL | 0.035 | 0.035 |
| CG coordinate (X, Y, Z) | ( 1.9456,0.855, 0.592) m | ( 1.4,0.65, 0.8)m |
| Projected total area | 0.85×h×w =2.173m2 | 0.85×h×w =1.823m2 |

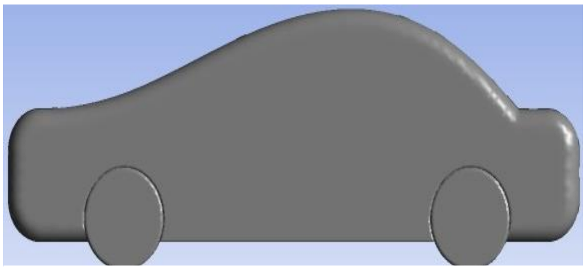

(a) Long range concept car

(b) Bajaj quit car

Figure 3.28: The CAD models of studied long range concept car (a) and Bajaj quit (b)

### 3.8.3 Definition of The Numerical Scheme

FVM (Finite Volume Method) scheme was employed to simulate flow phenomenon by considering side wind effect at 0m/sec, 10m/sec, 20m/sec, 30m/sec and 40m/sec. Numerical investigations have been conducted with ANSYS fluent work bench for the same conditions to simulate and solve equations of flow around the model vehicles. The general purpose CFD was used for a numerical calculation of the turbulent incompressible flow field. 3-D dimensional Navier-Stokes equations were solved with standard (K-Ɛ) turbulent model {Nisugi, 2004 #27}.

#### 3.8.3.1 Numerical domain and grid

The commercial software, Phoenix was used for building numerical grids using orthogonal grids and the CAD-to-CFD approach. To create the numerical grid within the rectangular coordinate system, the CAD model was imported into the defined numerical domain. (X, Y, Z) defines the domain's numerical size as (22 m, 6.8 m, and 5.5 m). The computation was carried out at the optimal grid distribution, as seen in Figure 3.28. This distribution was achieved by carefully evaluating grid independence via a number of iterations, and it converged quite nicely with an error cut off of less than 0.01%.

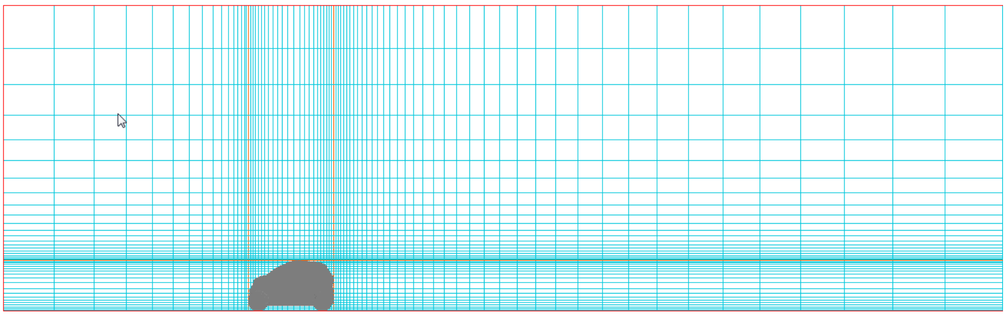

Figure 3.29: Computational domain and the imported car model in to Phoenix and Optimized computational grid of model car (47x94x41)

The same CAD models were imported to ANSYS fluent workbench using design modeler as shown on Figure 3.30. Starting with coarse mesh progressively fine mesh of 446,530 nodes and 2,608,561 elements was obtained after introducing inflation and tetrahedral mesh method. The optimized mesh obtained after grid independent test is shown on Figure 3.31(a). The flow type was considered turbulent, transient, and incompressible in developed boundary conditions, and it was treated to an appropriate boundary condition for the aerodynamic properties of the vehicle body. The definitions for initializing and boundary conditions are provided in Table 3.20. After 100 iterations, the residuals were observed to be stable, and the convergence criteria was 0.000001.

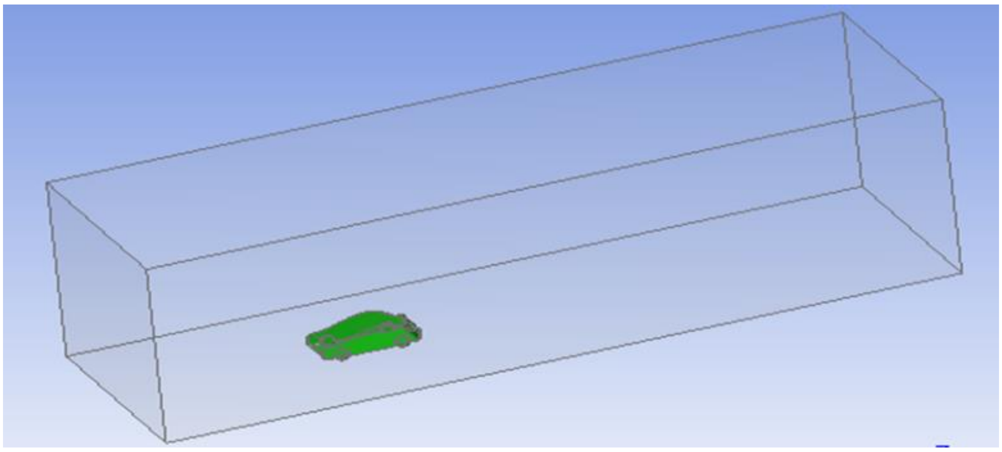

Figure 3.30: Computational domain and the imported car model in to ANSYS workbench

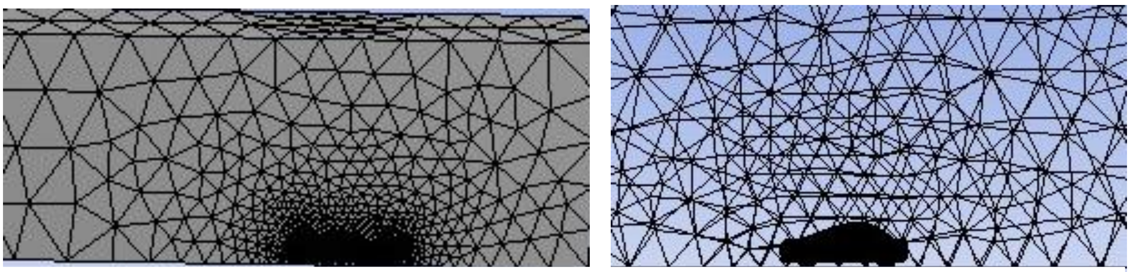

(a) Optimized Fine mesh (b) Coarse mesh

Figure 3.31: Optimized (a) and coarse (b) mesh in ANSYS numerical scheme

Table 3.20: Implemented boundary and the initial conditions

| Boundary surface | Boundary & initial conditions |
|---|---|
| Inlet-one | Longitudinal Velocity inlet (120 km/h) |
| Left side (Inlet-two) | Side wind Velocity inlet (0, 10, 20, 30, 40m/sec) |
| Outlet | Pressure outlet |
| Right Side and top | No slip wall condition |
| Ground | moving ground type |
| Flow domain | Quasi-3D flow, Turbulent and incompressible flow |

3.8.3.2 Governing Equations

The basic equations of fluid dynamics in the control volume are based on Navier stokes equations that are comprised of equation for conservation of mass and momentum are given as,{KIM, 2011 #29}

1. The Continuity equation

$$\frac{\partial U_i}{\partial x_i} + \frac{\partial U_j}{\partial y_i} + \frac{\partial U_k}{\partial z_i} = 0 \tag{3.40}$$

2. The Momentum equation

$$\frac{\partial U_i}{\partial t} + \frac{\partial}{\partial x_j}(U_i U_j) = -\frac{1}{\rho}\frac{\partial P}{\partial x_i} + \frac{\partial}{\partial x_j}\left[V\left(\frac{\partial U_i}{\partial x_j} + \frac{\partial U_j}{\partial x_i}\right) - \overline{u_i u_j}\right] - g_i \tag{3.41}$$

Where; $\overline{-U_i U_j} = v_t\left[\left(\frac{\partial U_i}{\partial x_j} + \frac{\partial U_j}{\partial x_i}\right)\right] - \frac{2}{3}k\sigma_{ij}$

3. Standard κ-ε model for turbulence; the turbulent kinetic energy equation

$$\frac{\partial}{\partial x_i}(U_j \mathrm{k}) = \frac{\partial}{\partial x_j}\left[v\left(v + \frac{v_t}{\sigma_k}\right)\frac{\partial k}{\partial x_j}\right] + G - \varepsilon \tag{3.42}$$

4. The Energy dissipation equation

$$\frac{\partial}{\partial x_i}(U_j \varepsilon) = \frac{\partial}{\partial x_j}\left[v\left(v + \frac{v_t}{\sigma_k}\right)\frac{\partial \varepsilon}{\partial x_j}\right] + \frac{\varepsilon}{k}\left(C\varepsilon_1 G - C\varepsilon_2 \varepsilon\right) \tag{3.43}$$

Where, reduction rate due to deformation

$$G = \overline{-U_i U_j} = \left[\left(\frac{\partial U_i}{\partial x_j}\right)\right] \qquad v_t = C_\mu \frac{k^2}{\varepsilon}$$

$(C_\varepsilon = 0.09,\ C_{\varepsilon 1} = 1.44,\ C_{\varepsilon 2} = 1.92,\ \sigma_k = 1.0,\ \sigma_\varepsilon = 1.0)$ k- turbulent energy, ε-dissipation rate, $v_l$ & $v_t$ laminar and turbulent kinematic viscosities(Ebrahim, Dominy, & Martin, 2020; Indrojarwo, Estiyono, & Pratama, 2019; Y. Li & Zhu, 2019).

## 3.9 Modelling of the Suspension System

This section presents an examination of how variations in weight distribution affect the ride comfort and roll stability of an EV conversion when it is subjected to random road profiles. It also offers suggestions for potential enhancements, which could be made using low-energy consumption devices. Two half-car models one for pitch-bounce and the other for roll-bounce were combined and used in the suspension system analysis using MALTLAB/Simulink to address the trade-off between inconsistent standards of road holding, ride comfort, and vehicle handling within the constraints of the suspension journey.

### 3.9.1 The Implemented Ride Car Model

In this study the development for seven-degrees-of-freedom (7DOF) vehicle ride model referenced (van Kempen, 2019) and (Lefèvre et al., 2020). In developing the mathematical model for an BEV conversion it is assumed that vehicle body is lumped into a single mass.

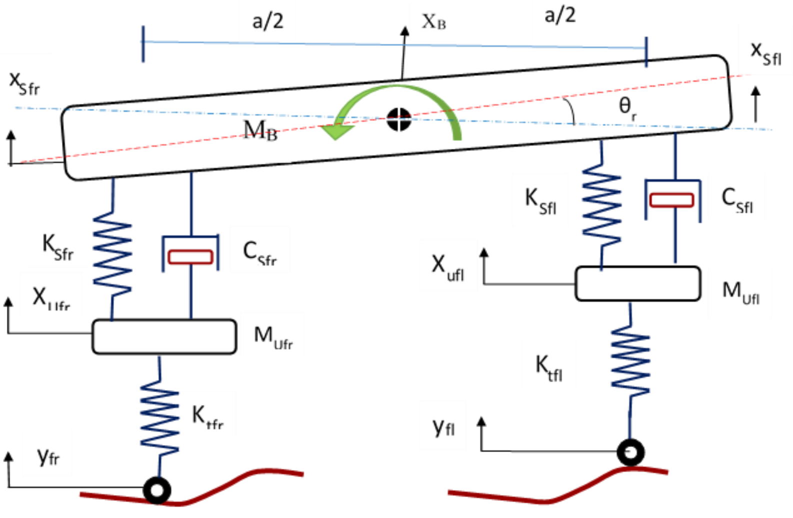


Figure 3.32: Half car for Bounce-roll model considering passive suspension

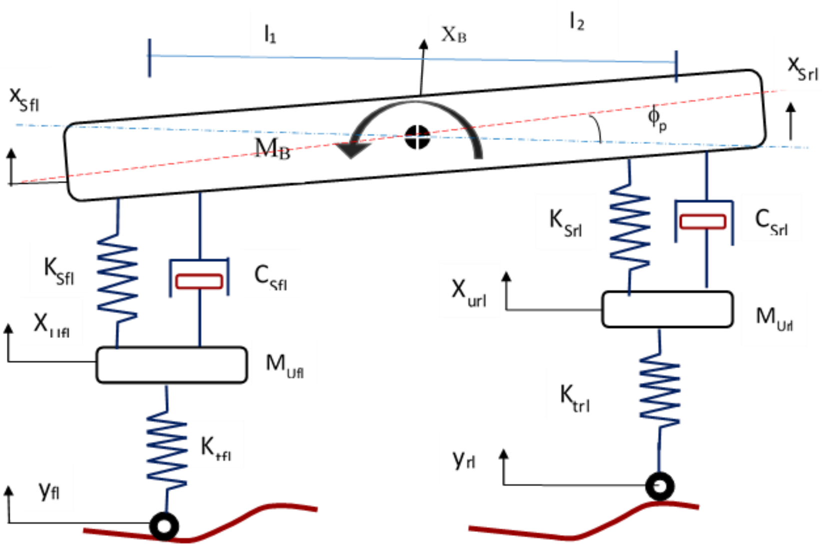


Figure 3.33: Bounce-pitch half car model of passive suspension system

This is referred to as the sprung mass. No effects of aerodynamic forces anti-roll bars and the control arm are considered, to reduce the complexity of the modelling and to prevent simulation error. It is assumed that the modelled vehicle will always remain grounded at all times and the four tyres always in contact with the ground during manoeuvring. In vehicle modelling, the roll and pitch deflections in their planes are small as shown on Figures 3.32 and 3.33 respectively and simplified with small angle approximation. While for the tyre, it is modelled as a linear spring without having damping characteristic. Dimensional and design parameters of the concept long range car are presented on Table 3.21.

Table 3.21: Essential parameters of the model car for suspension system evaluation

| Evaluation parameters | Value |
|---|---|
| Weight distribution (F:R) | 48:52 |
| CG height position | 592 mm |
| track | 1.495 m |
| Location of front axle from CG (l1) | 1.1856 m |
| Location of rear axle from CG (l2) | 1.0944 m |
| Un-sprung mass of front quarter car (Musf/2) | 59 kg |
| Sprung mass of front quarter car (Msf/2) | 409 kg |
| Un-sprung mass of rear quarter car (Mur/2) | 36 kg |
| Sprung mass of front quarter car (Msr/2) | 471 kg |
| Stiffness of tire (Kt) | 255487N/m |
| Stiffness of front suspension spring (Kf) | 45000N/m |
| Stiffness of rear suspension spring (Kr) | 36000N/m |
| The dampers' damping coefficient (Crf) | 5000Ns/m |
| The moment of inertia about x-axis (Ixx) | 719kg-m$^2$ |
| The moment of inertia about y-axis (Iyy) | 2495kg-m$^2$ |

### 3.9.2 Equations of Motion

By combining the two interdependent H-car models, 7DOF of ride model capable for evaluating bounce, pitch and roll responses of body and bounce of all four wheel un sprung mass developed. Analysing the kinematics of all four-corner quarter and the ride body of model car, the displacements of each quarter sprung masses are given calculated as;

$$X_{Sfl} = X_B + \frac{a}{2}\theta_r - l_1\phi_p \tag{3.44}$$

$$X_{Sfr} = X_B - \frac{a}{2}\theta_r - l_1\phi_p \tag{3.45}$$

$$X_{Srl} = X_B + \frac{a}{2}\theta_r - l_2\phi_p \tag{3.46}$$

$$X_{Srr} = X_B - \frac{a}{2}\theta_r + l_1\phi_p \tag{3.47}$$

Where $X_{Sij}$ is the total displacement of sprung masses (i =f for front, r for rear and j=l for left, r for right), $X_{Bj}$ is the sprung mass's vertical displacement at the COG, $\theta_r$ is the roll angle and $\phi_p$ is the pitch angle. The distances from CG to the front and rear centres of axle are given by $l_1$and $l_2$ respectively. Their value depends on the weight distributions at front and rear axles, the position of the CG of the vehicle. The forces on each of the suspension is computed as the sum of the spring force ($F_{Sij}$) and damper force ($F_{Dij}$). These suspension forces are given by;

$$F_{Sij} = K_{Sij}(\pm(X_{Uij} - X_{Sij})) \tag{3.48}$$

$$F_{Dij} = C_{Dij}(\pm(\dot{X}_{Uij} - \dot{X}_{Sij})) \tag{3.49}$$

with $K_{Sij}$ is the stiffness of the spring, $C_{Dij}$ the damping coefficient of the dampers $X_{Uij}$ un-sprung mass vertical displacement and $X_{Sij}$ the sprung mass vertical displacement at each side of the vehicle.

The tires are modelled as a spring and the force acting at the tires is usually known as dynamic tire loads, $F_{tij}$ is given by;

$$F_{tij} = K_{tij}(\pm(X_{rij} - X_{Uij})) \tag{3.50}$$

where, $K_{tij}$, and $X_{rij}$ are the tire stiffness and road input displacement respectively.

Using Newton's Second Law at the vehicle's sprung mass, the body vertical acceleration, $\ddot{X}_B$, angular acceleration $\ddot{\theta}_r$ during the roll effect and the angular acceleration $\ddot{\phi}_p$ while the vehicle's pitching effect can be computed by equations (Xia et al., 2020)

$$F_{fl} + F_{fr} + F_{rl} + F_{rr} = M_{VG}\ddot{X}_B \tag{3.51}$$

$$(F_{fl} + F_{rl})\frac{a}{2} - (F_{fr} + F_{rr})\frac{a}{2} = I_{xx}\ddot{\theta}_r \tag{3.52}$$

$$(F_{rl} + F_{rr})l_2 - (F_{fl} + F_{fr})l_1 = I_{yy}\ddot{\phi}_p \tag{3.53}$$

Where, $M_{VG}$ is the total mass of the vehicle. $I_{xx}$ is the inertia moment about x-axis and $I_{yy}$ is the inertia moment about y-axis.

The acceleration for each wheel can be determined using equations [3.54-3.57]

$$F_{tfl} - F_{Sfl} - F_{Dfl} = M_{Ufl}\ddot{X}_{Ufl} \tag{3.54}$$

$$F_{tfr} - F_{Sfr} - F_{Dfr} = M_{Ufr}\ddot{X}_{Ufr} \tag{3.55}$$

$$F_{trl} - F_{Srl} - F_{Drl} = M_{Url}\ddot{X}_{Url} \tag{3.56}$$

$$F_{trr} - F_{Srr} - F_{Drr} = M_{Urr}\ddot{X}_{Urr} \tag{3.57}$$

Using Equations 3.44-3.57 Simulink model was developed along with matlab code for execution of the whole setup and to tune the implemented control strategy in active suspension model. Figure 3.34: depicts the vehicle model developed in Simulink window.

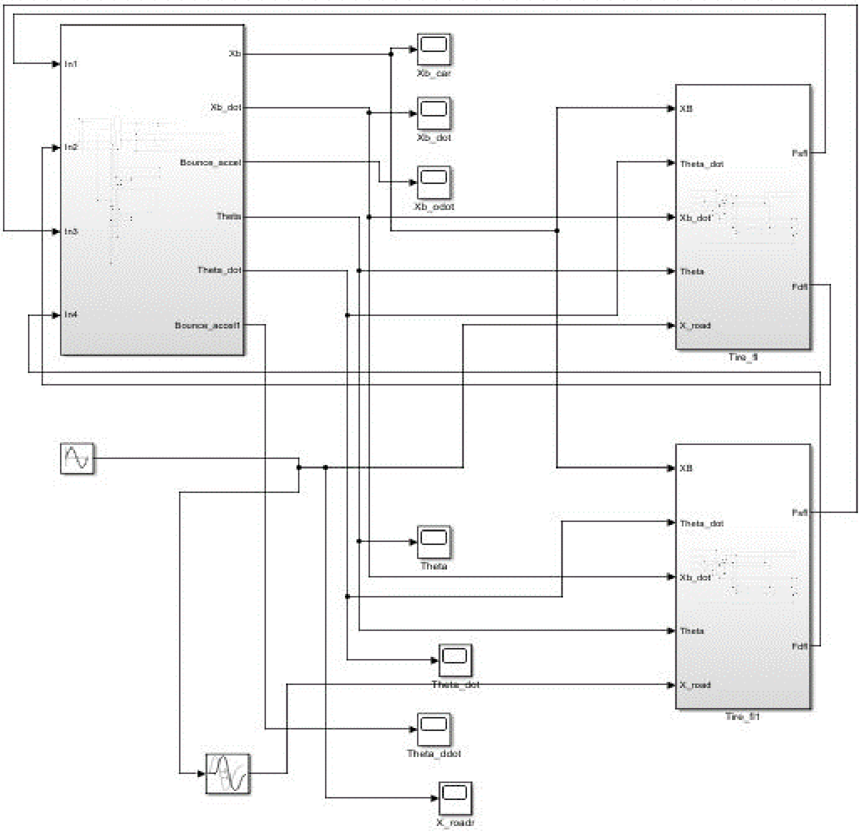


Figure 3.34: Simulink model of full car for suspension ride and handling assessment

Table 3.21 presents the tabulated suspension system parameters used for this study. The assumptions for modelling 7 DOF ride car of linear suspension system are:

- The front and rear tires act as spring with no damping effect.

- There is rotational motion in the sprung car body, wheels rotational motion are not considered.
- It is assumed that all springs and dampers are linear.
- The tires are always in contact with road surface, but the effect of friction between surface of the road and tires are neglected.

The suspension system's ability for providing optimal comfort and road handling by keeping the car well-isolated from unforeseen road disturbances within a reasonable deflection range served as the basis for evaluation.

# CHAPTER FOUR

# RESULTS AND DISCUSSIONS

## 4.1 Synthesized Drive Cycle

### 4.1.1 Results of Statistical Analysis

The analysis of trip distances one of the representative real data trip features is shown in Figure 4.1 (a) and recorded an average value of 7.28 km, with the highest frequency in the range of 3-4.5 km. Furthermore, 80 % of the trip distances covered less than 9.83 km in CDF. It should be noted that the driven distance of a candidate DC was found to be in a range of 4 km to 15 km, but must be near the established CDF value. Regarding trip duration, 25 % recorded the highest frequency with a duration of about 750 seconds (12.5 minutes). Additionally, the third quartile, as indicated in Figure 4.1(b), was located at 1358 s (22.63 min). Hence, the representative driving cycle should be close to the third quartile, while the duration was adjusted to 1320 s (22 min) to minimize the computational burden.

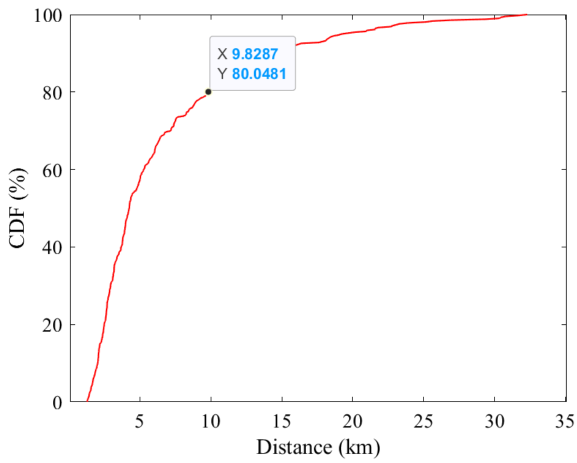


(a) Cumulative distribution of trip distance

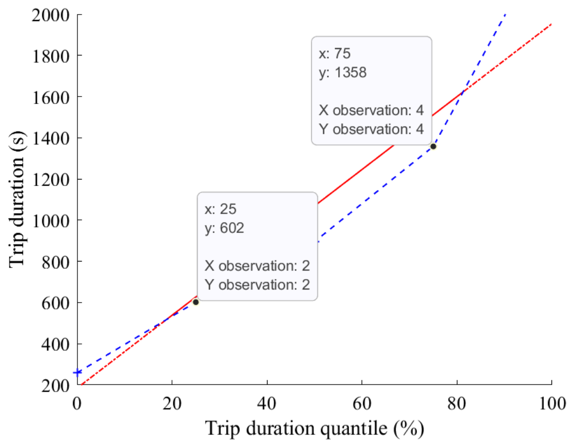


(b) Quartile distribution trip duration

Figure 4.1: Distance and duration distributions of real-time trip cycles.

A significant difference of 46 % was noted between average speeds (w/o stop) and average driving speeds (w/stop) in the low-speed phase compared with 8 % in the high-speed phase as shown in Figure 5 (a) and (b). This indicates that the influence of stop time on average vehicle speed was based on the percentage of stop time.

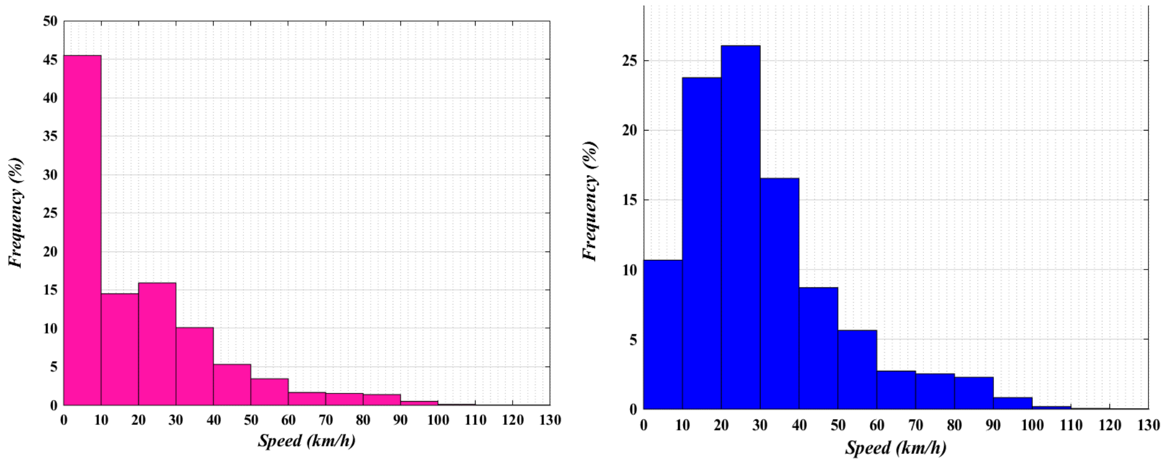


(a) Average driving speeds with stops (b) Average driving speeds without stops

Figure 4.2: Comparison of driving speeds.

After analysing the CFD of all ten (10) ST in the low speed phase, it was found that more than 80 % was primarily coincided with 64 s and a high frequency (55 %) occurred below 20 s (see Figure 4.3 (a) and (b)). Hence, the fifth MT with an average speed of 18 km/h and lasting 64 s was found to be the best fit with real data and was selected to be the first MT of the low-speed phase. A stop duration between MTs would be steady sampling and to address the smooth transition, it was decided that the average stop duration of the trip cycle would be 11 s.

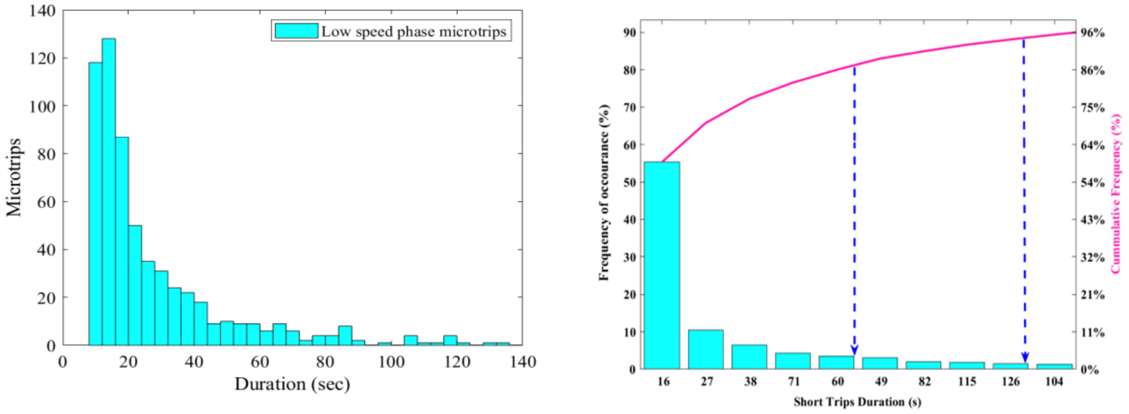


(a) The frequency of MT duration (b) Cumulative frequency of MT duration

Figure 4.3: The distribution of low-speed short trip duration

Figures 4.4 (a) and (b) illustrate the distribution of acceleration-related principal components used for acceleration and braking behaviour splitting for characterizing driving behaviour.

High-speed phases have a low average positive acceleration (APA), RPA and time idling, but a long distance. A medium APA, high RPA, medium distances and medium stop time represent the medium-speed phase. Finally, the low-speed phase was found to have a high APA, medium RPA, high stop time and shorter distances.

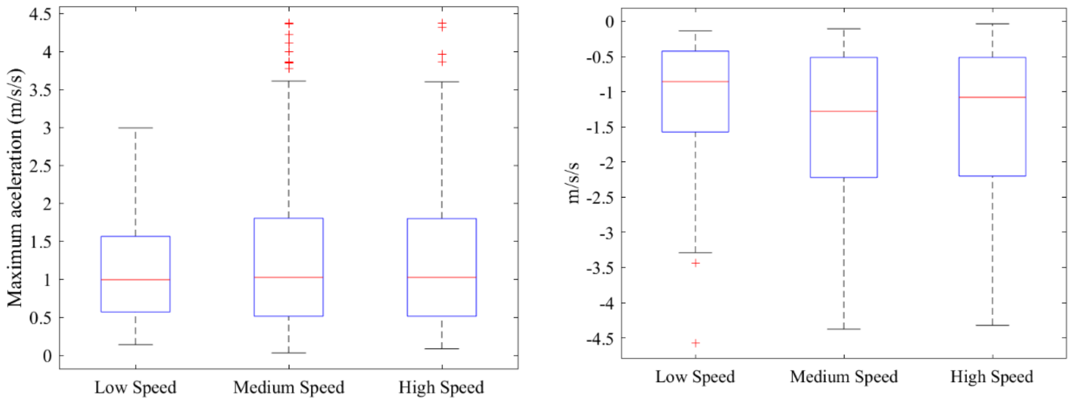


(a) Acceleration distribution (b) Deceleration distribution

Figure 4.4: Acceleration and deceleration distribution of all speed range trip cycles.

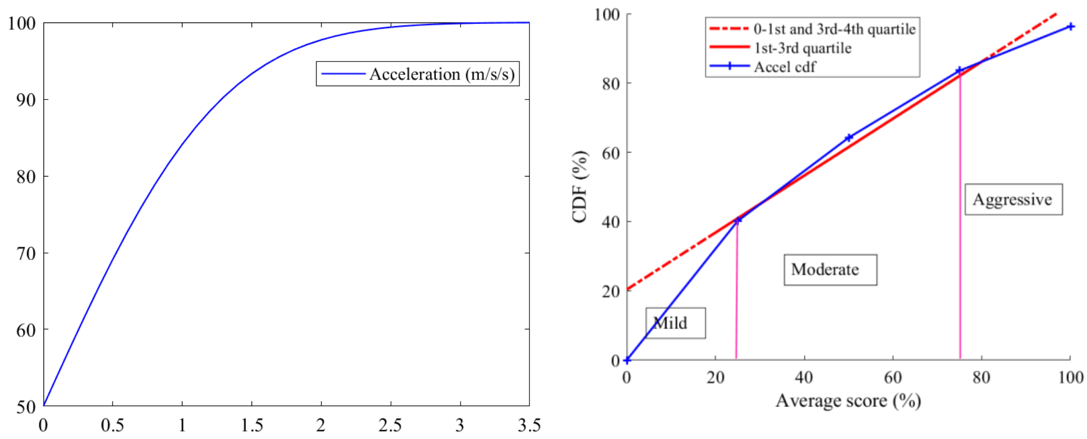


(a) CDF of acceleration (b) Quartile score of acceleration on CDF

Figure 4.5: Cumulative distribution function and its quartile score of acceleration.

Different CDFs for positive and negative acceleration features were obtained, as shown in Figure 4.5 (a), and driving behaviours were identified by dividing the average position of each MT on the CDF graph of the 0-1$^{st}$ quartile, 1$^{st}$-3$^{rd}$ quartile and 3$^{rd}$-4$^{th}$ quartile.

The driving behaviour with an average $a^+ < 0.5$ m/s$^2$ was identified as mild and with $a^+ >$ 2m/s$^2$ as aggressive, with behaviour between the two being average (D. Zhao et al., 2022). As shown in Figure 4.5 (b), a driving behaviour of the 0-1$^{st}$ quartile scored by 40 % is mild, 1$^{st}$-3$^{rd}$ quartile scored by only 40 % is average, and 3$^{rd}$-4$^{th}$ scored by 20 % is aggressive.

Consequently, only 40 % of MTs, rather than half, were considered to be average drivers identified by moderate braking. Hence, a representative AASU DC must be constructed by incorporating 40 % mild, 40 % moderate and 20 % aggressive behaviours in both ascending and descending speed profiles.

### 4.1.2 Drive cycle Synthesized by the RSBS Method

The speed-acceleration distribution of the synthesized four cycles (i.e. mild, aggressive driving, aggressive braking, and combined) are presented in Figures 4.6 and 4.7.

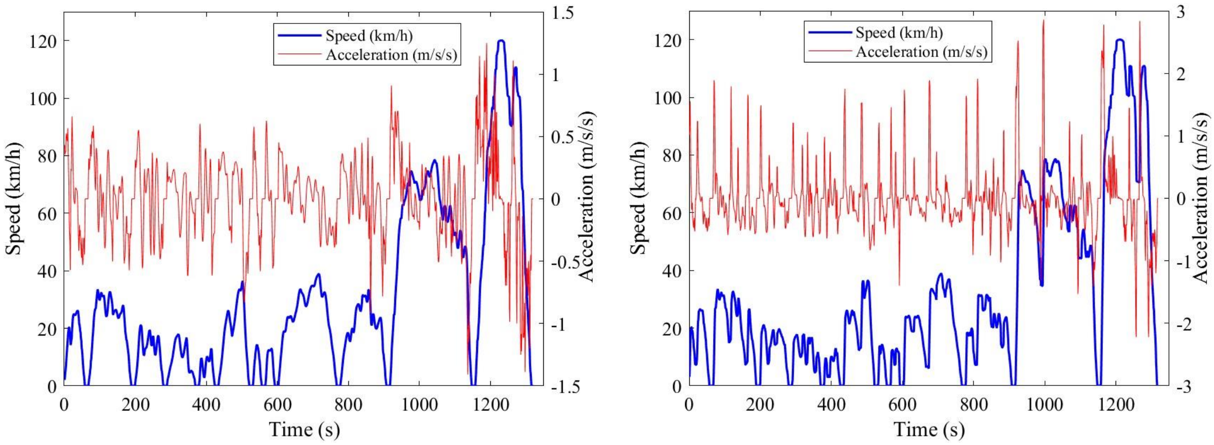


(a) Mild DC

(b) Aggressive driving DC

Figure 4.6: Speed-acceleration distributions of AASU DC by the RSBS method.

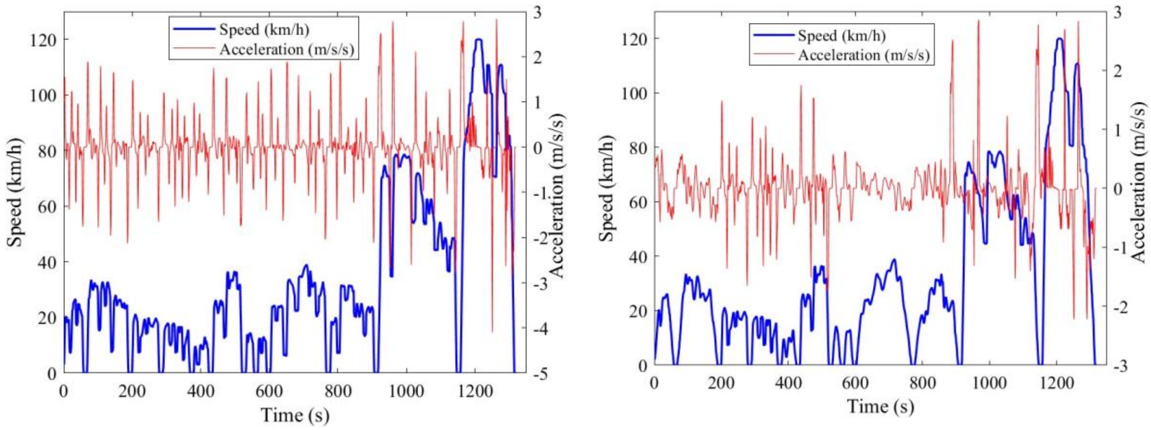


(a) Aggressive driving and braking DC

(b) Combined behaviors DC

Figure 4.7: Speed-acceleration of the RSBS's DC for aggressive and combined behaviors.

After behaviour division, the speed difference between mild and aggressive was considerably lower, but a remarkably high variation existed between accelerations in the two behaviours. This variation was lower for the low phase and higher for the high phase. Hence, it could be concluded that as the speed increases, the gap between quartile one and quartile three decreases for both positive and negative accelerations.

For mild cycles (see Figure 4.6), a low variation in acceleration was found among different driving profiles (-3.75 %) with an increase in driving speed, but for aggressive driving the variation was higher (-22.5 %). Although, behaviour splitting has a significant influence on urban cycles, a considerable dispersion in acceleration-related features was found in the medium and high-speed segments

### 4.1.3 Drive Cycle Synthesized by the k-means Method

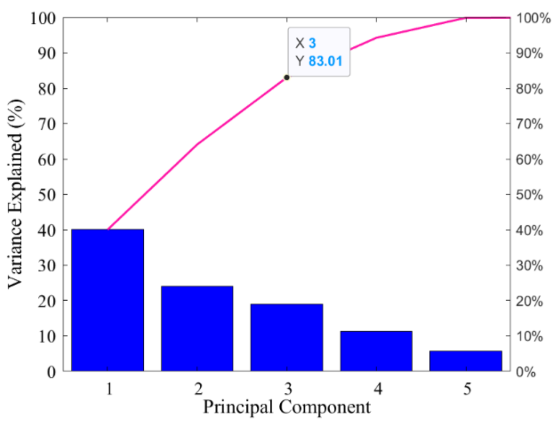


(a) Pareto highest variance explained by PCs

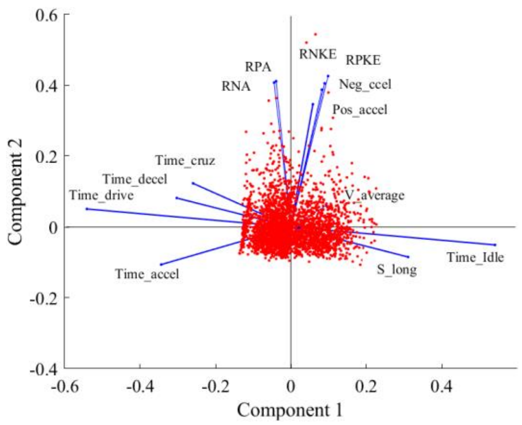


(b) Bi-plot of eigenvectors and eigenvalues

Figure 4.8: The influence of driving features on PCs and their variance explained.

The Pareto graph in Figure 4.8 (a) indicates that only five (5) principal components (PC) achieved the explained variability of 99.8 % rather than the twelve (12) PC implemented. The variance explained by the first, second and third PCs was 40 %, 22.6 % and 19.4 % respectively, and the total variance explained by employment of the first three PCs was correct since they represented about 82.01 % of the data set variability.

The two-dimensional bi-plot presented in Figure 4.8 (b) shows the contribution and influence of the driving features on the first two PCs. The highest variability was found in speed-related features, distance and time percentage of stop, because they were the main contributors to the variance explained by the first PC. Acceleration-related features, including APA, ANA, RPA, RNA, PKE and negative kinetic energy (NKE), mainly influenced the second component. The third component was mainly affected by the stop and time proportion of each kinematic mode.

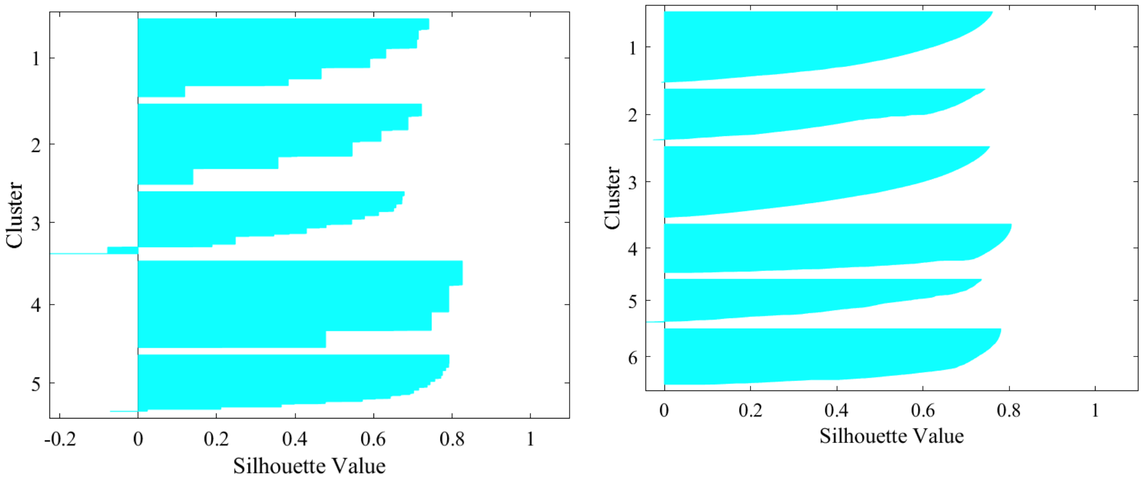


(a) Width and value of five clusters

(b) Width and value of six clusters

Figure 4.9: Score of silhouette value and distribution of width for five and six clusters

The three PCs were grouped by k-means into the optimum number of six clusters, as shown in Figure 4.9 (b) with the higher silhouette value of 0.78, and uniform width obtained when compared with the 0.74 silhouette values and non-uniform widths of five clusters shown in Figure 4.9 (a). ST were then selected from all the clusters based on their closeness to the cluster centres until a total duration of 1320 s was obtained.

### 4.1.4 Characteristic Distribution of Synthesized Drive Cycles and Real Dataset

Relative, mean relative, and root mean square errors of speed and acceleration-related features between candidate DCs and entire dataset were calculated. The difference between the speed distributions of the real data from DCs by the RSBS and k-means methods were compared and are shown in Figure 4.10 (a) and (b) respectively.

The average difference of RSBS DC from real data was found to be lower (2 %) than that of the higher (5 %) k-means DC. Other statistical properties are compared in Table 5, which indicates that there was a significant distortion in the statistical distribution of k-means DC from the original data set. However, the relative error between RSBS DC and real data was the lowest, and this was selected as the best representative BEV DC for AASU routes.

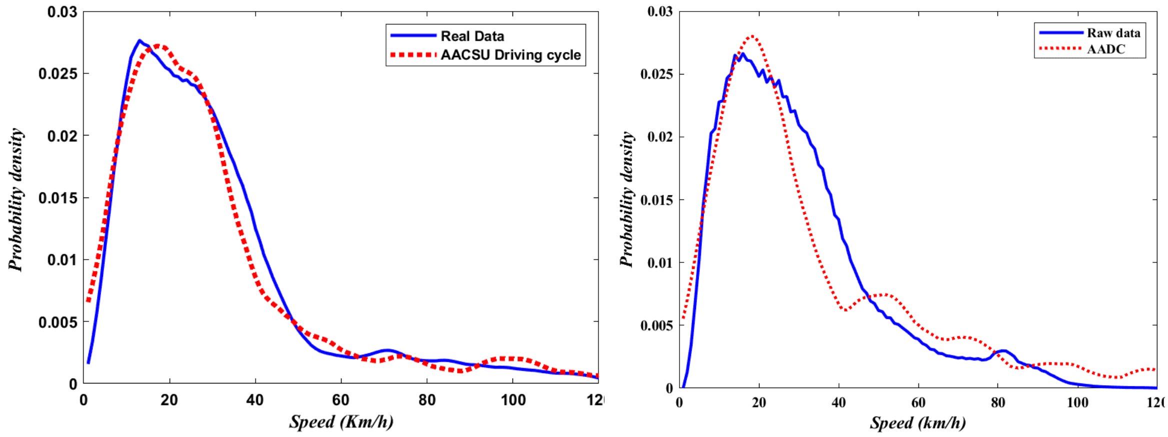


(a) Real data and RSBS DC

(b) Real data and k-means DC

Figure 4.10: Comparison of speed distribution between real data and RSBS and k-means

Table 4.1: Essential characteristics of RSBS, k-means, WLTC-2 DCs and real data.

| **Drive cycles** | **Cycle Phase** | **Duration (s)** | **V w/o stops (km/h)** | **V w/stops (km/h)** | **$a_{ave}$ ($m/s^2$)** | **$d_{ave}$ ($m/s^2$)** | **D (km)** | **RPA ($m/s^2$)** | **RNA ($m/s^2$)** |
|---|---|---|---|---|---|---|---|---|---|
| | Low | 882 | 19.8 | 17.6 | 0.43 | -0.46 | 4.196 | 0.185 | -0.22 |
| RSBS | Medium | 255 | 56.1 | 53.7 | 0.625 | -0.705 | 2.942 | 0.5 | -0.66 |
| | High | 183 | 81.4 | 73.9 | 0.45 | -0.61 | 2.835 | 0.29 | -0.32 |
| k-means | Low | 950 | 18.9 | 16.7 | 0.645 | -0.645 | 4.42 | 0.43 | 0.40 |
| | Medium | 240 | 40.4 | 36.4 | 0.54 | -0.705 | 2.43 | 0.56 | 0.65 |
| | High | 132 | 85.4 | 82.1 | 0.625 | -0.621 | 3.01 | 0.72 | 0.91 |
| Real data | Low | 101994 | 21.30 | 14.7 | 0.44 | -0.36 | 400. | 0.34 | -0.29 |
| | Medium | 26227 | 59.75 | 33.4 | 0.54 | -0.74 | 249.9 | 0.63 | -0.62 |
| | High | 17485 | 94.9 | 78.1 | 0.39 | -0.42 | 740.7 | 0.45 | -0.36 |
| WLTC-2 | Low | 589 | 26.0 | 51.4 | 0.92 | -1.07 | 3.132 | 0.244 | 0.2112 |
| | Medium | 433 | 44.1 | 74.7 | 0.96 | -0.99 | 4.712 | 0.629 | 0.2489 |
| | High | 455 | 57.8 | 85.2 | 0.85 | -1.11 | 6.820 | 0.962 | 0.1994 |

### 4.1.5 Comparison of Energy Consumption between Standard and AASU DCs

In a typical DC, the tractive effort provided by a vehicle's power/energy source must overcome all road loads, including aerodynamic, rolling, gravitational and acceleration resistance expressed. Estimation of the on-board ESS for BEV was averaged cumulative energy as a function of driving speed over the interval dt:

$$E_{Total} = \int_0^{t_f} F_{tra} v(t)dt = \int_0^{t_f} P(t)dt \tag{4.1}$$

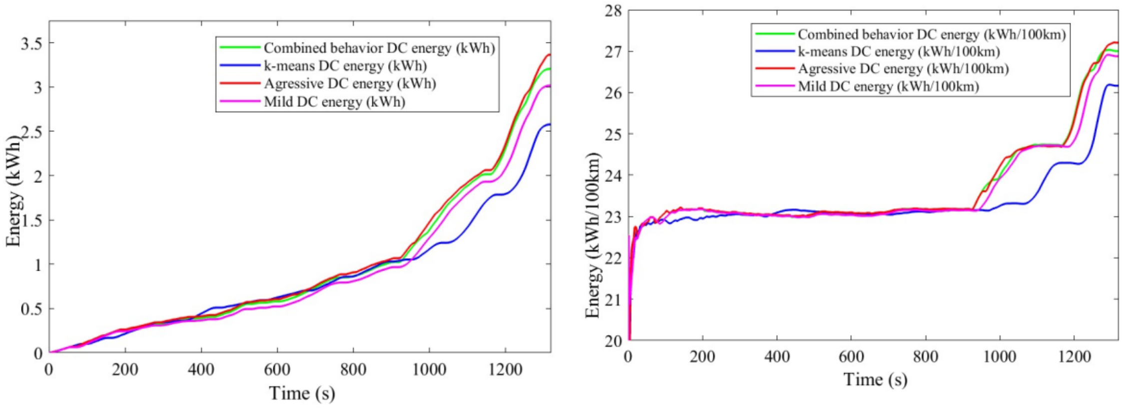


(a) Cumulative consumption rate (kWh) (b) Consumption per range (kWh/100 km)

Figure 4.11: Energy consumption of AASU DC for different driving behaviors.

The energy consumed by a 2000 kg midsize car to negotiate the road load was calculated from the candidate AASU DC among different behaviours for comparison. In Figure 4.11 (a), the area under the curve of the aggressive cycle peaked higher at 3.34 kWh at a greater speed compared with the mild cycle's 3 kWh. Figure 4.11 (b) shows energy consumption per 100 km. High consumption at high speeds was due to the coupled effect of high speed with high acceleration, which has a considerable correlation with energy consumption.

Figure 4.12 (a) and (b) show a comparison of the effect of braking behaviour division on regenerative potential with coast and panic braking. More braking kinetic energy of 1.65 kWh (21.2 %) was wasted by aggressive drivers than the 1.3 kWh wasted by coast drivers. Studies have indicated that the regeneration potential with current advances was only 8 % of energy for aggressive and up to 25 % for coast drivers (Z. Gao et al., 2019).

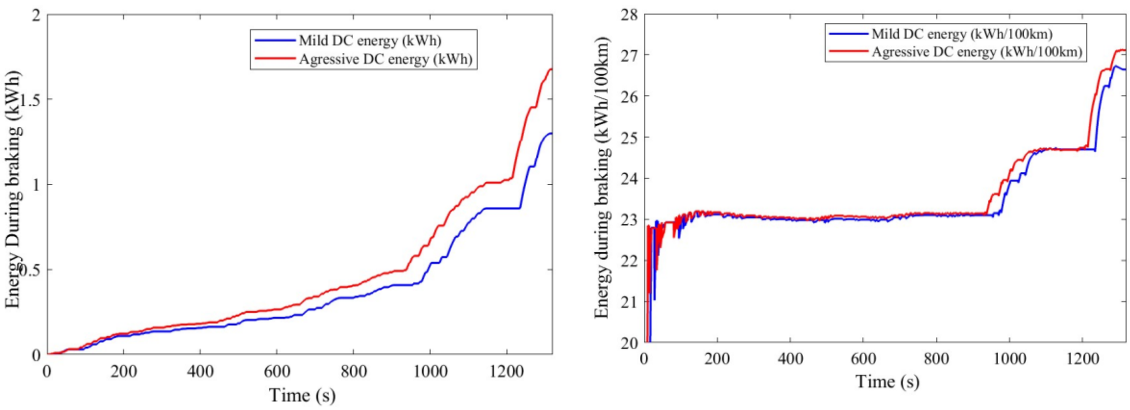


(a) Cumulative rate of regeneration (kWh) (b) Regeneration per range (kWh/100 km)

Figure 4.12: Regenerative potential AASU DC for mild and aggressive driving

Accordingly, the regenerated energy can extend the range per single charge of BEV by 10.8 % and 3.9 % for coast and aggressive drivers respectively. Hence, splitting behaviour and ignoring braking mode will result in a significant error in net energy consumption estimation and battery size due to the distortion in characteristics of DC synthesized from that of a real driving scenario.

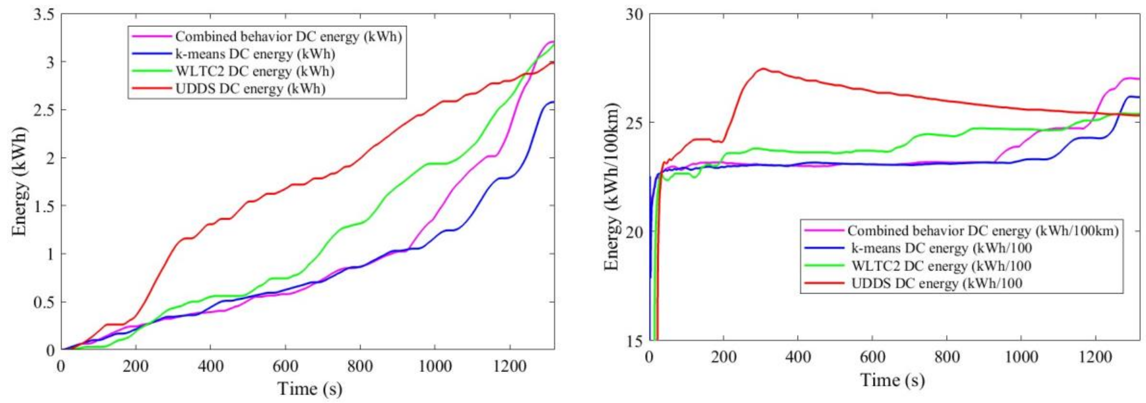


(**a**) Cumulative consumption rate (kWh) (**b**) Consumption per range (kWh/100 km)

Figure 4.13: Energy consumption of WLTC-2, UDDS, AASU-RSBS and k-means DCs.

Finally, the averaged RSBS DC was compared with k-means, WLTC-2 and UDDS cycles (Barethiye, Pohit, & Mitra, 2017). The standard cycles were selected based on equivalence in total duration of WLTC-2 1477 s and UDDS 1400 s, method of construction and data representativeness. WLTC-2 has the highest maximum acceleration of all cycles, which was thought to be more realistic. The maximum acceleration of UDDS was lower compared with transient cycles.

The cumulative energy consumption rate and consumption per 100 km by RSBS, k-means, WLTC-2 and UDDS DC were calculated and the results are shown in Figure 4.13 (a) and (b). Less energy was consumed by RSBS DC than by the WLTC-2 and UDDS cycles at a wide operating range, except at peak velocity. A significant difference was found with low overall net consumption per 100 km range of 22.5 kWh compared with 24.25 kWh and 26.34 kWh of WLTC2 and UDDS net consumptions respectively. Net consumption by RSBS and k-means DC was comparable at low speeds, however at higher speeds the k-mean consumed less due to the average low acceleration dispersion.

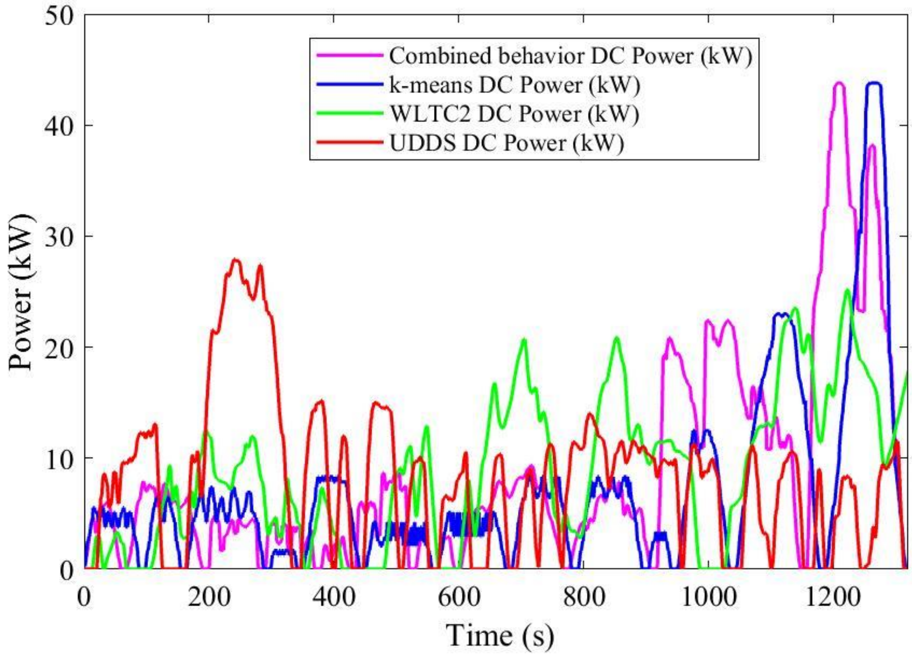


Figure 4.14: Power consumption of WLTC-2, UDDS, AASU-RSBS and k-means DCs.

For the high-speed expressway part of the RSBS DC, a distinct operating point could be found at 120 km/h, where more energy is consumed and power demanded (see Figure 4.14). However, this was because of the higher drag force and was not related to driving behaviour. Although the consumption was high for high speed, the proportion of the route segment was only 10 % compared with 70 % for urban and 20 % for suburban routes, and the influence on net energy demand per range was insignificant. WLTC-2 demanded high power in the urban DC due to the maximum speed coupled with aggressive acceleration within a short driving range, whereas UDDS required moderate power in a representative rural section, except in an aggressive single trip.

## 4.2 Powertrain Size and Energy Management

This section presents the results and discussion of the simulations performed. The EV profile is similar to the AASU route, whereas UDDS and WLTC2 cycles were simulated for comparative analysis. The PID controller converts the error into signals for the accelerator and brake pedal, as shown in Figure 4.15: for the AASU cycle. The deviation of vehicle and cycle speed was in the range of 0.1-0.4km/h and 0.2-0.5 for the Urban and large cars respectively. Since the average error is less than 0.2 the controller is capable of tracking the reference cycles.

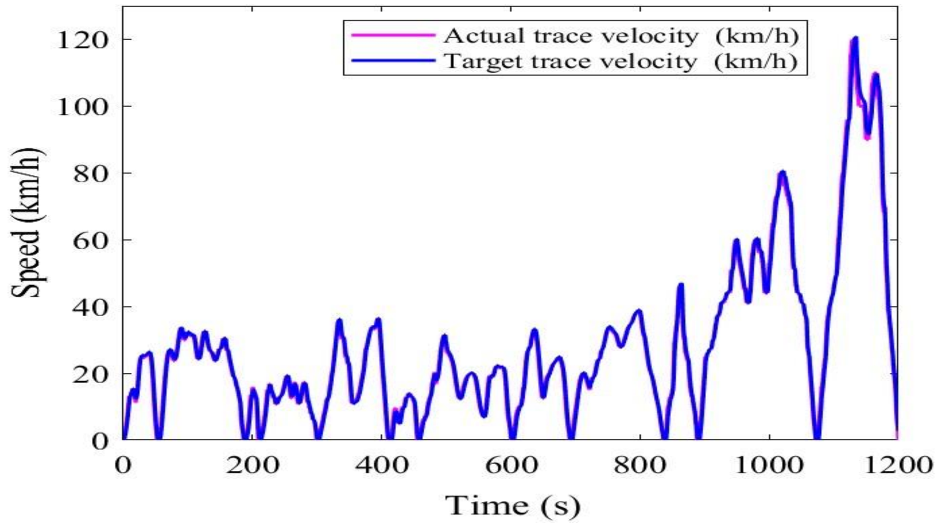


Figure 4.15: Actual and reference speed profiles in the AASU cycle

Figures 4.16: show the SOC of the battery bank throughout the driving profile for AASU, UDDS and WLTC2 cycles simulation. For the AASU cycle, the initial SOC (91%) was reduced by 4.1% and 4.5% for urban and long-range cars respectively. A 4.9% reduction with a sharp decline has been observed for long-range simulation with WLTC2. This could be due to the high frequency of acceleration throughout the cycle.

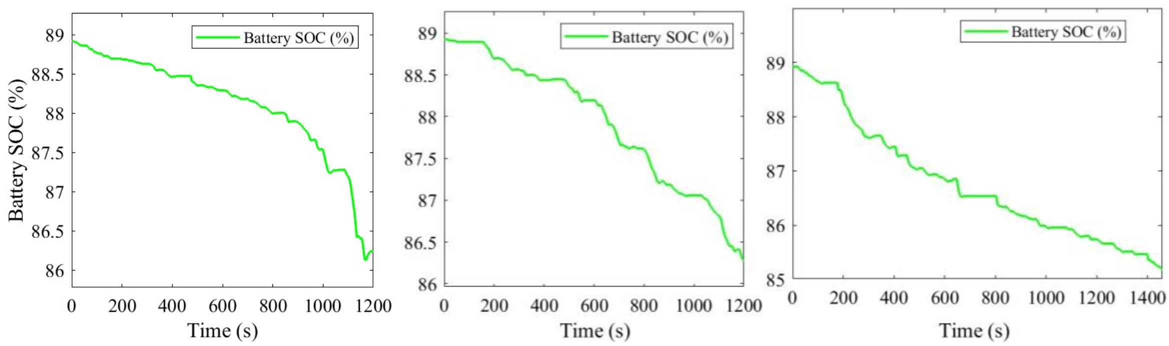


(a) AASU DC (b) WLTC-2 DC (c) UDDS DC

Figure 4.16: SOC of the long-range car's battery for AASU, WLTC2 and UDDS DCs.

The battery delivers a maximum current of 115A for urban cars, whereas 225A drown for long range to complete one cycle of AASU as shown in Figure 4.17. It revealed that the long-range battery current fluctuates between minimum value -100A and maximum value of 225A only on highway.

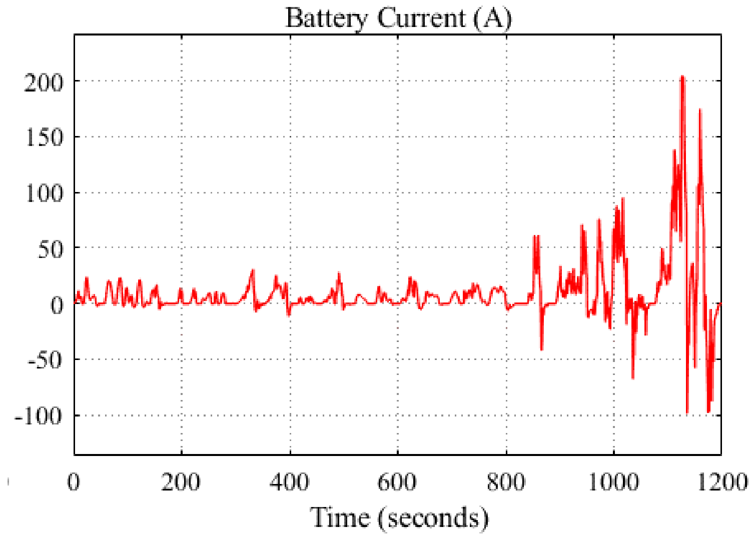


Figure 4.17: AASU drive cycle battery current fluctuation for long range

As can be seen in the map shown (see Figure 3.23): the efficiency reaches a maximum value of 0.96 for both cars. Since the area where efficiency is greater than 0.90 covers more than 50% of the entire region, the sized machine is very effective in most areas of operation. When two-speed transmissions are used the rated motor torque can be downscaled from 250Nm to 220Nm. Further results can be found on Figures C.2 and C.3.

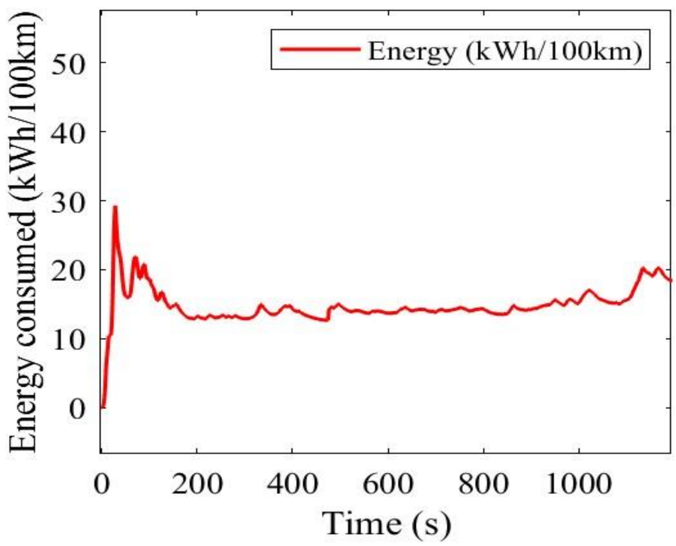


Figure 4.18: Energy consumption per 100km for long range car for AASU DC

Figures 4.16 and 4.18: depicts that battery energy consumption highly depends on the drive cycle and less on the powertrain. The lowest consumption for the AASU cycle is due to cycle parameters identified by relatively low-speed levels, which accounts for 70% of the cycle and the lowest level of acceleration. In general, cycles with the highest discharge energy consumption are also those with the highest levels of acceleration and RPA value.

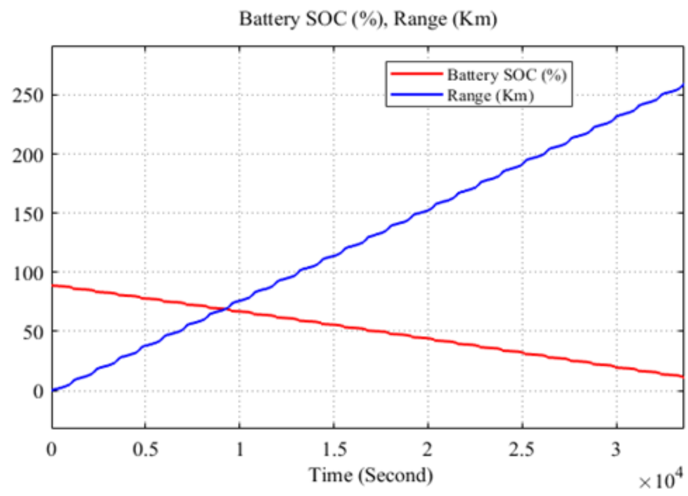


Figure 4.19: Battery SOC and range calculated for long range car in AASU cycle

The long-range car's total range by full battery charge was simulated along with the SOC of the battery as the illustrative example presented for the AASU cycle in Figure 4.19. The maximum driven distances were 269.7 km for AASU and 247.5km for WLTC. Similarly, the average cycle efficiency was 88.7% for AASU, which is higher than estimated (85%) when seeking suitable battery energy content for the range requirement.

Table 4.2: Summary of energy consumption range and average cycle efficiencies

| Test cycle | Energy (kWh/100Km) | Range (km) | Average Efficiency | Decrease battery size (kWh) |
|---|---|---|---|---|
| AASU | 17.436 | 269.9 | 88.7 | -3.4 |
| WLTC2 | 17.989 | 258.7 | 87.8 | -1.52 |
| WLTC | 23.985 | 247.5 | 84.7 | +0.5996 |
| UDDS | 19.802 | 240.5 | 84.0 | +1.88119 |

In this illustrative example of the long-range car, the battery energy content was estimated to be 85% of 42 kWh, resulting in a range of 264.5km. The discrepancy with the value in Table 8, could be the consequence of the assumed lower efficiency and energy content of the battery which in the simulation varies depending on the load situation. The total energy of 17.436kWh was contributed by the battery (13.495kWh) and the remaining accounts for regenerated energy (3.941kWh). It can be seen that the lower energy consumption for the

Addis Ababa and its suburbs (AASU) cycle generally provides 5-20 km more than the WLTC cycle, while the range is shortened by about 10 km for the UDDS cycle.

## 4.3 Powertrain Integrated Car Body and Structure Analysis

### 4.3.1 Modal Analysis

Initially Free-free modal analysis was simulated to test the connectivity of each part to unite body considering ten modes of natural frequency. It was found that all parts respond as one body for all modes with maximum frequency of 51Hz as shown on Figure 4.20 (a). However, pre-stressed modal analysis is used for finding most frequently stressed mode along with maximum deformation. The results are obtained for the first ten modes along with the corresponding natural frequencies and displacements. The maximum frequency was found to be 76.675Hz with corresponding total deformation of 17.242mm in 10$^{th}$ mode at upper corner member of backlight window as highlighted in red on Figure 4.20 (b). Hence, torsional load case is the most severe and if the structure is designed stiff enough in torsion, it guarantees for bending and lateral loads.

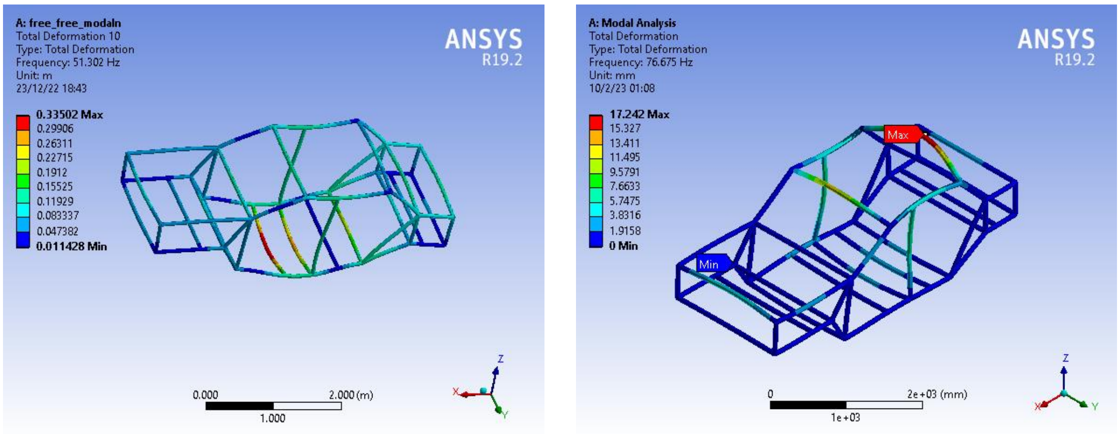


(a) Free-free (b) Pre-stressed

Figure 4.20: Natural frequency and deformation for Free-free (a) and pre-stressed (b)

### 4.3.2 Torsional Analysis

From contour of Figure 4.21 (a) and (b) stress induced in aluminium frame (207MPa) is nearly equal to that of steel (205MPa), whereas deformation is three times higher. Although, the stress is less than yield strength, this design is not in acceptable limit as safety factors are 1.27 and 1.35 for steel and aluminium respectively.

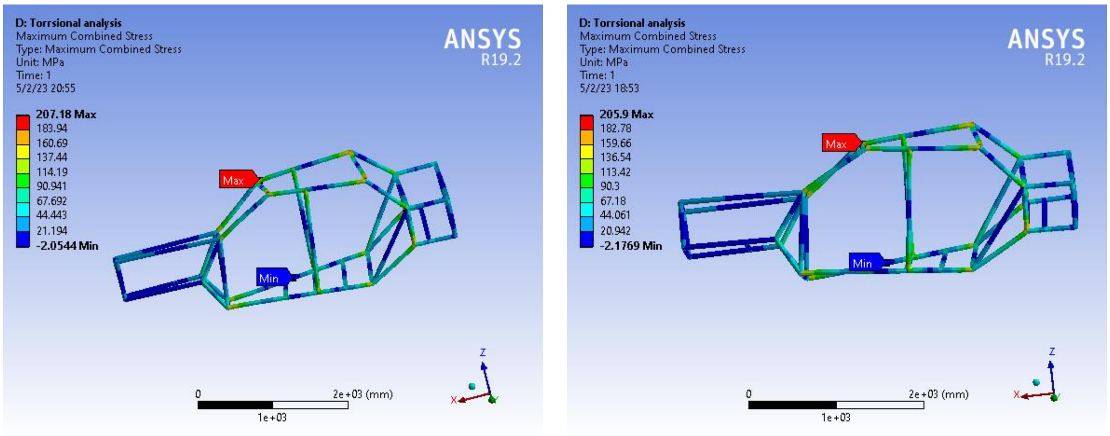


(a) 60 mm Aluminium (b) 60mm Structural steel

Figure 4.21: Combined torsional stress in aluminum (a) and structural steel (b)

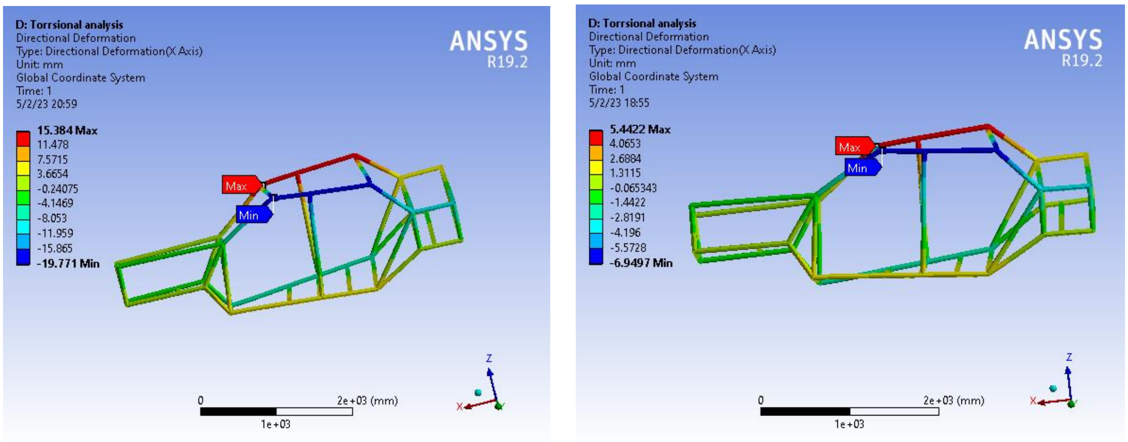


(a) 60 mm Aluminium (b) 60mm Structural steel

Figure 4.22: Deformation of aluminum (a) and structural steel (b) under torsion

Figures 4.21: and 4.22: depict the calculated torsional stiffness for aluminium (735.68kNm/rad) that is much less than general BIW reference data of (1000-1500kNm/rad), but comparable for steel (1064.43kNm/rad). Hence it is required to increase the cross section of structure tube to reduce the stress level.

### 4.3.3 Vertical Bending Case

The response of the structure to the applied static bending load was obtained as shown on Figures 4.23 and 4.24. No variation in bending stress was shown among the two materials as it is a function of moment of inertia of cross sectional area, but deformation is much higher for aluminium. Accordingly bending rigidity of steel (8.89kN/mm) is similar to BIW reference data of 7-11kN/mm, but aluminium (6.6kN/mm) is less stiff for bending load of applied on front cross member.

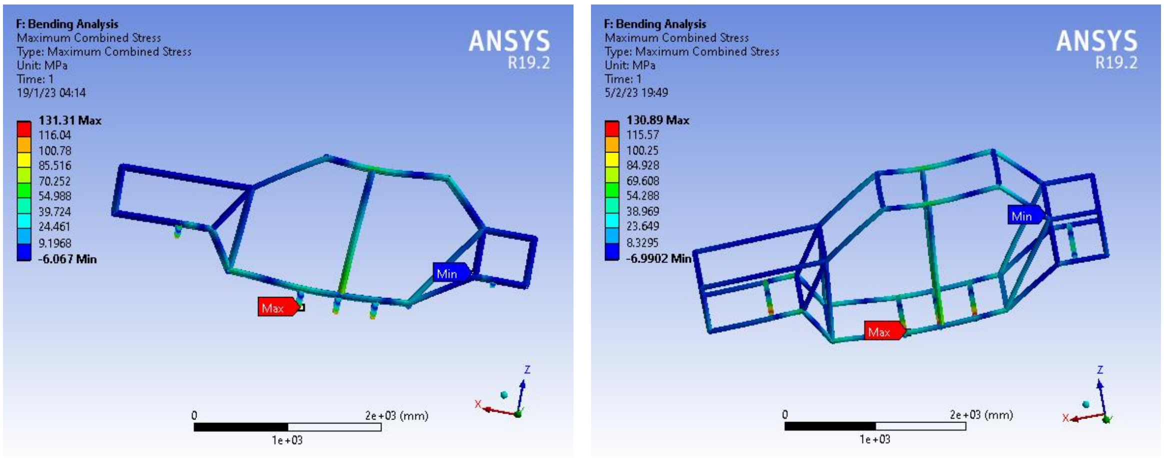


(a) 60 mm Aluminium (b) 60mm Structural steel

Figure 4.23: The induced bending stress in aluminum (a) and structural steel (b)

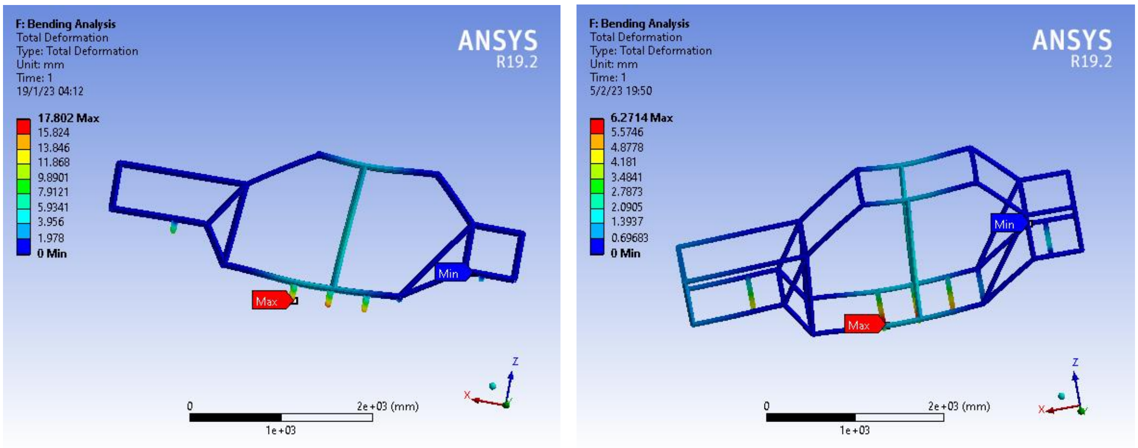


(b) 60 mm Aluminium (b) 60mm Structural steel

Figure 4.24: Deformation of aluminum (a) and structural steel (b) under bending load

### 4.3.4 Impact Analysis

Aluminium fails to provide stiff cargo against 30g frontal impact as the structure deforms 1635.4mm higher than crumble zone of passenger protection as shown in Figure 4.25 (a). However, steel structure deforms only around 1/3rd of aluminium and guaranty full protection of passengers as well as front battery pack as shown in Figure 4.25 (b).

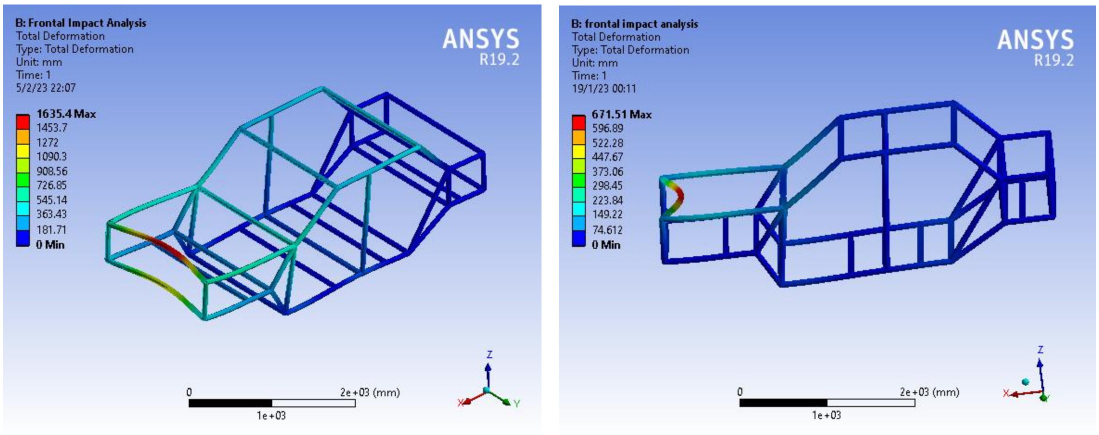


(a) Frontal impact on Aluminium (b) Frontal impact on Structural steel

Figure 4.25: Deformation of aluminum (a) and structural steel (b) under 30g force

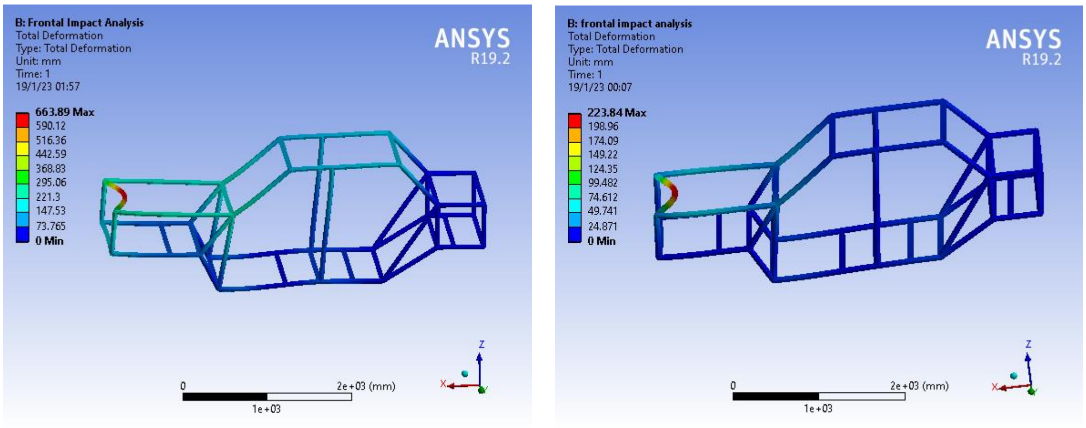


(a) Frontal impact on Aluminium (b) Frontal impact on Structural steel

Figure 4.26: Deformation of aluminum (a) and structural steel (b) under 10g force

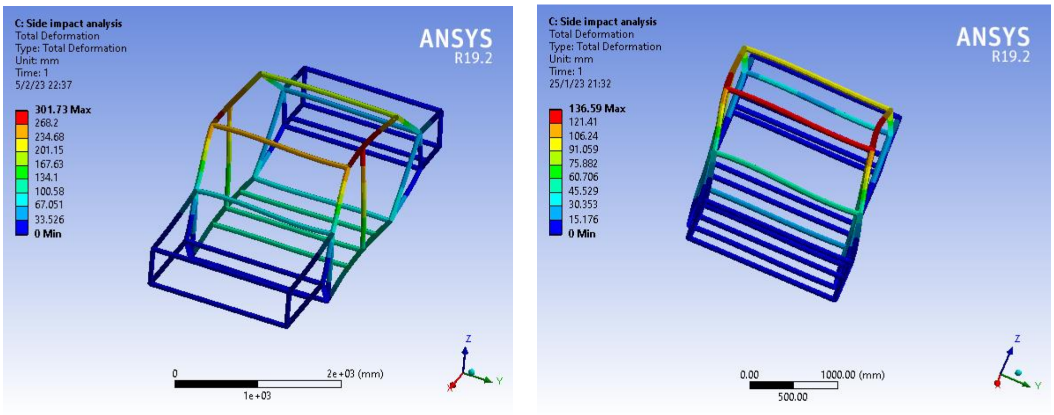


(a) Side impact on Aluminium (b) Side impact on Structural steel

Figure 4.27: Deformation of aluminum (a) and structural steel (b) under 5g force

Frontal 10g impact deformation of aluminium (663.89mm) and steel (223.84mm) are capable to provide full protection of occupants, but aluminium failed to protect front battery pack as its leading edge is 700mm away from front bumper. Side impact of 5g deforms aluminium 301.73mm and steel 136.59 mm as shown in Figure 4.27 (a) and (b) respectively. Hence steel structure is stiff enough to protect occupants and mid-battery pack. Based on these results both aluminium and steel materials failed to qualify requirements of body structure imposed by stiffness and safety

### 4.3.5 Comparison for Different Cross Sections

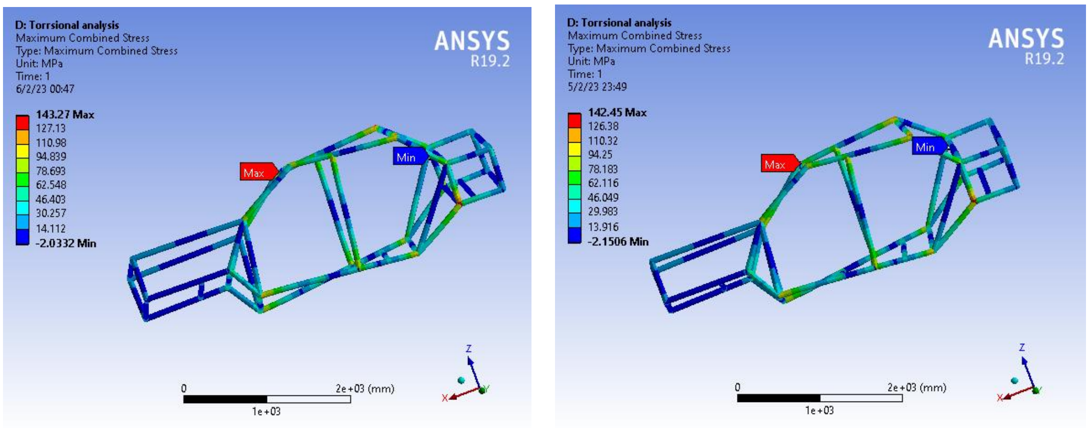


(a) 70 mm Aluminium (b) 70 mm Structural steel

Figure 4.28: The maximum torsional stress in aluminum (a) and structural steel (b)

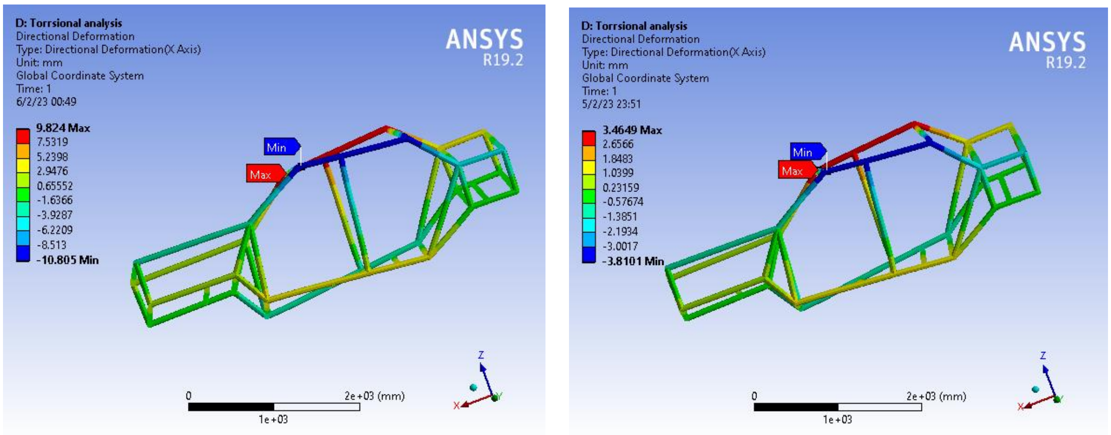


(a) 70 mm Aluminium (b) 70 mm Structural steel

Figure 4.29: Deformation of aluminum (a) and structural steel (b) under torsion

Two different dimensions of 65 and 70mm further modified on the body structure and three dimension (60, 65 and 70 mm) circular tube section with 1mm thickness were analysed to compare the effect on structural rigidity, protection and weight reduction. The two modified

65 and 70mm dimensions are stiff enough in bending and torsional loading cases for the two materials as shown in Table 4.3.

Table 4.3: Comparison of stiffness and stress for different sizes and materials

| Material | Size (mm) | Stress (MPa) Yield | Stress (MPa) Induced | Bend Stiff (kN/mm) | Torsion Stiff (kNm/rad) |
|---|---|---|---|---|---|
| Steel | 60 | 250 | 205 | 8.89 | 1064.43 |
| | 65 | 250 | 170 | 9.54 | 1297.60 |
| | 70 | 250 | 142 | 10.2 | 1160.70 |
| Aluminium | 60 | 280 | 207 | 6.6 | 735.68 |
| | 65 | 280 | 169 | 8.22 | 1203.77 |
| | 70 | 280 | 143 | 8.76 | 1128.50 |

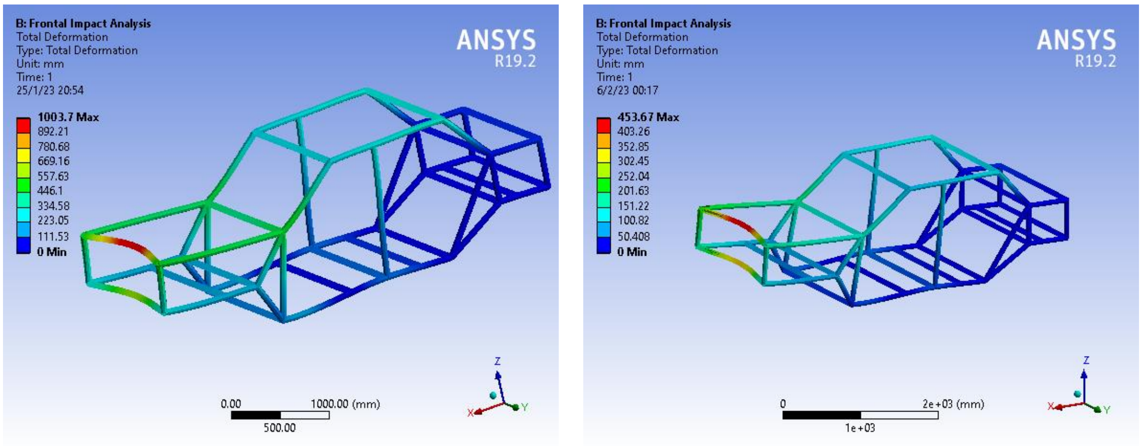


(a) Frontal impact on 70 mm Aluminium (b) Frontal impact on 70 mm Structural

Figure 4.30: Deformation of aluminum (a) and structural steel (b) under 30 g force

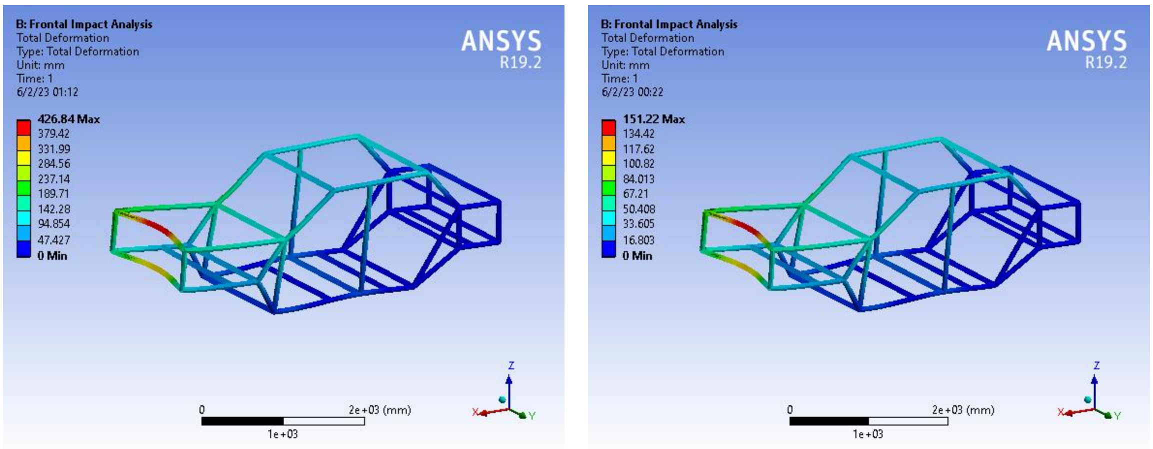


(a) Frontal impact on 70 mm Aluminium (b) Frontal impact on 70 mm Structural

Figure 4.31: Deformation of aluminum (a) and structural steel (b) under 10 g force

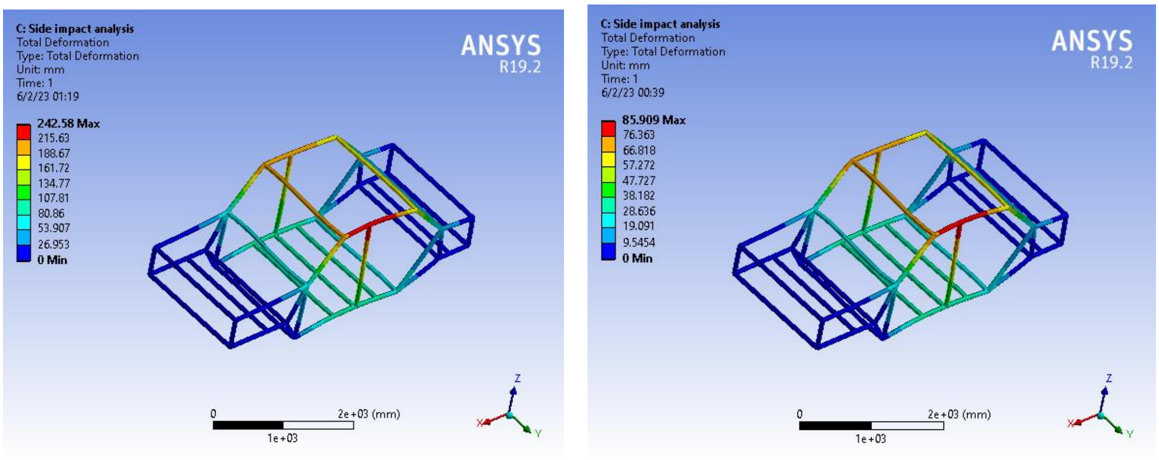


(a) Side impact on 70 mm Aluminium (b) Side impact on 70 mm Structural steel

Figure 4.32: Deformation of aluminum (a) and structural steel (b) under 5g force

Table 4.4: Comparison of impact deformation for different sizes and materials

| Material | Size (mm) | Total deformation | | | | Mass (kg) |
|---|---|---|---|---|---|---|
| | | 5 g side | 10 g front | 20 g front | 30 g front | |
| Steel | 60 | 136.59 | 223.85 | 447.67 | 671.51 | 88.46 |
| | 65 | 106.89 | 193.24 | 386.48 | 579.73 | 95.975 |
| | 70 | 85.51 | 151.22 | 302.45 | 453.67 | 103.49 |
| Aluminum | 60 | 301.73 | 663.89 | 1280.5 | 1635.4 | 31.23 |
| | 65 | 277.94 | 545.14 | 1090.3 | 1106.5 | 33.875 |
| | 70 | 242.58 | 426.84 | 853.69 | 1003.7 | 36.52 |

Steel structure with the two modified 65 and 70mm dimensions as well as 70 mm aluminium qualifies all structural stiffness and safety requirements associated with battery pack and occupant protection as shown in comparison Table 4.4. However, total mass of structure for 70 mm aluminium is 2.83 and 2.63 times lighter than 70 mm and 65mm steel respectively. This reduction in mass could be estimated to save battery energy consumption of 2.12kwh an equivalent energy to extend the range by 18.21km per day

## 4.4 Aerodynamic Drag and Stability Characteristics

### 4.4.1 Results of Quantitative Analysis

Closely examining the CFD simulation result in Figure 4.33: linear increase in $C_D$ with side wind speed was indicated. The simulated average $C_D$ value of 2.76 and 3.11were observed for long range and Bajaj cars to be very high as compared to original car specification of o.35 and 0.45 respectively. At no wind effect case also the $C_D$ value of model cars 0.38 and 0.42 is slightly higher than original benchmarked Toyota corolla and Bajaj cars' value specified by their manufacturers. However, the $C_D$ value of long range modeled with clustered battery pack is 0.325 and the decrease in drag found to consume 7.15% less power due to higher ground clearance and uniform underbody flow as compared to the benchmarked car.

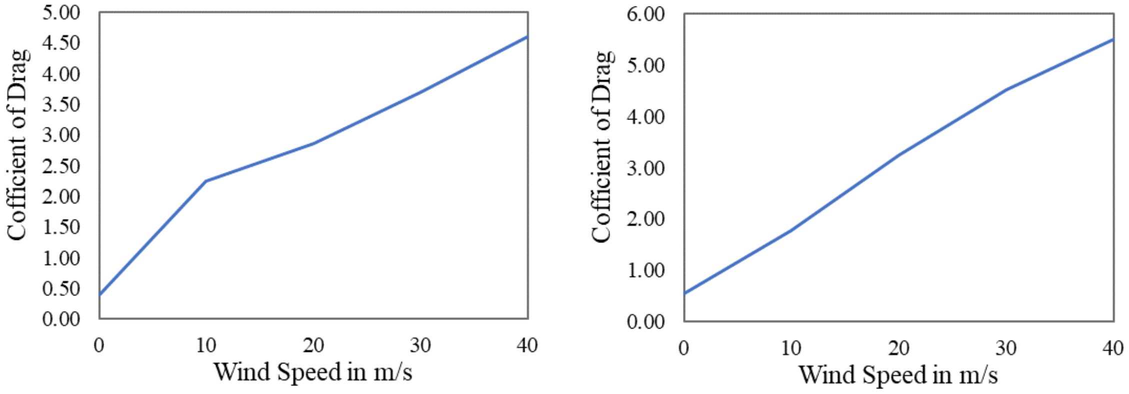


(a) Long range car (b) Bajaj Qute

Figure 4.33: Variation of $C_D$ of long range (a) and Bajaj (b) with side wind velocity

Figure 4.34: depicts aerodynamic lift variation with side wind speed, where it linearly increases for higher side wind velocities for both car models. Long range car tend to lift with average $C_L$ value of 0.91 with side wind as compared to 0.45 of Bajaj. This may be due to higher top speed of 120km/h and wheelbase that influence the vehicle lift. However, for zero side wind velocity the $C_L$ value of Bajaj model 0.02 is lower than original car 0.035. At 10m/sec side wind higher $C_L$ (0.31) and $C_D$ (1.78) values were observed as compared to 20m/sec for Bajaj.

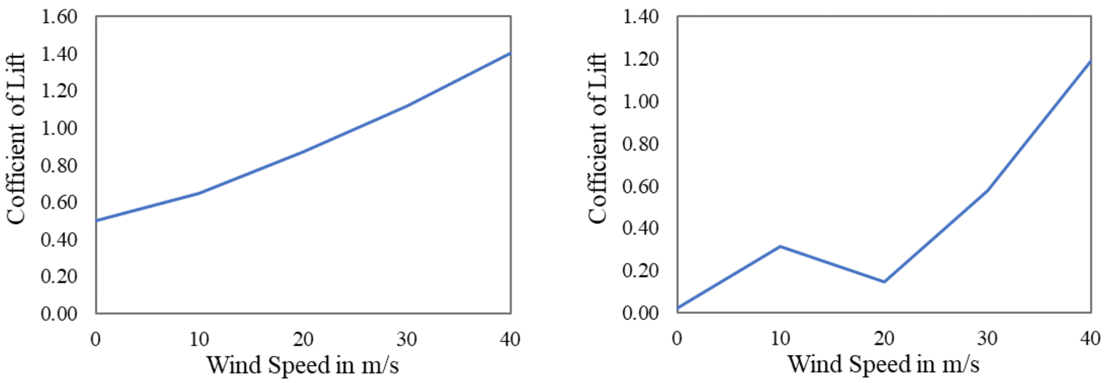


(a) Long range car (b) Bajaj quite

Figure 4.34: Variation of $C_L$ of long range (a) and Bajaj (b) with side wind velocity

This could be due to form drag and the tendency of model to uplift as a result of the decrease in under body and opposite to wind side flow velocity. The increase in drag found to consume 8.368 and 3.435 times higher power as compared to no side wind effect case for long range and low speed Bajaj respectively. At this speed the car is prone uplift and it may tend to be unstable (Mamo, Gopal, & Yoseph, 2024).

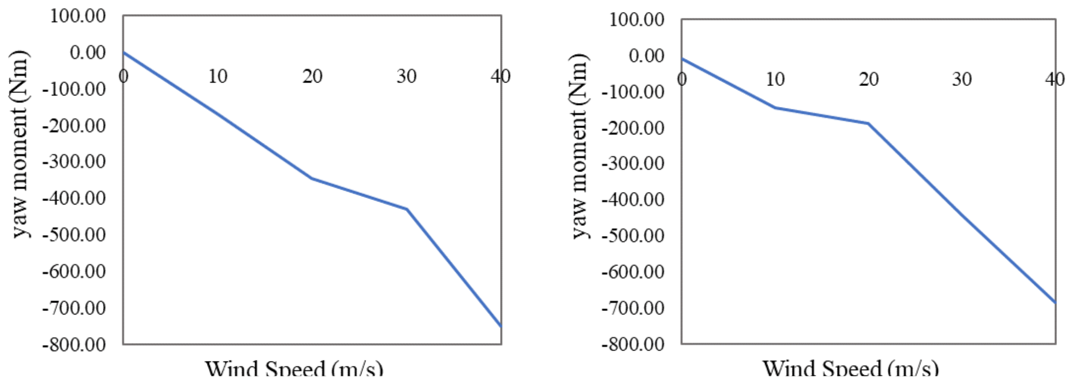


(a) Long range car (b) Bajaj quite

Figure 4.35: Variation of the yaw for long range (a) and Bajaj (b) with side wind

The simulated results indicated that there is paramount linear increase for all induced moments with side wind. As shown on Figures 4.35 (a) and 4.37 (a) negative sign on yaw (-749.18 Nm) and roll (-837.92Nm) moment indicates the long range car tends to be un-stabile and move outward of the road. Roll moments is more dangerous for the specific model specially cornering and moving on banking road of higher than $4^{o}$. The average pitch moment (-97.50Nm) is similar to no wide effect case for Bajaj, but at 10m/sec it is found to be -36.61Nm and the car tend to loose traction due to uplift effect.

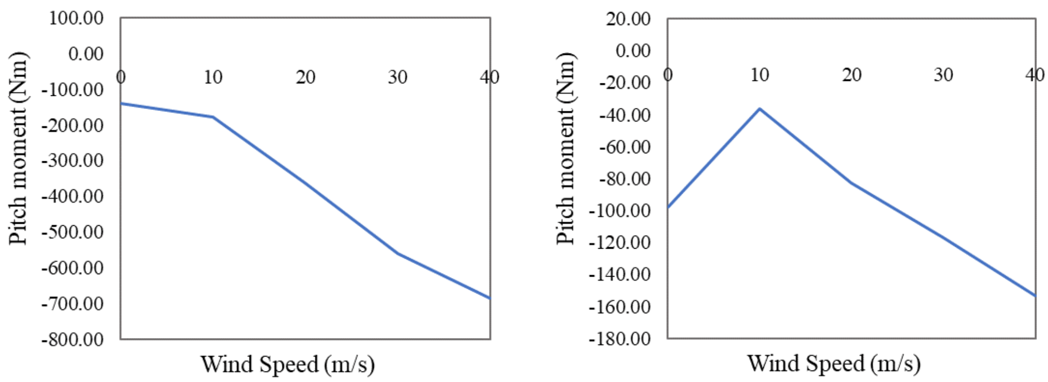


(a) Long range car (b) Bajaj quite

Figure 4.36: Variation of the pitch for long range (a) and Bajaj (b) with side wind

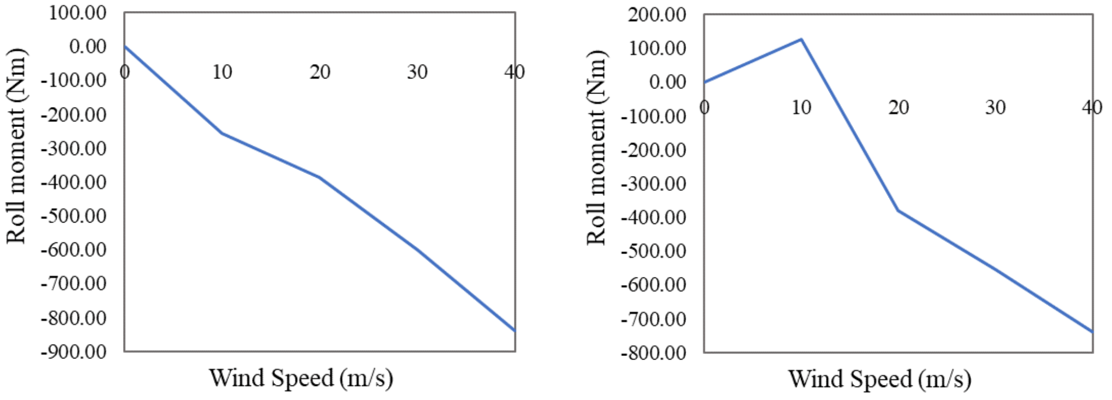


(a) Long range car (b) Bajaj quite

Figure 4.37: Variation of the roll for long range (a) and Bajaj (b) cars with side wind

### 4.4.2 Qualitative Analysis

4.4.2.1 Distribution of Velocity vector

Aerodynamic characteristics was analysed qualitatively from the plots of velocity vector, pressure and kinetic energy contour. Vector plots effectively show the differences in the velocity of the airflow over certain sections of the car's body as shown on Figures 4.38 and 4.39.

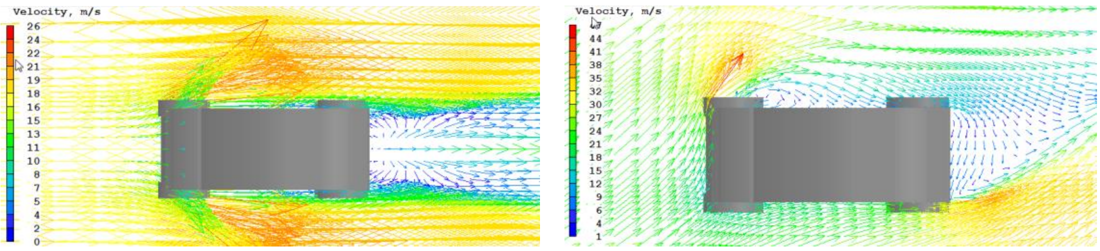


(a) No side wind (b) 10m/s side wind

Figure 4.38: Velocity vectors of Bajaj at no (a) and with 10m/s side wind

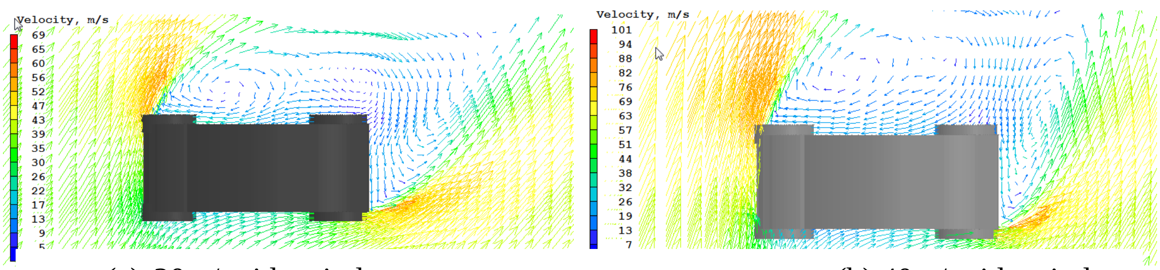


(a) 20m/s side wind (b) 40m/s side wind

Figure 4.39: Velocity vectors of Bajaj with 20m/s (a) and 40m/s (b) side wind

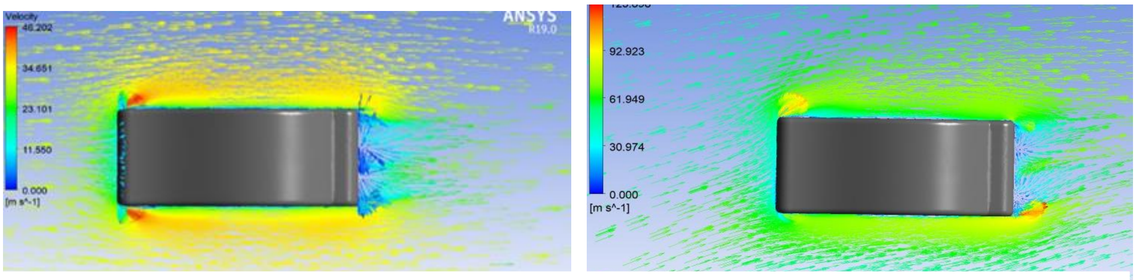


(a) No side wind (b) 10m/s side wind

Figure 4.40: Velocity vectors of long range no side wind (a) and with 10m/s side wind

In Figure 4.38 (a) the high velocity flow regions are around the transition of the windshield to the roof, the rear windshield transition, under body and just after the nose of the car at no side wind simulation. Low velocity was observed around front bumper, wheel arc, sidewalls and wake region. Rear region, where streamlines detach due to square back nature of original car was found to be most critical to form wake drag for Bajaj.

Figures 4.38-4.40 compare the distribution stream wise velocity component (vectors) around the whole body surface of the two model cars at different side wind velocities. The result obtained from simulation with wind effect has shown low airflow velocity around the vehicle viewed on wind flow side. However, higher velocity vector is observed at right front and rear left corners of the vehicle. This disturbed airflow tends to yaw the vehicle about vertical (z-axis) and the driver might lose steering controllability.

#### 4.4.2.2 Variation of pressure contour

Figure 4.41 shows aerodynamic pressure coefficient ($C_P$) variation of long range and Bajaj model cars moving at constant speed of 33.33m/s and 16.67m/s with no side wind effect. High pressure is resulted at fore end of the vehicle when there is no side wind effect.

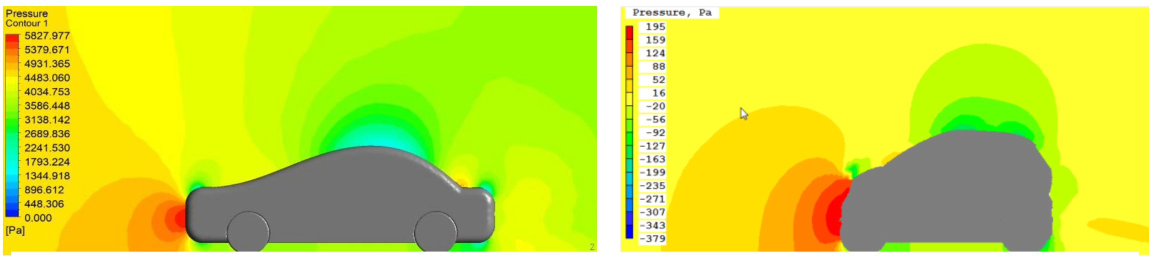


(a) Long range car model (b) Bajaj quite model

Figure 4.41: Pressure contour of long range (a) Bajaj quit (b) with no side wind

Because the front wall of the majority of BEVs is completely closed that causes high stagnation pressure at the front end of the vehicle instead of the flow route that ICEVs' radiator grills give. Near the roof's trailing edge, the upper body flow split, and a wake and high pressure reduction developed at the back end.

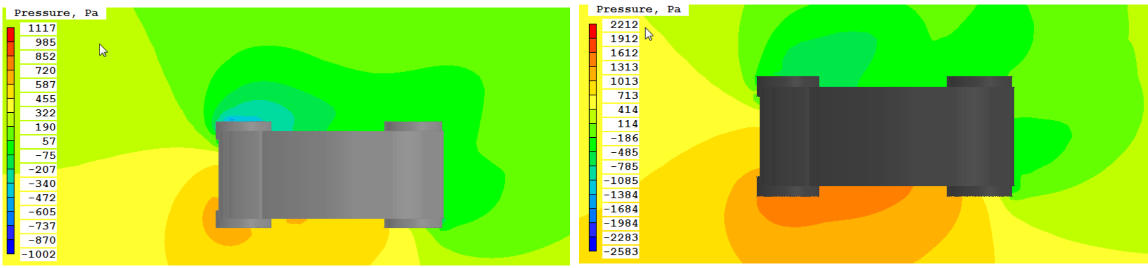


(a) 10 m/s side wind (b) 20 m/s side wind

Figure 4.42: The effect of 10m/s (a) and 20m/sec (b) side wind on pressure of Bajaj

In this simulation, the large pressure differential between the front and back dominates, with skin friction having very little effect. High form drag consequently develops around the two vehicles' bodies.

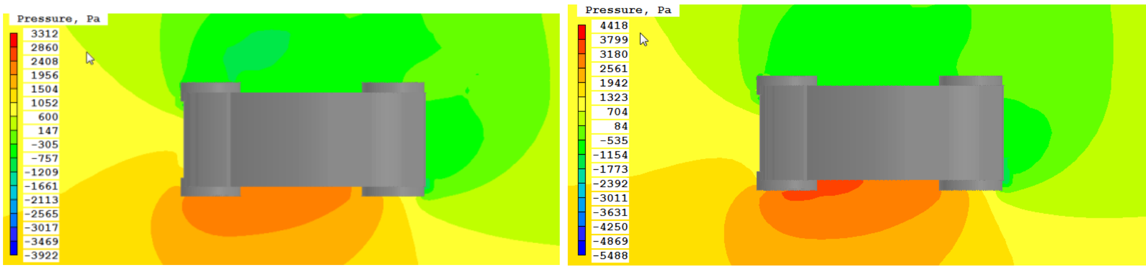


(a) 30 m/s side wind (b) 40 m/s side wind

Figure 4.43: The effect of side wind 30m/s (a) 40m/s (b) on pressure coefficient of Bajaj

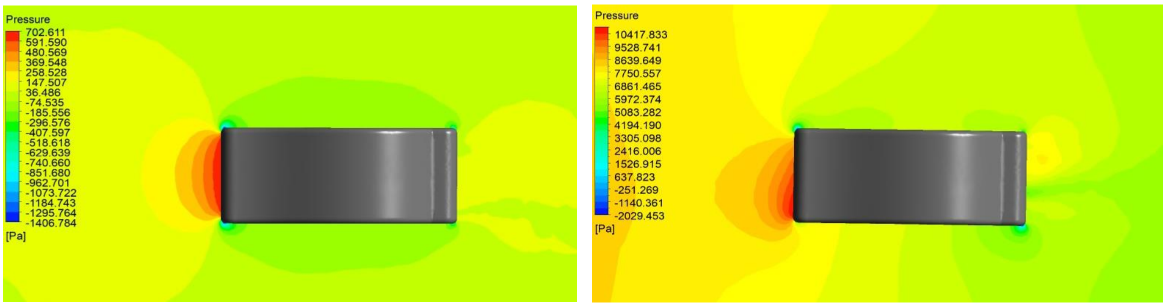


(b) No side wind (b) 20 m/s side wind

Figure 4.44: Pressure contour of long range at no (a) and 20m/s (b) side wind

The effect of side wind velocity on aerodynamic pressure coefficient ($C_P$) was presented in Figures 4.43 and 4.44. As side wind velocity increases, the fore end stagnation pressure and wake formed at rear end of vehicle decreases drastically. However, pressure reduced on rear, underbody opposite side of a car to wind flow direction due to generate eddies. Overall drag force around the vehicle body increased due pressure difference on both sides of the vehicle. However, the impact of side wind on low speed cars is higher than that of high speed regarding the induced pressure coefficient.

#### 4.4.2.3 Variation of turbulent kinetic energy contour

Figure 4.45: shows aerodynamic turbulent kinetic energy variation of long range and Bajaj model cars moving at constant speed of 33.33m/s and 16.67m/s with no side wind effect. High turbulent kinetic energy generated at front, over the roof and rear side of vehicle when there is no side wind effect. The rear of the Bajaj car model was found to be dominant due to the induced eddy around wake region, contributes significantly in the formation of form drag. The contribution of under body for drag of long range found to be higher than Bajaj.

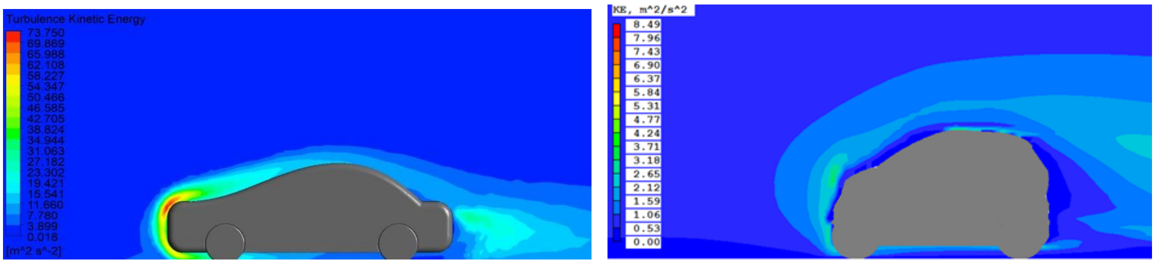


(b) Long range car model (b) Bajaj quite model

Figure 4.45: Kinetic energy of long range (a) Bajaj quit (b) with no side wind

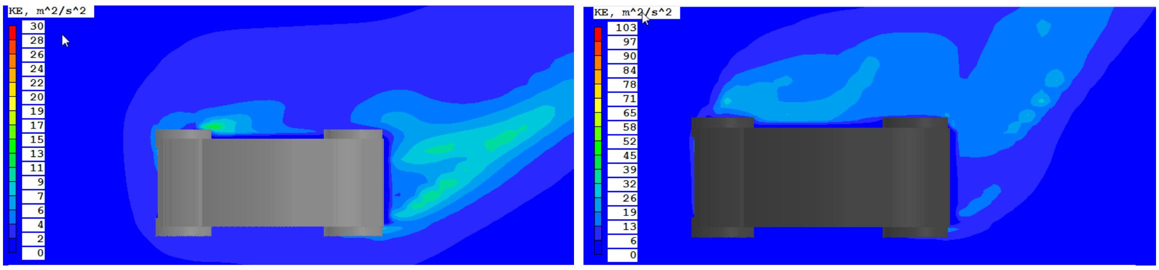


(a) 10 m/s side wind (b) 20 m/s side wind

Figure 4.46: Effect of 10m/s (a) and 20m/s (b) side wind on kinetic energy

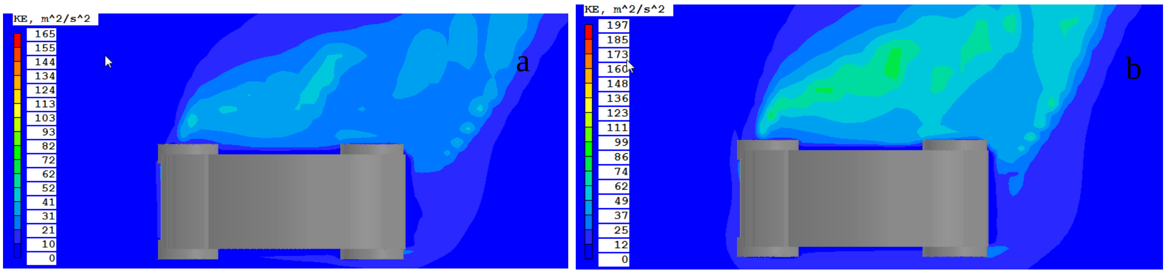


(a) 30 m/s side wind (b) 40 m/s side wind

Figure 4.47: Effect of 30m/s (a) and 40m/s (b) side wind on turbulent kinetic energy

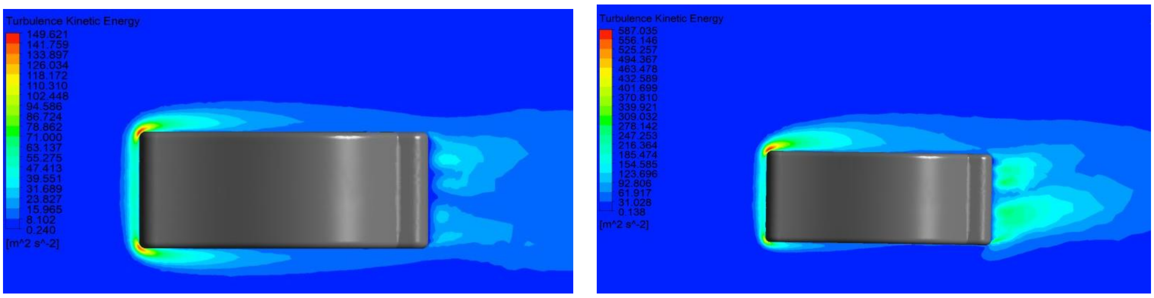


(b) No side wind (b) 20 m/s side wind

Figure 4.48: Effect of 20m/s side wind on turbulent kinetic energy around long rang car

Figures 4.48: show aerodynamic turbulent kinetic energy variation with 20m/s side wind velocities for model car moving at constant speed of 33.33 m/s. Due to side wind effect the turbulent zone mainly on opposite side to wind flow direction of vehicle.

The study investigates the aerodynamic characteristics of long range and low speed car on CAD model using PHOENICS and ANSYS fluent. The Finite-volume method was used, and turbulence models and discretization schemes were studied as parameters. Numerical solutions of PHOENICS show improvement up to 3% in comparison with the ANSYS fluent, in terms of convergence rate and agreement with the available experimental data. The discretization scheme plays a major role in the quality of results, as the flow considered was unidirectional and characterized by high speed. The Upwind discretization scheme is more accurate, providing results improved by more than 1.5% for a given turbulence model on the whole computational field. The use of a high-order discretization scheme is suggested for more acute areas of the body modeled in order to improve results further.

## 4.5 Dynamic Ride Performance of Converted BEV

To investigate the dynamic behaviour, two types of road input were used in Simulink developed stimulation platform. The front and rear tires got a single bump and sine wave for the left wheel input. The road profile inputs for the rear wheel was delayed by time-required to travel the distance of wheelbase at specified speed V.

$$t_d = \frac{l_1 + l_2}{V} \tag{4.2}$$

Where $t_d$ is the time delay between the rear wheel and front wheel, $l_1$ is the distance between the vehicle's front axle and centres of gravity, and $l_2$ is the distance between the vehicle's rear axle and centres and V is vehicle speed.

### 4.5.1 Vertical Wheel Displacement

Vertical wheel displacement is used to assess the tire-to-road-surface contact. The reaction of the front and rear wheels in terms of vertical displacement for the baseline vehicle and the converted BEV is shown in Figure 4.49. The vertical amplitude of motion of the rear wheel is larger than that of the front wheel due to the more complex rear suspension. To investigate the tire's touch with the road, utilise the wheel displacement map. Because of the increased tyre stiffness, the front and rear wheels' capacity to hold the road keeps getting better because they virtually always follow the input profile. It has been noted that unsprang mass, or the front and rear wheels, roughly follows the input signal or speed breaker displacement since tyre stiffness is significantly more than that of a spring and damping is likewise very low.

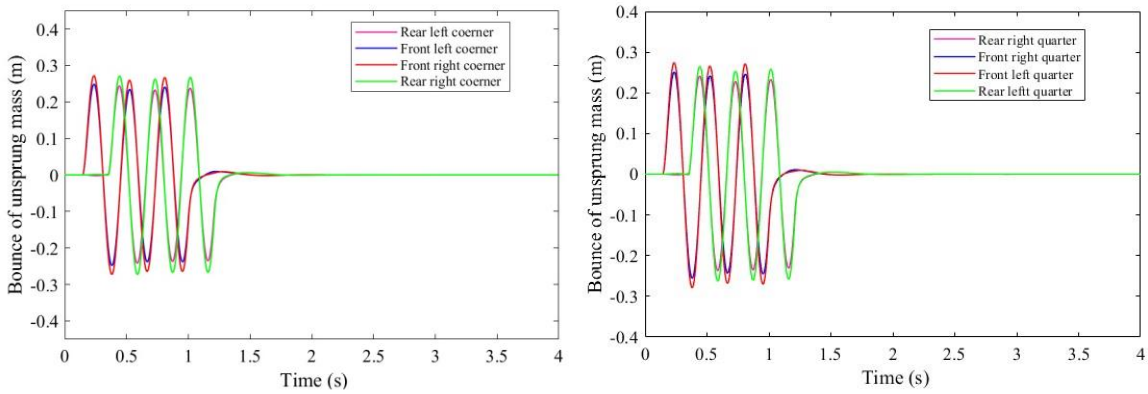


Figure 4.49: Vertical wheels displacement of the converted BEV (a) and baseline car (b)

Figure 4.49: showed how the vertical motion of the wheels and the imperfections in the road differed for the front and rear suspensions when the road bump input was only applied to the left tyres. Due to a high order road bump of 0.25 metres, the left front and rear wheels are marginally larger than the right corner wheels. A negative figure indicates that the tyre has

been "bitten" by the road, whereas a positive number indicates that there is a space between the tyre and the surface.

### 4.5.2 Body Attitude

The three main body attitudes of an automobile that are essential for ride comfort and safety are body bounce, pitch, and roll. Figure 4.50: shows that spring and damper system improves ride comfort by reducing the vehicle's vertical displacement by 44% compared to wheel displacement and by allowing the bounce motion of the sprung mass to fade out gently.

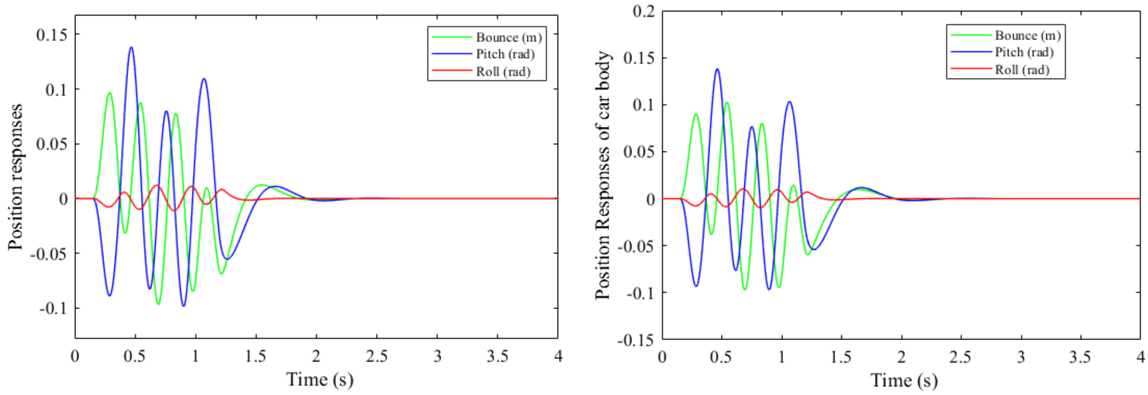


Figure 4.50: Vertical displacement of the converted BEV (a) and baseline car (b) body

Additionally, because the combined effect of the front and rear suspension systems control the overall vertical motion of the sprung mass here, the maximum value of bounce is smaller than that of the front or rear sprung mass considered. This helps to obtain a more realistic idea of the car body displacement. One of the most unpleasant body positions in a car is pitching, so if you want to be comfortable, steer clear of it.

Figures 4.50(a) and (b) demonstrate that the roll motion exited by bump input in the left wheels is less than the amplitude of reaction for the vehicle's vertical bounce and pitch motions. The vertical height and pitch angle are larger at the quarter of the exited tyre because to the delay period between the front and rear wheel tyres contacting the bump. Because of the shorter track distance and lower CG height, it is noted that there is less rolling motion reaction and an almost equal reduction in settling time, which are significantly lower than the vehicle's body pitch reactions.

### 4.5.3 Vehicle Discomfort Parameters

When evaluating a transient ride, one can include the bounce magnitude as well as its first, second, and third order time derivatives, which include vibration velocity, acceleration, and jerk. The ride performance can also be evaluated by looking at the vibration dose value (VDV), which is a cumulative measurement of the vibrations that the passengers' bodies experience as the car passes an impediment. In relation to the time of the fourth power of acceleration, it is computed using the fourth root of the integral. VDV provides a measure of the body's overall vibration exposure, accounting for exposure length, frequency, and magnitude. The analysis method that yields the highest correlation between vibration magnitude and discomfort is VDV, which is based on acceleration.

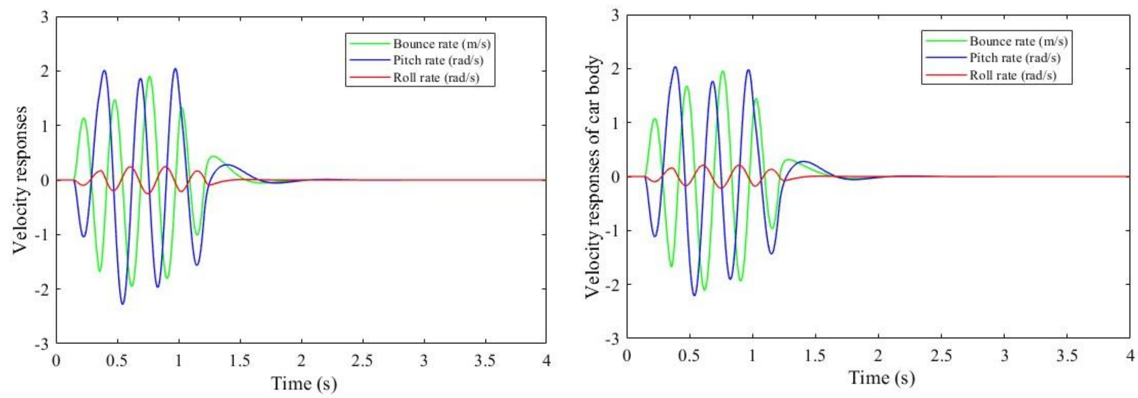


Figure 4.51: Vibration velocity of the converted BEV (a) and baseline car (b) body

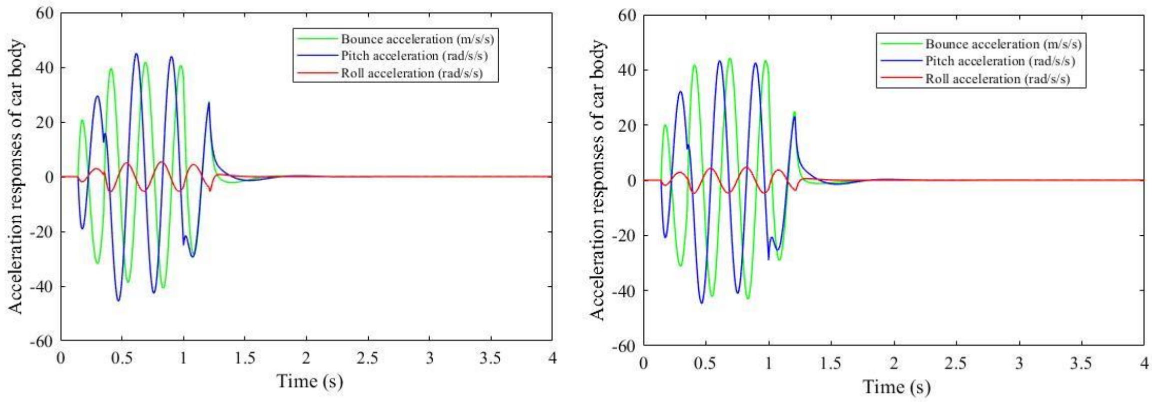


Figure 4.52: Vibration acceleration of the converted BEV (a) and baseline car (b) body

The vehicle's ride comfort performance before and after the conversion, as well as the reactions of the EV conversion with the passive suspension system, are displayed in Figures 4.51 and 4.52. With the exception of the vertical displacement response for both vehicle models, the simulated results show that there have been no appreciable changes to the observed responses as a result of the alterations towards an EV. It appears that when the vehicle is exposed to the random road profiles input, the modification into an EV is causing the vehicle to have a greater vertical displacement peak.

Changes in pitch motions, including pitch angle and pitch rate, were also noted. This is a result of the CG shifting positions. The CG is situated close to the front axle of a typical car, therefore when the wheel struck a bump, the vertical displacement peak would have been higher than when the rear wheel did. Regarding the EV conversion, since the CG is biased towards the rear axle, the vertical displacement magnitude peak is lower when the rear wheel hits a bump than it is when the front wheel does.

# CONCLUSIONS AND RECOMMENDATION

## Conclusions

This dissertation investigates a systematic methodology for integrating electric powertrains into vehicle sizing and synthesis, aiming to reduce energy consumption, improve powertrain efficiency, and ensure dynamic performance, using a simulation-based framework and cost-effective experimentation. The methodology combines a multi-level, step-by-step approach to link customer expectations to final powertrain design configurations. It integrates benchmark analysis into the BEV design process, understanding end user preferences and expectations. These qualitative targets were specified by time and state based quantitative measures and used as inputs for simulation framework

The study used an energy flow analogy-based modelling approach to analyze vehicle performance requirements. Bi-level and physics-based parametric models were developed for component level dynamics. Computationally efficient models were used to optimize vehicle, subsystem, and component targets. The framework was implemented using decomposition-based, Analytical Target Cascading techniques. The integration of an electric powertrain using the BIW concept for BEV conversion design was done, focusing on two small and midsize long-range cars to addresses customer concerns.

First, the synthesized BEV driving cycle captures Addis Ababa's and its suburbs' driving profile, allowing for the calculation of energy consumption of Ethiopian road network and other emerging large cities. The method combines MT random selection-to-RSBS to create a representative DC. It was discovered through behaviour splitting that drivers who exhibit aggression tend to use more energy due to their frequent panic stops and subsequent accelerations.

Second, a new approach for sizing the powertrain of a BEV was developed, integrating with vehicle concepts and considering power intensity as a measure of energy consumption demand. The vehicle's performance was simulated using a vehicle level energy flow analogy modelling approach. The AASU DC showed significant reductions in energy consumption, providing 5-20 km more range than the WLTC cycle.

Third, the implemented BEV powertrain packaging in the BIW concept is energy-efficient and provides integrated structural stiffness and protection during severe collisions. Four design concepts were generated, with the clustered battery pack showing improved weight distribution without major modifications. The FEM model of the integrated body structure showed that 65mm steel and 70mm aluminum are stiff in all loads, providing stiff cargo and full battery pack protection. The weight of aluminium body structure having 70mm was observed to decrease by 10.43% and 11.75% with approximate value of 59.46kg and 66.79kg as compared with 65 and 70mm steel respectively. This reduction in mass from 65mm steel could be estimated to save battery energy consumption of 2.12kwh an equivalent energy to extend the range by 18.21km.

Forth, the study analysed the impact of powertrain components packaging and side wind velocity on aerodynamic drag and stability characteristics in a CAD model. Results showed higher average aerodynamic coefficients and moments than the original car's simulated values. The increase in drag force is due to drag induced underbody, rear side, and opposite side of wind attack. The model car's power requirement increased by 3.3 times to overcome aerodynamic road load with 10m/sec side wind. However, at no wind effect the $C_D$ value of the car with clustered battery pack 0.325 is lower and the decrease in drag found to consume 7.15% less energy (1.8kWh) that can extend the range by 15.46km as compared to the benchmarked car.The model car exhibits stable conditions under side-winds below 15m/sec on straight roads, but can become unstable dynamically on curved or straight roads with winds exceeding 15m/s, potentially causing lane breakaway.

Finally, the ride dynamic performance of a transformed car was evaluated using a full 7 DOF car model in MATLAB/ SIMULIK programme. The results revealed no significant differences in ride comfort performance following the conversion to a BEV. However, the conversion resulted in a greater vertical displacement peak and pitch motion variations due to the CG's position. The RMS value of acceleration ranged from 0.6 to 0.9 m/s2, but to avoid discomfort completely, it should be less than 0.315 m/s2. However, the likelihood of such a significant acceleration occurring is low, and even if it does, it will only last for less than 1 second, with minimal discomfort. In conclusion the implemented methodology for sizing and packaging BEV powertrain resulted reduction of 7.23 kWh battery size that is equivalent to extend the range of long range car by about 53.67km when driven with no side wind effect.

## Recommendations

In the future, it may be beneficial to investigate the temperature effect of the battery caused by packaging, as well as an aerodynamic analysis of internal ducting flow including the estimate of energy required for thermal management of battery. In powertrain sizing, fine-tuning of component controls is critical to improving energy allocation and power management. It is recommended that, in the future, driving and road slope profiles be merged in a parallel simulation to provide a more precise assessment of energy consumption and powertrain efficiency. In this work, modelling and simulation were the primary focus, with experimentation limited to a virtual setup. Additional experimentation in a realistic laboratory is required for further validation. Wind tunnel testing of aerodynamic impacts is also necessary.

Furthermore, while investigating the effect of various vehicle parameters on road hold and ride comfort, it is possible to conclude that increasing front and rear spring stiffness increases the rms acceleration values of front and rear sprung mass, half car sprung mass bounce acceleration, and pitch angle. When the damping coefficient of the front and rear suspension systems is increased, the corresponding front and rear rms values fall, as does the pitch angle. The bounce acceleration value follows a bathtub curve, and the change in tyre stiffness increases ride comfort.

The road holding deteriorates as the front and rear suspension stiffness values grow; it also deteriorates in the case of front damping, but improves when the rear suspension damping values are increased. Future research would look into the effect of changing these suspension parameters on vehicle ride and handling qualities.

# REFERENCES


Aiyan, M., & Sagar, S. S. (2022). *Design and Optimization of an Electric Car Chassis and Body Using Structural Analysis and Computational Fluid Dynamics* (0148-7191). Retrieved from

Al-Ghanim, A. M. H., & Nassar, A. A. (2018). Modeling, simulation, and control of half car suspension system using Matlab/Simulink. *International journal of science and research*.

Alexandru, C. (2020). *A comparative analysis between some dynamic models for the vehicle suspension system.* Paper presented at the IOP Conference Series: Materials Science and Engineering.

Arora, S. (2017). *Design of a modular battery pack for electric vehicles.* Swinburne University of Technology Melbourne, Australia,

Arora, S., Kapoor, A., & Shen, W. (2018). Application of Robust Design Methodology to Battery Packs for Electric Vehicles: Identification of Critical Technical Requirements for Modular Architecture. *Batteries, 4*(3), 30. doi:10.3390/batteries4030030

Barethiye, V., Pohit, G., & Mitra, A. (2017). Analysis of a quarter car suspension system based on nonlinear shock absorber damping models. *International Journal of Automotive and Mechanical Engineering, 14*(3), 4401-4418.

Bere, P., Dudescu, M., Neamtu, C., & Cocian, C. (2021). Design, Manufacturing and Test of CFRP Front Hood Concepts for a Light-Weight Vehicle. *Polymers (Basel), 13*(9). doi:10.3390/polym13091374

Berjoza, D., Pirs, V., & Jurgena, I. (2022). Research into the regenerative braking of an electric car in urban driving. *World Electric Vehicle Journal, 13*(11), 202.

Bisschop, R., Willstrand, O., & Rosengren, M. (2020). Handling Lithium-Ion Batteries in Electric Vehicles: Preventing and Recovering from Hazardous Events. *Fire Technology, 56*(6), 2671-2694. doi:10.1007/s10694-020-01038-1

Bouhsissin, S., Sael, N., & Benabbou, F. (2023). Driver Behavior Classification: A Systematic Literature Review. *Ieee Access*.

Brahim, G., Abdelfatah, N. J. I. C., & Automation. (2012). A novel 4WD electric vehicle control strategy based on direct torque control space vector modulation technique. *2012*.

Busho, S. W., & Alemayehu, D. (2020). Applying 3D-eco routing model to reduce environmental footprint of road transports in Addis Ababa City. *Environmental Systems Research, 9*(1), 1-22.

Cavusoglu, Ö. F. (2017). *Aerodynamics around wheels and wheelhouses.* Chalmers University of Technology,

Chandrashekar, C., Agrawal, P., Chatterjee, P., & Pawar, D. S. (2021). Development of E-rickshaw driving cycle (ERDC) based on micro-trip segments using random selection and K-means clustering techniques. *IATSS Research, 45*(4), 551-560. doi:10.1016/j.iatssr.2021.07.001

Chen, F., Huang, R., Wang, C., Yu, X., Liu, H., Wu, Q., . . . Bhagat, R. (2020). Air and PCM cooling for battery thermal management considering battery cycle life. *Applied Thermal Engineering, 173*, 115154. doi:10.1016/j.applthermaleng.2020.115154

Chesterman, S., & Chevallier, R. (2022). Long term low emission and climate resilient development strategies.

Cinar, G. (2018). A Methodology for Dynamic Sizing of Electric Power. *No. December*.
Decker, L., Förster, D., Gauterin, F., & Doppelbauer, M. (2021). Physics-Based and Data-Enhanced Model for Electric Drive Sizing during System Design of Electrified Powertrains. *Vehicles, 3*(3), 512-532. doi:10.3390/vehicles3030031
Deepankumar, S., Saravanan, B., Yuvaraj, D., Ramesh Kumar, T., Sureshkumar, M., & Simmon, K. V. (2021). *Simulation and Analysis with Material Optimization of Automobile Suspension Using Multi-body Dynamic.* Paper presented at the Advances in Materials Research: Select Proceedings of ICAMR 2019.
Deur, J., Škugor, B., & Cipek, M. J. a. (2015). Integration of electric vehicles into energy and transport systems. *56*(4), 395-410.
Ebrahim, H., Dominy, R., & Martin, N. (2020). Aerodynamics of electric cars in platoon SAGE publications. *Proceedings of the Institution of Mechanical Engineers, Part D: Journal of Automobile Engineering, 235*(5), 1396-1408. doi:10.1177/0954407020965028
Ehsani, M. G., Yimin Longo, Stefano Ebrahimi, Kambiz. (2018). *Modern electric, hybrid electric, and fuel cell vehicles*: CRC press.
Elkamel, A., Angerer, C., Mößner, B., Lüst, M., Büchner, S., Sträußl, F., & Lienkamp, M. (2019). Parameter-adaption for a vehicle dynamics model for the evaluation of powertrain concept designs. *MATEC Web of Conferences, 272*, 01022. doi:10.1051/matecconf/201927201022
Funde, J., Wani, K., Dhote, N., & Patil, S. (2019). *Performance analysis of semi-active suspension system based on suspension working space and dynamic tire deflection.* Paper presented at the Innovative Design, Analysis and Development Practices in Aerospace and Automotive Engineering (I-DAD 2018) Volume 1.
Gao, W., Kong, X., Deng, Z., Yu, W., Wu, Y., & Luo, J. (2021). Review of state of the art in active aerodynamic control research for vehicles. *Journal of Physics: Conference Series, 1985*(1), 012040. doi:10.1088/1742-6596/1985/1/012040
Gao, Z., LaClair, T., Ou, S., Huff, S., Wu, G., Hao, P., . . . Barth, M. (2019). Evaluation of electric vehicle component performance over eco-driving cycles. *Energy, 172*, 823-839.
Gebisa, A., Gebresenbet, G., Gopal, R., & Nallamothu, R. B. (2022). A Neural Network and Principal Component Analysis Approach to Develop a Real-Time Driving Cycle in an Urban Environment: The Case of Addis Ababa, Ethiopia. *Sustainability, 14*(21), 13772.
Ghandour, R., Potams, A. J., Boulkaibet, I., Neji, B., & Al Barakeh, Z. (2021). Driver behavior classification system analysis using machine learning methods. *Applied Sciences, 11*(22), 10562.
Grunditz, E. (2016). *Design and assessment of battery electric vehicle powertrain, with respect to performance, energy consumption and electric motor thermal capability*: Chalmers University of Technology.
Guo, F., Zhang, D., Dong, Y., & Guo, Z. (2019). Urban link travel speed dataset from a megacity road network. *Sci Data, 6*(1), 61. doi:10.1038/s41597-019-0060-3
HAILU, E., & Kibret, D. (2016). Assessment of anthropometric measurements and body composition of selected beginner South West Ethiopian soccer players. *Turkish Journal of Sport and Exercise, 18*(2), 56-64.
Hamza, K., & Laberteaux, K. (2018). A Study on Optimal Powertrain Sizing of Plugin Hybrid Vehicles for Minimizing Criteria Emissions Associated with Cold Starts. *SAE International Journal of Alternative Powertrains, 7*(3), 183-193. doi:10.4271/2018-01-0406

Han, B., Wu, Z., Gu, C., Ji, K., & Xu, J. (2021). Developing a Regional Drive Cycle Using GPS-Based Trajectory Data from Rideshare Passenger Cars: A Case of Chengdu, China. *Sustainability, 13*(4), 2114. doi:10.3390/su13042114

Hassan, M., Mohd, T., Aris, I., Azura, C., & Ibrahim, B. (2015). *A Review of Energy Management System in Battery Electric Vehicle with Hybrid Electrical Energy Source.* Paper presented at the International Conference on Engineering Education and Research.

Heimes, H. H., Kampker, A., Haunreiter, A., Davids, H., & Klohs, D. (2020). Product-requirement-model to approach the identification of uncertainties in battery systems development. *International Journal on Interactive Design and Manufacturing (IJIDeM), 14*(3), 911-922. doi:10.1007/s12008-020-00666-9

Hoang, T. T., Pham, H. T., & Vu, H. M. T. (2022). From Intention to Actual Behavior to Adopt Battery Electric Vehicles: A Systematic Literature Review. *The Open Transportation Journal, 16*(1).

Hossain, M. S., Kumar, L., Islam, M. M., Selvaraj, J., & Miralinaghi, M. (2022). A Comprehensive Review on the Integration of Electric Vehicles for Sustainable Development. *Journal of Advanced Transportation, 2022,* 1-26. doi:10.1155/2022/3868388

Huang, Y., Wang, H., Khajepour, A., Li, B., Ji, J., Zhao, K., . . . Reviews, S. E. (2018). A review of power management strategies and component sizing methods for hybrid vehicles. *96*, 132-144.

Huluka, A. W., & Kim, C. H. (2019). Numerical study on aerodynamic drag reduction and energy harvest for electric vehicle: a concept to extend driving range. *IOP Conference Series: Materials Science and Engineering, 700*(1), 012009. doi:10.1088/1757-899x/700/1/012009

Huzayyin, O. A., Salem, H., & Hassan, M. A. (2021). A representative urban driving cycle for passenger vehicles to estimate fuel consumption and emission rates under real-world driving conditions. *Urban Climate, 36*, 100810.

Indrojarwo, B. T., Estiyono, A., & Pratama, A. R. (2019). Exterior Electric Hatchback Crossover Car Design with Strong, Vicious and Sharp Concept. *IOP Conference Series: Materials Science and Engineering, 588*(1), 012028. doi:10.1088/1757-899x/588/1/012028

Jiang, X., Shan, X., Du, M., & Pu, Z. (2022). Modeling Network Capacity for Urban Multimodal Transportation Applications. *Journal of Advanced Transportation, 2022*, 1-22. doi:10.1155/2022/6034369

Jihui, S., Agyemang, K. O., Zhaolin, C., & Gao, Y. (2022). Optimizing Intermodal Transport and Hub Location Problem for ECOWAS in the Context of Improving Intra-African Trade. *Journal of Advanced Transportation, 2022,* 1-17. doi:10.1155/2022/2559663

Jonas, T., Hunter, C. D., & Macht, G. A. (2022). Quantifying the impact of traffic on electric vehicle efficiency. *World Electric Vehicle Journal, 13*(1), 15.

Kabalan, B. (2020). *Systematic methodology for generation and design of hybrid vehicle powertrains.* Université de Lyon,

Kaleg, S., Hapid, A., & Kurnia, M. R. (2015). Electric vehicle conversion based on distance, speed and cost requirements. *Energy Procedia, 68,* 446-454.

Khan, M. A., Abid, M., Ahmed, N., Wadood, A., & Park, H. (2020). Nonlinear control design of a half-car model using feedback linearization and an LQR controller. *Applied Sciences, 10*(9), 3075.

Khemri, N., Supina, J., Syed, F., & Ying, H. (2019). Developing a Real-World, Second-by-Second Driving Cycle Database through Public Vehicle Trip Surveys. *1*. doi:10.4271/2019-01-5074

Krüger, C., Spohr, S., Merdivan, D., & Urban, P. (2022). Avoiding structural redundancies between the vehicle body and the battery housing based on a functional integration approach. *Automotive and Engine Technology, 7*(3-4), 197-208. doi:10.1007/s41104-022-00106-8

Lajunen, A. S., Panu Laurila, Lasse Pippuri Mäkeläinen, Jenni Tammi, Kari. (2018). Overview of Powertrain Electrification and Future Scenarios for Non-Road Mobile Machinery. *Energies, 11*(5). doi:10.3390/en11051184

Lasocki, J. (2021). The WLTC vs NEDC: A Case Study on the Impacts of Driving Cycle on Engine Performance and Fuel Consumption. *International Journal of Automotive and Mechanical Engineering, 18*(3), 9071.

Lefèvre, S., Kracht, F. E., & Schramm, D. (2020). *Quasi-static and dynamic suspension measurements vs. multi-body and real-time simulation results.* Paper presented at the 10th International Munich Chassis Symposium 2019: chassis. tech plus.

Li, M., Wang, J., Guo, Q., Li, Y., Xue, Q., & Qin, G. (2020). Numerical Analysis of Cooling Plates with Different Structures for Electric Vehicle Battery Thermal Management Systems. *Journal of Energy Engineering, 146*(4). doi:10.1061/(asce)ey.1943-7897.0000648

Li, Y., & Zhu, H. (2019). A Research on Electric Car Styling Design and Low Aerodynamic Drag. *IOP Conference Series: Materials Science and Engineering, 573*(1), 012014. doi:10.1088/1757-899x/573/1/012014

Lin, C.-C., Peng, H., & Grizzle, J. (2004). *A stochastic control strategy for hybrid electric vehicles.* Paper presented at the Proceedings of the 2004 American control conference.

Lin, C., Gao, F., Wang, W., & Chen, X. (2016). Multi-objective optimization design for a battery pack of electric vehicle with surrogate models. *Journal of Vibroengineering, 18*(4), 2343-2358. doi:10.21595/jve.2016.16837

Liu, C., Fang, Z.-d., Liu, X., & Hu, S.-y. (2018). Multibody dynamic analysis of a gear transmission system in electric vehicle using hybrid user-defined elements. *Proceedings of the Institution of Mechanical Engineers, Part K: Journal of Multi-body Dynamics, 233*(1), 30-42. doi:10.1177/1464419318789185

Liu, Y., & Zhang, J. (2021). A Repeated Commuting Driving Cycle Dataset With Application to Short-Term Vehicle Velocity Forecasting. *Journal of Autonomous Vehicles and Systems, 1*(3). doi:10.1115/1.4052996

Mamo, T., Gopal, R., & Yoseph, B. (2024). Modeling and Predesign Analysis of Electric Vehicle Considering Ethiopian Driving Cycle. *International Journal of Automotive Technology*. doi:10.1007/s12239-024-00045-3

Martellucci, L., & Krishna, K. K. (2021). Analysis of Air-Cooling Battery Thermal Management System for Formula Student Car. *Journal of Transportation Technologies, 11*(03), 436-454. doi:10.4236/jtts.2021.113029

Martyushev, N. V., Malozyomov, B. V., Sorokova, S. N., Efremenkov, E. A., & Qi, M. (2023). Mathematical Modeling of the State of the Battery of Cargo Electric Vehicles. *Mathematics, 11*(3), 536.

Muhammad Nabil Farhan, K., Izuan Amin, I., Nofrizalidris, D., Daniel Syafiq Baharol, M., Safra Liyana, S., Razlin Abd, R., & Muhamad Asri, A. (2021). A Review of Aerodynamics Influence on Various Car Model Geometry through CFD Techniques. *Journal of Advanced Research in Fluid Mechanics and Thermal Sciences, 88*(1), 109-125. doi:10.37934/arfmts.88.1.109125

Nicoletti, L., Köhler, P., König, A., Heinrich, M., & Lienkamp, M. (2021). Parametric modelling of weight and volume effects in battery electric vehicles, with focus on the gearbox. *Proceedings of the Design Society, 1*, 2389-2398.

Niroomand, N., Bach, C., & Elser, M. (2021). Vehicle Dimensions Based Passenger Car Classification using Fuzzy and Non-Fuzzy Clustering Methods. *Transportation Research Record: Journal of the Transportation Research Board, 2675*(10), 184-194. doi:10.1177/03611981211010795

Outlook, I. G. E. (2022). Securing Supplies for an Electric Future. 2022. In.

Outlook, I. G. E. (2023). Catching up with Climate Ambitions. *IEA: Paris, France*.

Pathak, A. S., Ganesh Krapf, Sebastian Ongel, Aybike Lienkamp, Markus (2019). Exploration of Optimal Powertrain Design Using Realistic Load Profiles. *10*(3), 56.

Peng, J., Jiang, J., Ding, F., & Tan, H. (2020). Development of Driving Cycle Construction for Hybrid Electric Bus: A Case Study in Zhengzhou, China. *Sustainability, 12*(17), 7188. doi:10.3390/su12177188

Pierri, E., Cirillo, V., Vietor, T., & Sorrentino, M. (2021). Adopting a Conversion Design Approach to Maximize the Energy Density of Battery Packs in Electric Vehicles. *Energies, 14*(7), 1939. doi:10.3390/en14071939

Rashed, G. I., Li, X., Pang, Z., Zhao, H., & Kheshti, M. (2021). Research on Construction Method of Urban Driving Cycle of Pure Electric Vehicle. *E3S Web of Conferences, 252*, 02064. doi:10.1051/e3sconf/202125202064

Razak*, T. A. A., Noor, A. N. M., Razak, M. Y., Ibrahim, M. R. b., Ismail, N. B., & Krishnan, P. (2019). Preliminary Design a nd Packaging of Two Passenger Micro Electric Vehicle ( MEV. *International Journal of Engineering and Advanced Technology, 9*(1), 3270-3273. doi:10.35940/ijeat.A1433.109119

Reick, B., Kaufmann, A., Stetter, R., & Engelmann, D. (2021). Influence of charging losses on energy consumption and CO2 emissions of battery-electric vehicles. *Vehicles, 3*(4), 736-748.

Sabater, C., & Görtz, S. (2021). Gradient-Based Aerodynamic Robust Optimization Using the Adjoint Method and Gaussian Processes. *55*, 211-226. doi:10.1007/978-3-030-57422-2_14

Saldaña, G., San Martín, J. I., Zamora, I., Asensio, F. J., & Oñederra, O. (2019). Analysis of the current electric battery models for electric vehicle simulation. *Energies, 12*(14), 2750.

Sandeep, V., Shastri, S., Sardar, A., & Salkuti, S. R. (2020). Modeling of battery pack sizing for electric vehicles. *International Journal of Power Electronics and Drive Systems (IJPEDS), 11*(4), 1987. doi:10.11591/ijpeds.v11.i4.pp1987-1994

Sanjarbek, R., Mavlonov, J., & Mukhitdinov, A. (2022). Analysis of the Powertrain Component Size of Electrified Vehicles Commercially Available on the Market. *Communications - Scientific letters of the University of Zilina, 24*(1), B74-B86. doi:10.26552/com.C.2022.1.B74-B86

Sayed, K., Kassem, A., Saleeb, H., Alghamdi, A. S., & Abo-Khalil, A. G. (2020). Energy-Saving of Battery Electric Vehicle Powertrain and Efficiency Improvement during Different Standard Driving Cycles. *Sustainability, 12*(24), 10466. doi:10.3390/su122410466

Sharmila, B., Srinivasan, K., Devasena, D., Suresh, M., Panchal, H., Ashokkumar, R., . . . Shah, R. R. (2022). Modelling and performance analysis of electric vehicle. *International Journal of Ambient Energy, 43*(1), 5034-5040.

Shin, J., Kim, W., Yoo, K., Kim, H., & Han, M. (2023). Vehicular level battery modeling and its application to battery electric vehicle simulation. *Journal of Power Sources, 556*, 232531.

Silvaş, E., Hofman, T., & Steinbuch, M. J. I. P. V. (2012). Review of optimal design strategies for hybrid electric vehicles. *45*(30), 57-64.

Singh, M. K., Pathivada, B. K., Rao, K. R., & Perumal, V. (2022). Driver behaviour modelling of vehicles at signalized intersection with heterogeneous traffic. *IATSS Research*, *46*(2), 236-246. doi:10.1016/j.iatssr.2021.12.008

Stanciu, S., Li, M., He, C., Zheng, J., Kassmi, K., & Shmavonyan, G. (2021). Simulation of heat dissipation model of lithium-ion battery pack. *E3S Web of Conferences, 300*, 01014. doi:10.1051/e3sconf/202130001014

Thomas, D. B. (2020). *Real world driving emissions from hybrid electric vehicles and the impact of biofuels.* University of Leeds,

van Kempen, G. (2019). *Multi-body modelling of the Lupo 3L and EL.* Master's thesis, Technical University Eindhoven, 2019. D&C,

Wager, G. (2017). Energy Efficiency of Electric Vehicles and Recharging Technologies under Consideration of Usage Profiles.

Wang, S., Wang, J., Song, L., Niu, Z., & Hu, X. (2022). Design of two-regional flexible-route bus systems considering interregional demands. *Journal of Advanced Transportation, 2022*.

Xia, Q., Yang, D., Wang, Z., Ren, Y., Sun, B., Feng, Q., & Qian, C. (2020). Multiphysical modeling for life analysis of lithium-ion battery pack in electric vehicles. *Renewable and Sustainable Energy Reviews, 131*, 109993.

Yang, N., Fang, R., Li, H., & Xie, H. (2019). Dynamic and static analysis of the battery box structure of an electric vehicle. *IOP Conference Series: Materials Science and Engineering, 688*(3), 033082. doi:10.1088/1757-899x/688/3/033082

Yuan, R., Fletcher, T., Ahmedov, A., Kalantzis, N., Pezouvanis, A., Dutta, N., . . . Ebrahimi, K. (2020). Modelling and Co-simulation of hybrid vehicles: A thermal management perspective. *Applied Thermal Engineering, 180*, 115883. doi:10.1016/j.applthermaleng.2020.115883

Yuan, T., Liu, R., Zhao, X., Yu, Q., Zhu, X., & Wang, S. (2022). Analysis of normal stopping behavior of drivers at urban intersections in China. *Journal of Advanced Transportation, 2022*.

Zhao, D., Zhong, Y., Fu, Z., Hou, J., Zhao, M., & Galante, F. (2022). A Review for the Driving Behavior Recognition Methods Based on Vehicle Multisensor Information. *Journal of Advanced Transportation, 2022*, 1-16. doi:10.1155/2022/7287511

Zhao, G., Wang, X., & Negnevitsky, M. (2022). Connecting battery technologies for electric vehicles from battery materials to management. *iScience, 25*(2), 103744. doi:10.1016/j.isci.2022.103744

Zhao, M., Gao, H., Han, Q., Ge, J., Wang, W., Qu, J., & Vanajakshi, L. (2021). Development of a Driving Cycle for Fuzhou Using K-Means and AMPSO. *Journal of Advanced Transportation, 2021*, 1-15. doi:10.1155/2021/5430137

Zhou, X., Zhao, R., Cheng, L., & Min, X. (2019). Impact of policy incentives on electric vehicles development: a system dynamics-based evolutionary game theoretical analysis. *Clean Technologies and Environmental Policy, 21*, 1039-1053.

# APPENDIX

## Appendix - A

### LIST OF PUBLISHED AND SUBMITTED PAPERS

The following papers are parts of this dissertation contributed to peer-reviewed international journals.

1. Mamo, T.; Gebresenbet, G.; Gopal, R.; Yoseph, B. Assessment of an Electric Vehicle Drive Cycle in Relation to Minimised Energy Consumption with Driving Behaviour: The Case of Addis Ababa, Ethiopia, and Its Suburbs. World Electr. Veh. J. 2023, 14, 302. https:// doi.org/10.3390/wevj14110302.
2. Mamo, T.; Gopal, R.; Yoseph, B. Tamirat, .; Seifu, Numerical Study on Low Speed Electric Car for Public Transportation to Predict its Aerodynamic Performance and Stability, *Engineering and Technology Journal*, e-ISSN: 2456-3358, vol. 08, no. 05, pp. 2183-2190, 2023.https://doi.org/10.47191/etj/v8i5.04
3. Mamo, T.; Gopal, R.; Yoseph, B. Modelling and Predesign Analysis of Electric Vehicle Considering Ethiopian Driving Cycle, *International Journal of Automotive Technology*, vol. 24, 2024.

# Appendix – B

Table B.1: List of top sell BEVs in global market with the corresponding Dimensional and design parameters

| Model | Minimal empty weight [kg] | Number of seats | Wheelbase [cm] | Length [cm] | Width [cm] | Height [cm] | Power[kW] | Torque [Nm] | Maximum speed [kph] | Acceleration 0-100 km/h [s] | Battery capacity [kWh] | Range (WLTP)[km] |
|---|---|---|---|---|---|---|---|---|---|---|---|---|
| BYD e1-Chaina | 870 | 5 | 234 | 346 | 161.8 | 146.5 | 45 | 100 | 101 | 18 | 32.2 | 300 |
| SMART Cabriolet | 1035 | 2 | 187.3 | 269.5 | 166.3 | 155.5 | 82 | 160 | 130 | 11.6 | 17.6 | 154 |
| MITSUBISHI EV | 1080 | 4 | 255 | 339.5 | 147.5 | 160 | 47 | 180 | 130 | | 16 | 135 |
| SMART Cabriolet | 1140 | 4 | 249.4 | 349.5 | 166.5 | 155.4 | 82 | 160 | 130 | 12.7 | 17.6 | 148 |
| Skoda Citigo-e iV | 1178 | 4 | 242.2 | 359.7 | 164.5 | 148.1 | 83 | 212 | 130 | 12.3 | 36.8 | 260 |
| Volkswagen e-up! | 1235 | 4 | 241.7 | 360 | 164.5 | 149.2 | 83 | 210 | 130 | 11.9 | 32.3 | 258 |
| Mini Cooper SE | 1300 | 4 | 249.5 | 384.5 | 172.7 | 143.2 | 184 | 270 | 150 | 7.3 | 28.9 | 234 |
| BMW i3 -120Ah | 1440 | 4 | 257 | 400.6 | 179.1 | 157 | 170 | 250 | 150 | 8 | 37.9 | 359 |
| Peugeot e-208 | 1455 | 5 | 254 | 405.5 | 174.5 | 143 | 136 | 260 | 150 | 8.1 | 50 | 349 |
| Renault Zoe R110 | 1502 | 5 | 258.8 | 408.5 | 178.7 | 156.2 | 108 | 225 | 135 | 11.4 | 52 | 395 |
| Renault Zoe R135 | 1502 | 5 | 258.8 | 408.5 | 178.7 | 156.2 | 135 | 245 | 140 | 9.5 | 52 | 395 |
| Hyundai Ioniq | 1527 | 5 | 270 | 447 | 182 | 147.5 | 136 | 295 | 165 | 9.9 | 38.3 | 311 |
| Hyundai K | 1535 | 5 | 260 | 418 | 180 | 157 | 136 | 395 | 155 | 9.7 | 39.2 | 289 |
| Kia e-Soul | 1535 | 5 | 260 | 419.5 | 180 | 160.5 | 136 | 395 | 157 | 9.9 | 39.2 | 276 |
| Kia e-Soul 64kWh | 1535 | 5 | 260 | 419.5 | 180 | 160.5 | 204 | 395 | 167 | 7.9 | 64 | 452 |
| Citron E-Méhari | 1541 | 4 | 266.7 | 435.4 | 180 | 152.2 | 136 | 260 | 160 | 7 | 30 | 270 |
| Nissan leaf | 1545 | 5 | 270 | 449 | 178.8 | 153 | 150 | 320 | 144 | 7.9 | 40 | 270 |
| Kia e-Niro | 1592 | 5 | 270 | 437.5 | 180.5 | 156 | 136 | 395 | 155 | 9.8 | 39.2 | 289 |
| Opel Mokka-e | 1598 | 5 | 256.1 | 415.1 | 179.1 | 153.2 | 136 | 260 | 150 | 9 | 50 | 324 |
| Chevirolet Bolt EV | 1616 | 5 | 260.1 | 416.6 | 176.5 | 159.5 | 149 | 360 | 150 | 6.5 | 66 | 380 |
| Mazda MX-30 | 1645 | 5 | 265.5 | 439.5 | 179.5 | 155.5 | 145 | 270 | 140 | 9.7 | 35.5 | 200 |
| Hyundai K 64kWh | 1685 | 5 | 260 | 418 | 180 | 157 | 204 | 395 | 167 | 7.6 | 64 | 449 |
| Nissan leaf | 1705 | 5 | 270 | 449 | 178.8 | 154.5 | 217 | 340 | 157 | 6.9 | 62 | 385 |
| Kia e-Niro 64kWh | 1737 | 5 | 270 | 437.5 | 180.5 | 156 | 204 | 395 | 167 | 7.8 | 64 | 455 |
| Honda Clarity | 1825 | 5 | 253.8 | 389.4 | 175.2 | 151.2 | 136 | 315 | 145 | 9 | 35.5 | 222 |
| Tesla 3 LRange | 1862 | 5 | 287.5 | 469 | 193 | 144 | 372 | 510 | 233 | 4.4 | 75 | 560 |
| Volkswagen ID.3 | 1934 | 5 | 277 | 426.1 | 180.9 | 156.8 | 204 | 310 | 160 | 7.9 | 77 | 549 |
| Ford Mustang M E | 1993 | 5 | 297.2 | 472.4 | 188 | 160 | 358 | 487 | 180 | 6.1 | 88 | 483 |
| Tesla S L Range | 2391 | 5 | 296 | 497.9 | 196.4 | 144.5 | 525 | 755 | 250 | 3.8 | 100 | 610 |
| Mercedes-BeEQC | 2,425 | 5 | 287.3 | 476.1 | 188 | 162.4 | 300 | 760 | 180 | 5.1 | 80 | 417 |
| Tesla X L Range | 2464 | 7 | 296.5 | 503.7 | 207 | 162.6 | 245 | 755 | 250 | 4.6 | 100 | 561 |

# Appendix-C

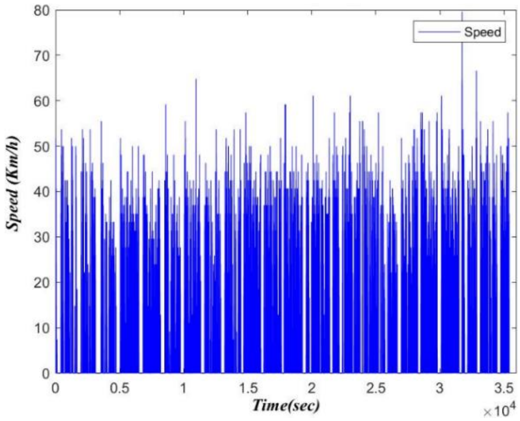


(a) Tested vehicle one

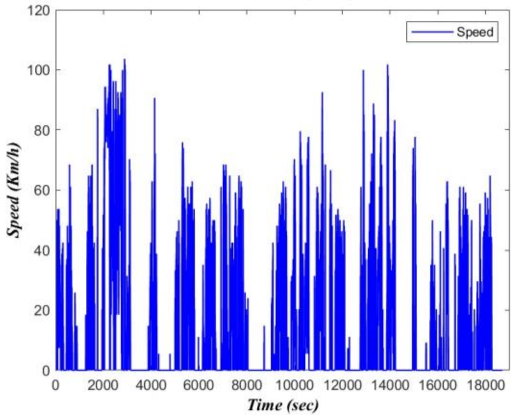


(b) Tested vehicle two

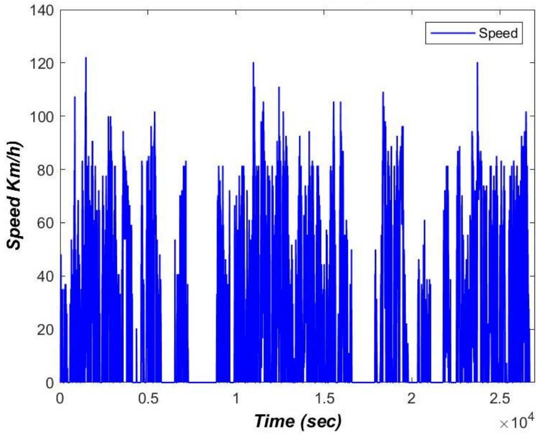


(c) Tested vehicle three

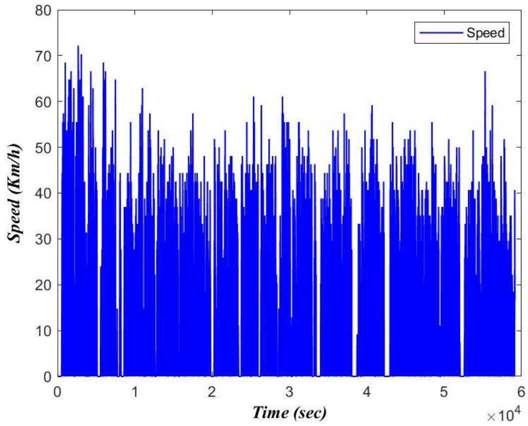


(d) Tested vehicle four

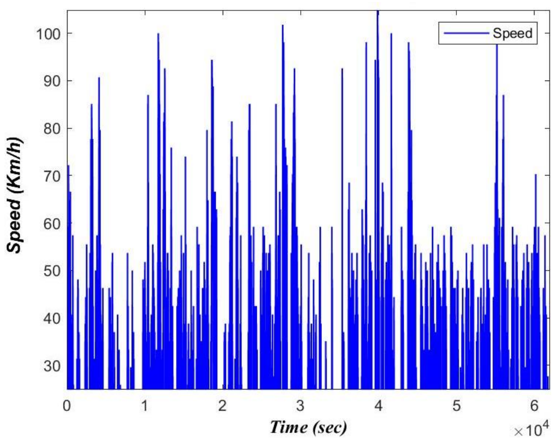


(e) Tested vehicle three

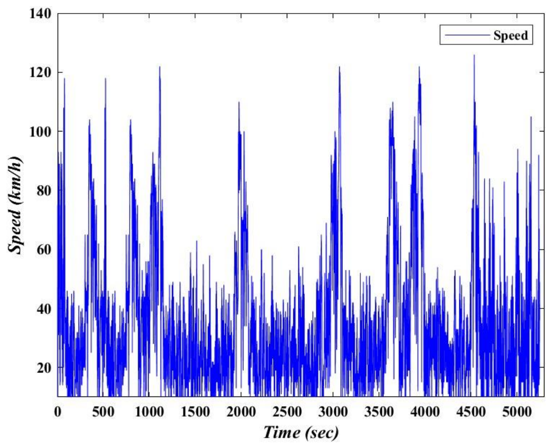


(f) Tested vehicle four

Figure C.1: Raw data collected by six GPS instrumented vehicles

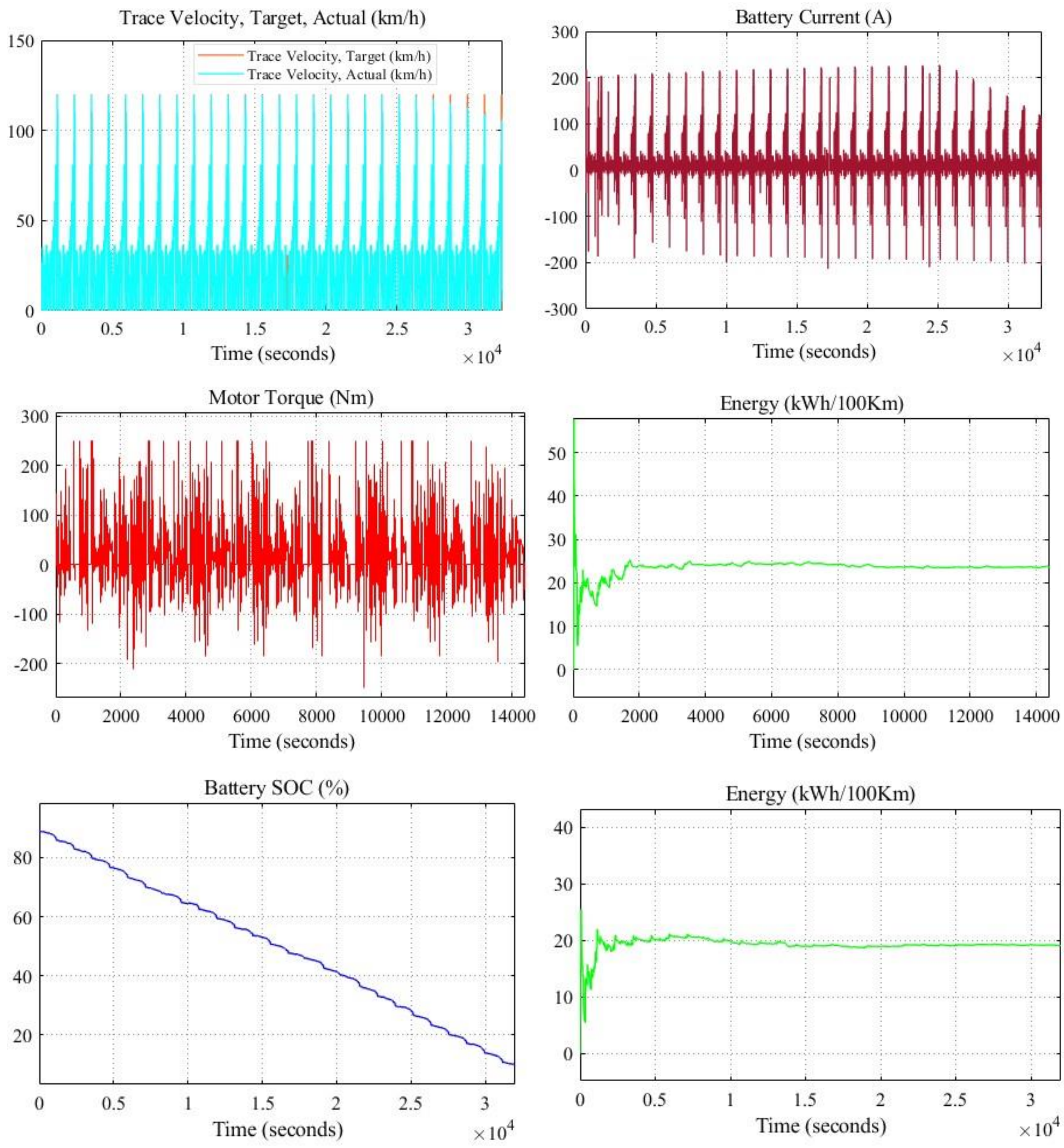


Figure C.2: Full discharge (10% SOC) simulation of fully charged battery in AASU DC